Philipps Universität Marburg

Satellite-based remote sensing of rainfall

In areas with sparse gauge networks and complex topography

DOCTORAL THESIS BY M.SC NAZLI TURINI

Philipps Universität Marburg

Satellite-based remote sensing of rainfall in areas with sparse gauge networks and complex topography

kumulative Dissertation
zur
Erlangung des
DOCTORGRADES DER NATURWISSENSCHAFTEN
(Dr. rer. nat.)

dem Fachbereich Geographie
der PHILIPPS-UNIVERSITÄT MARBURG

vorgelegt von

M.Sc. Nazli Turini

aus Maschhad-Iran

Marburg/Lahn, 2022

Vom Fachbereich Geographie
der Philipps-Universität Marburg
als Dissertation am 06.04.2022 angenommen.

Erstgutachter: Prof. Dr. Jörg Bendix
Zweitgutachter: Prof. Dr. Peter Chifflard

Weitere Mitglieder der Prüfungskommission:
Prof. Dr. Bernhard Seeger
Prof. Dr. Carina Peter

Tag der mündlichen Prüfung am 20.06.2022
Hochschulkennziffer: 1180

Foreword

I wrote this thesis in 2021. The last two years were the strangest I (and probably you also) have ever experienced, where nothing has been familiar. The unprecedented COVID-19 pandemic and health crisis has affected our lives globally, and the year 2020 was nominated as the second-hottest year on record for the planet. In May 2020, extreme rainfall events and flooding in the Kasese District in Uganda wrecked houses, power stations, and hospitals and drowned villages. This disaster also affected neighboring countries such as Kenya and Rwanda. Moreover, when social distancing was recommended, floods forced thousands of people suffering from homelessness and needing emergency food assistance to vacate. On the other side of the world, Australia experienced one of the worst wildfires in modern history, the Tropical Storm Isaias hit Florida, and floods caused damage in Germany.

These events prompted me to rethink why I am pursuing a PhD in water management and geography science as we are clearly failing! It was devastating to experience and hear about these environmental disasters one by one and to witness the vulnerability within and between countries.

When I attended the final conference for the Global Resource Water (GRoW) project in 2020 (online due to the pandemic), I came across a talk that made me think. I do not remember who spoke, but it began with, "We saw this year as important for accessing clean water in people's lives, due to the pandemic". It was stated by the World Health Organization and others that outbreaks of infectious diseases, including COVID-19, require that humans have access to clean water, sanitation, and hygienic conditions.

Different studies have shown that, due to COVID-19 lockdowns, a CO2 reduction was recorded on Earth for the first time due to less international travel. I realized that, regardless of how complicated our problems are, we still have an extreme influence on our environment, yet we can change paths if we believe that our livelihood depends on it. It also made me rethink the importance of the path I started in life. Therefore, I want to believe that we can still change our paths. The United Nations (UN)

sustainable development goals (SDG) and 2016 Paris agreement challenge us to change the way we think about the environment and about threats to humanity. I hope my work can be a grain in our unified effort to help Earth breathe.

Nazli Turini

Abstract

Rainfall is an essential parameter in the analysis and research of water resource management. However, the complexity of rainfall combined with the uneven distribution of ground-based gauges and radar in developing countries' mountainous and semi-arid areas limits its investigation. In this context, satellite-based rainfall products provide area-wide precipitation observations with a high spatio-temporal resolution, engaging them in hydrological management in ungauged basins.

Therefore, in this study, I investigated method to establish a satellite-based rainfall algorithm for ungauged basins. The algorithm combines the new Integrated Multi-SatEllite Retrieval for the Global Precipitation Measurement (GPM) (IMERG) rainfall products and second-generation geostationary orbit (GEO) systems developing rainfall retrieval techniques with the high spatio-temporal resolution using machine learning algorithms.

For the first step, microwave satellite and Meteosat Second Generation Spinning Enhanced Visible and Infrared Imager (MSG SEVIRI) data for Iran were collected to develop a regionally based new rainfall retrieval technique. The method used geostationary multispectral infrared (IR) data to train Random forest (RF) models. I employed the microwave (MW) rainfall information from the IMERG as a reference for RF training. The rainfall area was delineated in the first step, followed by rainfall rate assignment. The validation results showed the new technique's reliable performance in both rain area delineation and rain estimate, particularly when compared to IR-only IMERG. Multispectral IR data improves rainfall retrieval compared with one single band.

In the next step, I investigated the applicability of the developed algorithm in Ecuador with different orography and rainfall regimes compared to Iran. For this aim, I used the Geostationary Operational Environmental Satellite-16 (GOES-16) as the GEO satellite, which covers Ecuador at a suitable angle. The feature selection and algorithm tuning were performed to regionalize the models for Ecuador. The validation results show the reliable performance of the method in both rain area

delineation and rain estimation in Ecuador. The results proved the suitability of the developed algorithm with different GEO systems and in different regions. Some inaccuracies at the Andes' high elevation were evident after the spatial analysis of the validation indices. Evaluating the validation results against a high spatio-temporal radar network showed that the developed algorithm has difficulty capturing drizzles and extreme events dominant in the Andes' high elevations and needs improvement.

In summary, this research presents a new satellite-based technique for rainfall retrieval in a high spatio-temporal resolution for ungauged regions, which can be applied in parts of the world with different rainfall regimes. This findings could be used by planners and water managers regardless of the availability of rain gauges at ground. Furthermore, the research showed, for the very first time, the advantage of using the new generation of GEO satellite combined with microwave satellites integrated in GPM IMERG for estimating rainfall.

Zusammenfassung

Der Niederschlag ist ein wesentlicher Parameter bei der Analyse und Erforschung der Bewirtschaftung von Wasserressourcen. Die Komplexität des Niederschlags in Verbindung mit der ungleichmäßigen Verteilung von bodengestützten Messgeräten und Radar in den gebirgigen und halbtrockenen Gebieten von Entwicklungsländern schränkt jedoch seine Untersuchung ein. In diesem Zusammenhang liefern satellitengestützte Produkte flächendeckende Niederschlagsbeobachtungen mit einer hohen räumlich-zeitlichen Auflösung, die für das hydrologische Management in nicht beprobten Einzugsgebieten eingesetzt werden können.

Daher konzentriert sich die vorliegende Untersuchung auf die Erstellung eines satellitengestützten Niederschlagsalgorithmus für nicht beprobte Einzugsgebiete. Die neuen IMERG (Integrated Multi-SatEllite Retrieval for Global Precipitation Measurement (GPM)) Satellitenprodukte werden mit geostationären Orbit-Systemen (GEO) der zweiten Generation mittels Algorithmen des maschinellen Lernens zur Niederschlagsermittlung mit hoher räumlicher und zeitlicher Auflösung kombiniert.

In einem ersten Schritt wurden Mikrowellensatelliten- und Meteosat-Daten der zweiten Generation des Spinning Enhanced Visible and Infrared Imager (MSG SEVIRI) für den Iran gesammelt, um eine neue, regional basierte Methode zur Niederschlagsermittlung zu entwickeln. Die Methode verwendete geostationäre multispektrale Infrarotdaten (IR), um Random-Forest-Modelle (RF) zu trainieren. Als Referenz für das RF-Training wurden Mikrowellen-Niederschlagsdaten (MW) des IMERG verwendet. Im ersten Schritt wurde das Niederschlagsgebiet abgegrenzt, gefolgt von der Zuordnung der Niederschlagsmenge. Die Validierungsergebnisse zeigen, dass die neue Technik sowohl bei der Abgrenzung des Niederschlagsgebiets als auch bei der Niederschlagsschätzung zuverlässig funktioniert, insbesondere im Vergleich zum IR-only IMERG. Multispektrale IR-Daten verbessern die Niederschlagsermittlung im Vergleich zu einem einzelnen Band.

Im nächsten Schritt wurde die Anwendbarkeit des entwickelten Algorithmus in Ecuador untersucht, das sich in Bezug auf die Orographie und das

Niederschlagssystem vom Iran unterscheidet. Zu diesem Zweck wurde der Geostationary Operational Environmental Satellite-16 (GOES-16) als GEO-Satellit verwendet, der Ecuador in einem geeigneten Winkel abdeckt. Die Auswahl der Features und das Tuning des Algorithmus wurden durchgeführt, um die Modelle für Ecuador zu regionalisieren. Die Validierungsergebnisse zeigen die zuverlässige Leistung der Methode sowohl bei der Abgrenzung von Regengebieten als auch bei der Schätzung der Niederschlagsmenge in Ecuador. Die Ergebnisse belegen die Eignung des entwickelten Algorithmus für verschiedene GEO-Systeme und verschiedene Regionen. Nach der räumlichen Analyse der Validierungsindizes wurden einige Ungenauigkeiten in denhohen Lagen der Anden deutlich. Die Auswertung der Validierungsergebnisse anhand eines räumlich-zeitlichen Radarnetzes zeigt, dass der entwickelte Algorithmus Schwierigkeiten bei der Erfassung von Nieselregen und extremen Wetterereignissen hat, die in den hohen Lagen der Anden vorherrschen, und dahingehend verbessert werden muss.

Diese Forschungsarbeit stellt ein neues satellitengestütztes Verfahren zur Niederschlagsermittlung mit hoher räumlicher und zeitlicher Auflösung vor, das auf Regionen ohne Bodenstationsmessungen und unterschiedliche Niederschlagsregime angewendet werden kann. Dieser Algorithmuskann von Planungs- und Wasserwirtschaftsämtern oder anderen einschlägigen Einrichtungen unabhängig von der Verfügbarkeit von Regenmessern am Boden genutzt werden. Darüber hinaus zeigte die Untersuchung zum ersten Mal den Vorteil der Nutzung der neuen Generation von GEO-Satelliten in Kombination mit den in IMERG integrierten Mikrowellensatelliten für die Bewertung der Niederschlagsmenge.

Acknowledgments

Undertaking this PhD has been a truly life-changing experience for me and it would not have been possible without the support and guidance that I received from many people.

Foremost, I want to thank Dr. Boris Thies and Prof. Jörg Bendix, who initiated this PhD project and trusted me. Dr. Boris Thies who invested so much time into me, and without his help and guidance, this thesis will never be finished. Thanks for all insight and support to Prof. Jörg Bendix.

I am very thankful to my "Saisonales Wasserressourcen-Management in Trockenregionen: Praxistransfer regionalisierter globaler Informationen (SAWAM)" project colleagues for their cooperation. Especially I thank Christof Lorenz as well as the project leader Harald Kunstmann (Karlsruhe Institute of Technology). I gratefully acknowledge the financial support by the Federal Ministry of Education and Research (BMBF) within the SAWAM project.

This work certainly wouldn't have been possible without the support of Isabel, Maik, Sebastian Egli, Rütger and Christine whose helps in maturing ideas and developing them into the thesis is highly appreciated.

It was a great pleasure working and socializing with the other Ph.D. students, post-docs, and colleagues at LCRS. Thanks to Sebastian Achilis, Paulina Alava Nunez, Martin, Wolfgang, Katja, Lukas, Galo, Johanna, Benjamin, Michaela. Special thanks to Birgit for spending hundreds of hours in her office, and supplying me with cookies have always been my greatest pleasure.

A special mention to my parents, and my brothers Peyman and Ehsan whom I can always count. Thanks to my friends, Elmira, Elham, Micheal, Pascha, Kristin, Vida

and Fatima who tried to support me on my journey. Finally, thanks to Daniel for sharing everything with me and showed me what support and patient means.

Contents

Chapter 1

Introduction

1.1 Motivation

The United Nations (UN)-sustainable development goals (SDG) include 17 goals adopted in 2015 with the aim of world equality in economic prosperity and environmental sustainability [1]. One of the SDGs' most significant concepts is water security. SDG 6 is dedicated to sanitation and drinking water supply (targets 6.1 and 6.2), also including issues related to integrated water resources management (IWRM) (target 6.5).

As the World Water Development Report 2015 [2] asserts, "Water is at the core of sustainable development." Therefore, water is crucial and remains relevant to current times, where water management strategies for local people may lead to higher environmental stress nationally and globally [3].

Establishing a goal for securing sustainable and adequate water resources is required to understand the relationship between finite water resources, climate diversity, and different elements of sustainability. Precipitation is a vital link in the global water cycle and represents climate change; thus, adequate spatio-temporal precipitation information is essential for proper water management strategies [4, 5].

However, accurate precipitation measurement is challenging because of large spatio-temporal variations. Ground-based rainfall observations are insufficient due to the inadequate and uneven distribution of rain gauges and radars, especially in developing countries, mountainous, remote areas, and semiarid regions [6, 7, 8]. On the other hand, the need for high-quality rainfall contrasts with the observed decline in ground-based observation worldwide [9].

Consequently, the complexity of rainfall and poor data availability limit investigation and research in developing countries, mountainous, remote areas, and

semiarid regions [10]. These limitations are a big issue since data collection is the first step in the tool chain for water resource management [10].

Remote sensing applications and numerous recent satellite missions allow monitoring precipitation around the globe [10]. For this reason, in many developing countries, mountainous, remote areas, and semiarid regions, satellite-based rainfall products are the only sources of precipitation information both in space and time, rendering them attractive for water management and research in ungauged basins.

1.2 Current satellite-based rainfall products

Precipitation rates from satellites can be estimated from visible (VIS) to infrared (IR) sensors on Geostationary Earth Orbit (GEO) satellites or, from microwave (MW) on Low Earth Orbiting Low Earth Orbiting (LEO) satellites [11].

MW sensors provide relatively accurate precipitation information due to their sensitivity to cloud hydrometeors. By contrast, IR sensors on GEO satellites scan the relationship between cloud top temperature and precipitation rate. However, they provide a higher spatio-temporal resolution, which is of great interest to near-real-time applications.

In 1997, the first space-borne Precipitation radar (PR) onboard the Tropical Rainfall Measuring Mission (TRMM) was launched with TRMM Microwave Imager (TMI) [12]. TMI MW measurements could be compared directly with vertical PR scans of atmospheric columns in time and space [13].

Recent operational or research algorithms for rainfall retrieval utilize the GPM Microwave Imager (GMI) on board the Global Precipitation Measurement (GPM) satellites [14]. The GMI instrument carries 13 microwave channels ranging in frequency from 10 GHz to 183 GHz (four high frequency, millimeter-wave channels near 166 GHz and 183 GHz) [14] and provides significantly improved spatial resolution compared with the TMI (Table 1.1).

GEO satellites scan the Earth more frequently and provide better temporal resolution , therefore, they are more attractive for real-time precipitation monitoring [15]. GEO satellites can view about one-third of the Earth's surface. Still, the data quality toward the extremities diminishes due to the increasing scan angle to the exterior. Therefore, five operational GEO satellites are required to ensure full west–east coverage [16].

The sensors' technology varies among the GEO satellites (e.g., Advanced Baseline

Imager (ABI) [17], MSG SEVIRI [18], Advanced Himawari Imager (AHI)); however, they all provide VIS and IR sensors in a high spatio-temporal resolution.

Currently, active GEO satellites include the METEOSAT series [18] operated by the European Organisation for the Exploitation of Meteorological Satellites (EUMETSAT), two U.S.-operated Geostationary Operational Environmental Satellite (GOES) [17] operated by the National Oceanic and Atmospheric Administration (NOAA), the Japanese Himawari satellites (https://himawari8.nict.go.jp/) operated by the Japan Meteorological Agency, Elektro-L satellites developed by the Russian Federal Space Agency by NPO Lavochkin.

The second generation of GEO systems deliverers more detailed cloud properties due to their higher spectral resolution. The ABI sensor in GOES-16 is a multispectral passive imaging radiometer that scans the earth every 10 minutes with 16 spectral channels, ranging from visible (0.47 μ) to long-wave IR (13.3 μ) [17]. The Spinning Enhanced Visible and InfraRed Imager (SEVIRI) sensor on the Meteosat Second-Generation Spinning Enhanced Visible and Infrared Imager (MSG SEVIRI) satellite scans the earth in 11 IR wavelengths between 0.6 and 14 μ with a nominal spatial resolution of 4 km^2 every 15 minutes [18].

Table 1.1 reviews the primary instrumentation used for rainfall retrieval from VIS, IR and MW spectrums.

Table 1.1: Review of satellite instrumentation for rainfall retrieval

Instrument	**Satellite**	**Channels**	**Bands**	**Spatial**	**Temporal**
AVHHR	NOAA / MetOp	5	VIS / IR	1	twice daily
MSG SEVIRI	MSG	12	VIS / IR	1–4	15 minutes
ABI	GOES	16	VIS / IR	0.5-2	5–15 minutes
TMI	TRMM	5	10.7–85.5 GHz	5–25	twice daily
GMI	GPM	13	10–183 GHz	6–26	2-3 hours
AHI	Himawari	5	VIS / IR	16	30 minutes

Although high spatio-temporal satellite-based rainfall is earning demand within scientific and management communities, it still confronts many difficulties. One difficulty is to derive high-quality precipitation estimates from each sensor, followed by the more significant challenge of merging information from different sensors. Combined products aim for better accuracy, spatial coverage, and extended time series [19].

In recent years, combined MW-IR methods have attempted to exploit the advantages of both systems for more accurate precipitation dissipation at a higher spatio-temporal resolution globally and regionally [12].

The empirical relationship between IR and MW sensors was developed to (i) Find the IR threshold for rain area delineation and rain estimate using MW rainfall information as a reference; or, (ii) match the cumulative distribution functions of MW-based rainfall and brightness temperature from IR scans to generate the IR rain rate equation assuming that colder clouds produce more rain [12, 20, 21, 22]; (iii) regression methods in which the related MW estimates coincide with IR pixel data to demonstrate a regression-based equation for rain-rate estimation [23, 24, 25].

Another algorithm strategy is to obtain the "best" local estimate for a given grid box. This method has been used to generate precipitation products in a medium resolution in high accuracy rather than high temporal resolution time series [19]. The algorithm of the 3B42-RT product of the TRMM [12] is based on available MW estimates from different satellites every 3 h in the spatial resolution of $0.25° \times 0.25°$. The gaps between grids are then filled with rainfall estimates retrieved from the MW-calibrated IR algorithms. The instrumental differences between IR and MW may affect the spatial accuracy of rainfall products [19].

The Climate Prediction Center MORPHing technique (CMORPH) [26] uses the propagation of precipitation estimates between two MW scans using IR-based cloud tracking. CMORPH is a global precipitation algorithm that estimates rainfall at 0.25° every half hour. Using IR imagery, motion vectors in space and time advance the precipitation estimates derived from passive microwave (PMW) sensors. Furthermore, a time-weighted linear interpolation modifies the shape and intensity of the precipitation between microwave sensor scans. This algorithm can include any precipitation data from MW scans into precipitation retrieval using the temporal forward and backward scans to propagate rainfall [26].

The Integrated Multi-SatEllite Retrieval for the Global Precipitation Measurement (IMERG) [27] mission and its GPM core satellite is the newest global 30-min precipitation product with spatial 0.1° resolution [27]. IMERG unifies all the PMW observations from the GPM constellation network [27]. PMW precipitation primarily uses theGoddard profiling algorithm (GPROF) [28, 29], using a Bayesian approach conditioned upon surface classes, surface temperature, and total precipitable water. First, all the PMW estimates are intercalibrated in this algorithm. Then, as Huffman et al. [27] demonstrated, the Ku-band is used as a reference to calibrate Global

Precipitation Climatology Centre (GPCC) V2.3 product [30] to seasonal and regional adjustments. In the next step, the morphing process from CMORPH fills the gaps from the PMW estimates by applying motion vectors computed from ancillary data. Then, the Kalman filter approach [31] uses IR-calibrated precipitation from the Precipitation Estimation from Remotely Sensed Information using Artificial Neural Networks (PERSIANN)—Cloud Cluster System algorithm [20, 32] to supplement the morphed precipitation.

IMERG integrates one thermal band at 10.7 µm of IR in it's algorithm (IR-only). In addition, Huffman et al. [27] stated that managing the large volume of multi-spectral IR retrieval from different GEO platforms is challenging. There is a mismatch of IR-based rainfall estimation and surface precipitation motions due to IMERG limiting its bands to one and the restriction of visible data to daylight hours. Therefore, Huffman et al. [27], in the official document of IMERG, encouraged scientists and researchers to contribute and develop algorithms for improving the IR-based rainfall in IMERG since different validation studies' IR retrieval estimations have performed poorly in IMERG [33, 34].

Combining IR data from the GEO satellite with machine learning techniques was accurate in satellite-based rainfall retrieval algorithms [35, 36, 37, 38].

In satellite-based rainfall retrievals, machine learning techniques relate the predictor variables and rainfall estimates. The great advantage of machine learning algorithms over physically-based models is that they offer a higher potential in handling non-linear and complicated relationships between variables and a larger volume of training data [39].

The most globally famous machine learning-based rainfall retrieval is PERSIANN [22]. Using the GEO IR information, it uses an artificial neural network to cluster pixels based on their surface characteristics. A multivariant linear function mapping is developed for each group to relate the variables to rainfall rate estimates. Also, available algorithms such as PERSIANN provide rainfall daily in $0.25° \times 0.25°$, which is a low temporal and spatial resolution [22].

Additionally, different studies have already developed the retrieval based on multispectral IR bands from the second generation of GEO satellites and used ground-based information as a reference. Kühnlein et al. [35, 36] demonstrated the capability of random forest (RF) to estimate rainfall in midlatitudes. The algorithm is based on information from MSG SEVIRI and uses ground-based radar data as a reference to (i) delineate the precipitating cloud areas; (ii) differentiate between

convective and advective-stratiform precipitating areas; (iii) estimate the rainfall rates assigned separately to the convective and advective-stratiform precipitating areas.

Although the algorithm by Kühnlein et al. [35, 36] provides accurate rainfall information regionally, a significant drawback is that it is related to ground-based radar availability, which restricts its usage to the availability of ground truth data. As mentioned previously, many places with complex topography are characterized by less precipitation ground truth data. Therefore, the developed retrieval by Kühnlein et al. [35, 36] cannot apply to all regions.

1.3 Aims and Hypotheses

The overview presented in Section 1.2 shows that existing satellite-based rainfall retrieval has the following advantages and weaknesses:

- Available products such as PERSIANN [22] and IMERG [27] provide rainfall information globally but in a low spatial and temporal resolution, which are not applicable for water resource management;
- MW sensors return comparatively accurate precipitation estimates, but their temporal resolution is coarse;
- GEO satellites scan the earth more frequently and provide better temporal resolution [15]. However, they provide less accurate rainfall information. Second-generation GEO systems provide more detailed information about precipitation-relevant cloud properties due to their higher spectral resolution.
- Regionally developed algorithms based on the new generation of GEO satellites (e.g., algorithm developed by Kühnlein et al. [35, 36] provide high spatio-temporal resolution. However, they are trained based on ground truth data. Unfortunately, less precipitation ground truth data are available in most arid and semi-arid areas and complex topography. On the other hand, by applying RF techniques in IR-based rainfall retrieval by Kühnlein et al. [35, 36], the possibility of obtaining more information from second-generation GEO systems and handling large volumes of rainfall is provided;
- The IMERG [27] product, as the newest global MW-IR algorithm, unifies all the PMW observations from the GPM constellation network to benefit from the

accuracy of PMW sensors in rainfall retrieval. However, when geostationary IR data is incorporated into IMERG, managing the large volume of multispectral IR retrieval from different GEO platforms becomes challenging. Therefore, in IMERG, only one thermal band at 10.7 µm is integrated.

Therefore, to maximize the aforementioned benefits and overcome the weaknesses of satellite-based rainfall products, and support water management in regions without enough rainfall information, the aim of this thesis was formulated as follows:

Aim To combine the advantages of second-generation GEO systems and PMW rainfall information from the new IMERG product to develop a regionally adapted rainfall retrieval scheme with a high spatio-temporal resolution based on machine learning algorithms in ungauged regions.

The following four hypotheses were developed in accordance with the thesis aim mentioned above:

Hypothesis 1 the combination of PMW rainfall information with multispectral IR data from modern GEO satellites using machine learning algorithms can improve rainfall retrieval accuracy and provide high spatio-temporal resolution for rainfall information in ungauged regions.

Hypothesis 2 the developed algorithm in hypothesis 1 is transferable with equal accuracy to areas with complex topography and rainfall regimes.

Hypothesis 3 the accuracy assessment is highly dependent on the spatial coverage and resolution of the products.

Hypothesis 4 the main uncertainties in the satellite-based rainfall retrievals are due to drizzle and high rainfall rates, which are difficult to capture.

1.4 Study Areas

In order to test the aforementioned hypotheses, Iran and Ecuador, with their high spatio-temporal rainfall variability and complex topography, were chosen as study areas in this thesis (Figure 1.1). These regions were selected to support the Seasonal Water Resources Management for Semiarid Areas: Regionalized Global Data and Transfer to Practise (SaWaM) project funded by the Federal Ministry of Education

and Research (BMBF). I chose the GEO satellites GOES-16 (2 km^2, 10 minutes) for Ecuador and MSG-1 (4 km^2, 15 minutes) for Iran for their spatial resolution and central view on the aforementioned regions ((Figure 1.1-a). More detailed descriptions of MSG-1 and GOES-16 can be found in Chapters 2 and 3, respectively.

Ecuador (Figure 1.1-b) extends from 28°N - 18.58°S and from 68.58°W - 82°W with an area about 1,500,000 km^2, covering different climatological zones, from northern Ecuador to the central Andean plateau. The extreme east–west precipitation variability is due to the Andes mountain region. In Ecuador, the precipitation drivers mainly include the biannual migration of the intertropical convergence zone (ITCZ), El Niño–Southern Oscillation (ENSO), and the cold von Humboldt current in the Pacific Ocean. Furthermore, the Amazon basin and the Andes mountain range strongly impact precipitation [40, 41]. The rainfall amount in Ecuador differs from the Pacific coast south around 300 mm annually to the upper Amazon basin. The average rainfall of 3500 mm per year provides high rainfall variability in space and time over Ecuador [42].

Iran (Figure 1.1-c) is located between the 20°N–40°N latitudes and 44°E–63°E longitudes and has an area of about km^2. Two mountain ranges in Iran play a significant role in rainfall distribution. Along the Caspian Sea, the Alborz range in the north extends east–west with a maximum altitude of ~5000 m.a.s.l. The Zagros Mountains stretch from northwest to southeast with a maximum elevation of ~3500 m.a.s.l. These two mountainous ranges are essential to the variety of rainfall amounts and distribution. Iran is considered an arid or semiarid country with an average rainfall of ~250 mm in a year. The rainfall ranges from 50 mm in the deserts to 1600 mm on the Caspian sea. The main drivers of precipitation in Iran originate from migrating Mediterranean lows from the west and Sudan lows from the southwest. The interactions between these synoptic systems and the complex topographic cause the precipitation to be highly variable in space and time [43, 44]. The dominant precipitation types in January, February, November, and December are stratocumulus, altostratus, stratus, and nimbostratus; whereas, during warm months, cumulus, altocumulus, and deep convective have the maximum precipitation rate in Iran [45].

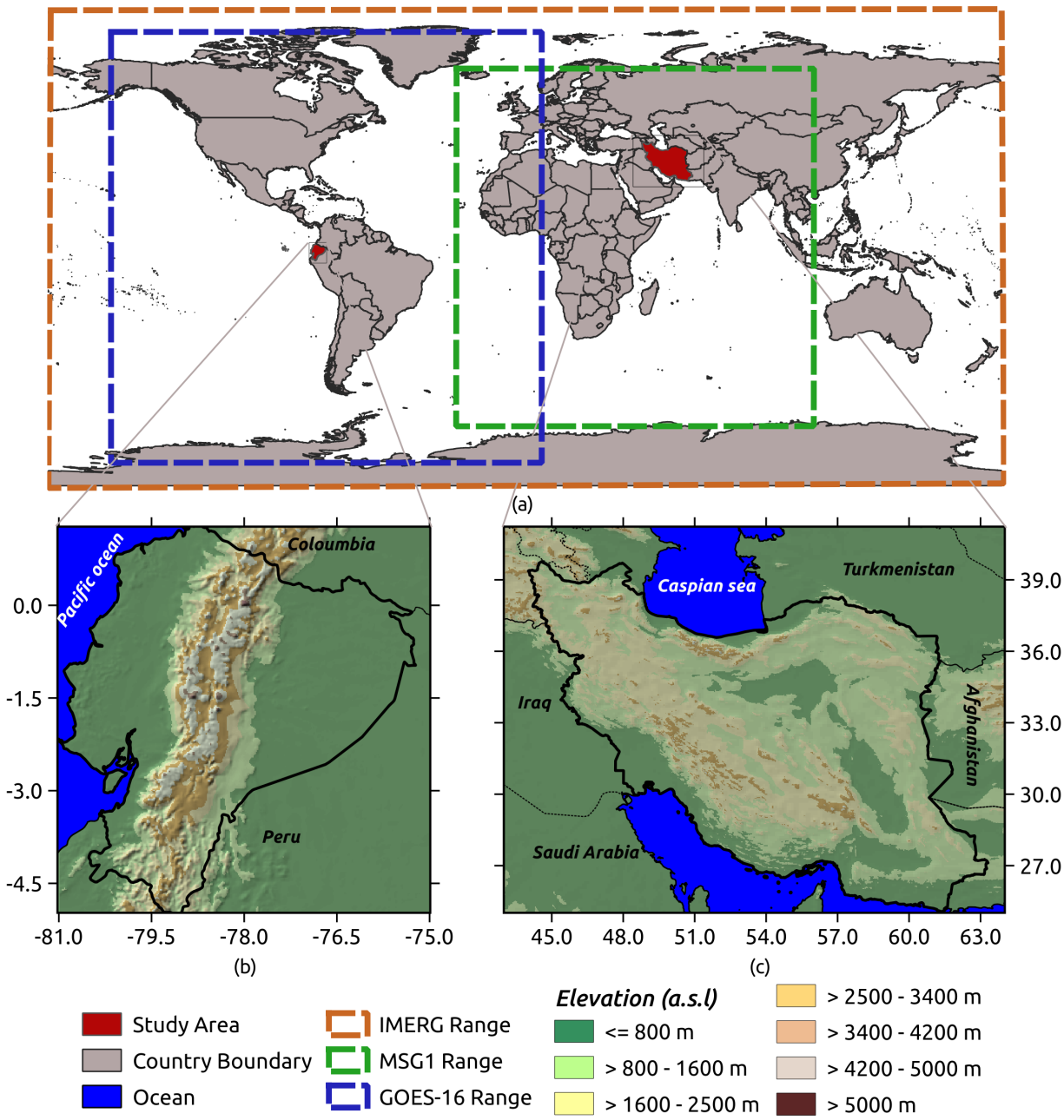

Figure 1.1: (a) The study areas of the thesis and the coverage of MSG-1, GOES-16 and IMERG. The elevation of (b) Ecuador and (c) Iran.

1.5 Thesis Structure

In order to examine the aforementioned hypothesis in section 1.3, the following working packages were developed. An overview of the complete thesis structure is provided in Figure 1.2.

WP1 development of a high spatio-temporal resolution satellite-based product for MSG SEVIRI (15 minutes, 3 km^2) and GPM IMERG for Iran using random forest. The algorithm relies on precipitation information from the IMERG and multispectral IR data from the MSG-1 satellites.

WP2 transfer the algorithm developed in WP1 to Ecuador with different climatic and orographic patterns and other geostationary satellite data (GOES-16).

WP3 identifying inaccuracy in the developed product by validation with ground-based observations on a sub-daily timescale.

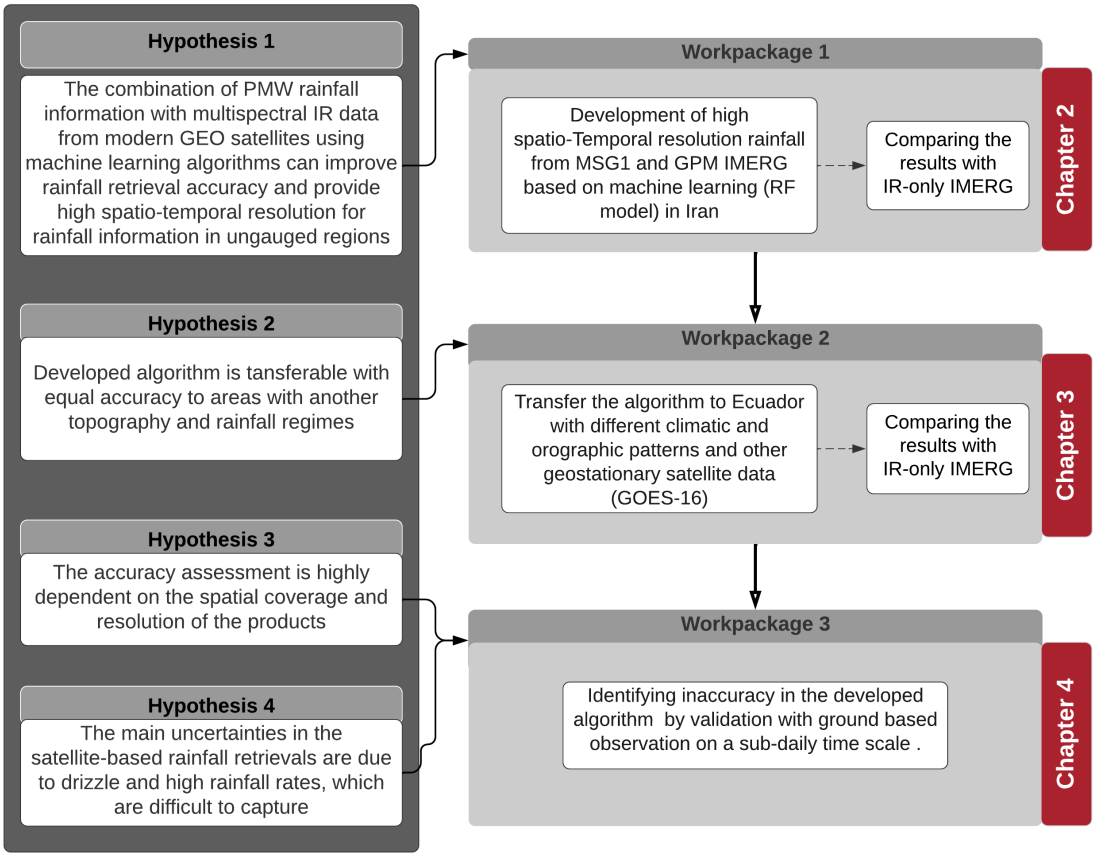

Figure 1.2: Thesis structure of hypothesis, working packages and related chapters.

WP1 was conceptualized to answer Hypothesis 1. Iran's complex topography and semiarid climate was selected as a case study for developing a new satellite-based algorithm for rainfall retrieval in high spatio-temporal resolution (3 km^2, 15 minutes) applying the RF. The algorithm was based on the IR bands of MSG SEVIRI (Chapter

2) and GPM IMERG (chapter 2.2.3). RF models using microwave-only rainfall information from the GPM IMERG product as a reference were developed to (i) delineate the rainfall area and (ii) assign the rainfall rate (Section 2.2.6). The most important predictors and hyperparameter tuning parameters were selected for each month, considering the seasonal variability of rainfall (Section 2.2.6). The positive validation results against independent MW-based IMERG, gauge data, and the IR-only IMERG led to Hypothesis 2 regarding the transferability of the developed algorithms to other areas with different topography and rainfall characteristics. Therefore, WP2 was conceptualized to answer Hypothesis 2.

In WP2, I transferred the satellite-based rainfall retrieval developed in WP1 to Ecuador (Chapter 3). Ecuador was chosen as a perhumid region with complex topography to examine the algorithm's applicabiliry and accuracy in another part of the world. The feature selection and tuning of the RF models (Section 3.2.3.1) for Ecuador was redone since the region has other climatic orographic patterns compared with Iran and a different geostationary satellite (GOES-16- Section 3.2.4.1). The positive results obtained with the developed algorithm in WP2 proved the applicability of rainfall-retrieval algorithm in different world regions. Similar to WP1, the results showed that using multi-spectral IR data improves the retrieval performance compared with single-spectrum IR approaches; however, the results still indicate uncertainties for the Andes' high elevation. The availability of the Radarnet-Sur network [46] in Ecuador empowered to investigate the uncertainty structure of the algorithm over complex topography in more detail using a high spatio-temporal resolution gauge and weather radar data. Therefore, in this WP3, I evaluated the performance of MW-based IMERG compared to RF-based rainfall and IR-only IMERG to characterize the impact of climatic and topographic conditions on satellite-based rainfall products at the time of MW overpass. This validation was performed against high spatio-temporal resolution data from ground-based radar networks and meteorological stations in a high temporal resolution. Therefore, WP3 was conceptualized to answer Hypotheses 3 and 4.

This thesis consists of three manuscripts comprising Chapters 2, 3 and 4 as the core and consitutes significant contributions to the SaWaM project funded by Global Resource Water (GRoW)-BMBF to fill the gap between local and global models and to support SDG-6. All of the manuscripts are published in peer-review journals. Chapter 5 summarizes the research findings providing answers to the hypotheses proposed in section 1.5. Finally a brief outlook for further investigation is presented.

References

[1] Prajal Pradhan et al. "A Systematic Study of Sustainable Development Goal (SDG) Interactions". In: *Earth's Future* 5.11 (2017), pp. 1169–1179. DOI: https://doi.org/10.1002/2017EF000632. eprint: https://agupubs.onlinelibrary.wiley.com/doi/pdf/10.1002/2017EF000632. URL: https://agupubs.onlinelibrary.wiley.com/doi/abs/10.1002/2017EF000632.

[2] UNESCO. "The United Nations World Water Development Report 2015: Water for a Sustainable World". In: *WWAP (United Nations World Water Assessment Programme)* (2015). eprint: https://www.unwater.org/publications/world-water-development-report-2015/.

[3] Anik Bhaduri et al. "Achieving Sustainable Development Goals from a Water Perspective". In: *Frontiers in Environmental Science* 4 (2016), p. 64. ISSN: 2296-665X. DOI: 10.3389/fenvs.2016.00064. URL: https://www.frontiersin.org/article/10.3389/fenvs.2016.00064.

[4] Joseph L Awange et al. "Uncertainties in remotely sensed precipitation data over Africa". In: *International Journal of Climatology* 36.1 (2016), pp. 303–323.

[5] J. Marshall Shepherd. "A Review of Current Investigations of Urban-Induced Rainfall and Recommendations for the Future". In: *Earth Interactions* 9.12 (2005), pp. 1–27. DOI: 10.1175/EI156.1. URL: https://journals.ametsoc.org/view/journals/eint/9/12/ei156.1.xml.

[6] Xiaoying Yang et al. "Nine-year systematic evaluation of the GPM and TRMM precipitation products in the shuaishui river basin in east-central china". In: *Remote Sensing* 12.6 (2020), p. 1042.

[7] Mohammed H I Dore. "Climate change and changes in global precipitation patterns: what do we know?" en. In: *Environ. Int.* 31.8 (Oct. 2005), pp. 1167–1181.

[8] Miguel Laverde-Barajas et al. "St-corabico: A spatiotemporal object-based bias correction method for storm prediction detected by satellite". In: *Remote Sensing* 12.21 (2020), p. 3538.

[9] Christof Lorenz and Harald Kunstmann. "The hydrological cycle in three state-of-the-art reanalyses: Intercomparison and performance analysis". In: *Journal of Hydrometeorology* 13.5 (2012), pp. 1397–1420.

[10] Wouter Buytaert et al. "Assessment and management of water resources in developing, semi-arid and arid regions". In: *Water Resources Management* 26.4 (2012), pp. 841–844.

[11] C Kidd and V Levizzani. *Status of satellite precipitation retrievals*. 2011.

[12] George J Huffman et al. *The TRMM Multisatellite Precipitation Analysis (TMPA): Quasi-Global, Multiyear, Combined-Sensor Precipitation Estimates at Fine Scales*. 2007.

[13] Veljko Petković and Christian D. Kummerow. "Understanding the Sources of Satellite Passive Microwave Rainfall Retrieval Systematic Errors Over Land". In: *Journal of Applied Meteorology and Climatology* 56.3 (2017), pp. 597–614. DOI: 10.1175/JAMC-D-16-0174.1. URL: https://journals.ametsoc.org/view/journals/apme/56/3/jamc-d-16-0174.1.xml.

[14] GJ Huffman et al. *NASA Global Precipitation Measurement (GPM) Integrated Multi-satellitE Retrievals for GPM (IMERG) Algorithm Theoretical Basis Document (ATBD) Version 5.2. 2018*. 2011.

[15] Margaret Wambui Kimani, Joost C. B. Hoedjes, and Zhongbo Su. "An Assessment of Satellite-Derived Rainfall Products Relative to Ground Observations over East Africa". In: *Remote Sensing* 9.5 (2017). ISSN: 2072-4292. DOI: 10.3390/rs9050430. URL: https://www.mdpi.com/2072-4292/9/5/430.

[16] C. Kidd. *Satellite rainfall climatology: a review*. 2001. DOI: https://doi.org/10.1002/joc.635. eprint: https://rmets.onlinelibrary.wiley.com/doi/pdf/10.1002/joc.635. URL: https://rmets.onlinelibrary.wiley.com/doi/abs/10.1002/joc.635.

[17] Steven J Goodman. "GOES-R series introduction". In: *The GOES-R Series*. Elsevier, 2020, pp. 1–3.

[18] Johannes Schmetz et al. "AN INTRODUCTION TO METEOSAT SECOND GENERATION (MSG)". In: *Bull. Am. Meteorol. Soc.* 83.7 (July 2002), pp. 977–992.

[19] Ali Behrangi et al. "REFAME: Rain Estimation Using Forward-Adjusted Advection of Microwave Estimates". In: *Journal of Hydrometeorology* 11.6 (2010), pp. 1305–1321. DOI: 10.1175/2010JHM1248.1. URL: https://journals.ametsoc.org/view/journals/hydr/11/6/2010jhm1248_1.xml.

[20] Yang Hong et al. "Precipitation estimation from remotely sensed imagery using an artificial neural network cloud classification system". In: *Journal of Applied Meteorology* 43.12 (2004), pp. 1834–1853.

[21] Chris Kidd et al. "Satellite rainfall estimation using combined passive microwave and infrared algorithms". In: *Journal of Hydrometeorology* 4.6 (2003), pp. 1088–1104.

[22] Soroosh Sorooshian et al. *Evaluation of PERSIANN System Satellite–Based Estimates of Tropical Rainfall*. 2000.

[23] Robert J. Kuligowski. "A Self-Calibrating Real-Time GOES Rainfall Algorithm for Short-Term Rainfall Estimates". In: *Journal of Hydrometeorology* 3.2 (2002), pp. 112–130. DOI: 10.1175/1525-7541(2002)003<0112:ASCRTG>2.0.CO;2. URL: https://journals.ametsoc.org/view/journals/hydr/3/2/1525-7541_2002_003_0112_ascrtg_2_0_co_2.xml.

[24] S. W. Miller, P. A. Arkin, and R. Joyce. "A combined microwave/infrared rain rate algorithm". In: *International Journal of Remote Sensing* 22.17 (2001), pp. 3285–3307. DOI: 10.1080/01431160152609155. eprint: https://doi.org/10.1080/01431160152609155. URL: https://doi.org/10.1080/01431160152609155.

[25] Gilberto A Vicente, Roderick A Scofield, and W Paul Menzel. "The operational GOES infrared rainfall estimation technique". In: *Bulletin of the American Meteorological Society* 79.9 (1998), pp. 1883–1898.

[26] Robert J Joyce et al. *CMORPH: A Method that Produces Global Precipitation Estimates from Passive Microwave and Infrared Data at High Spatial and Temporal Resolution*. 2004.

[27] George J Huffman et al. "NASA global precipitation measurement (GPM) integrated multi-satellite retrievals for GPM (IMERG)". In: *Algorithm theoretical basis document, version* 4 (2015), p. 30.

[28] C. Kummerow et al. "An observationally generated a priori database for microwave rainfall retrievals". In: *J. Atmos. Oceanic Technol.* 28 (2011), pp. 113–130.

[29] C. Kummerow et al. "The evolution of the Goddard Profiling algorithm to a fully parametric scheme". In: *J. Atmos. Oceanic Technol.* 32 (2015), pp. 2265–2280.

[30] R. F. Adler. "The version-2 Global Precipitation Climatology Project (GPCP) monthly precipitation analysis (1979–present)". In: *J. Hydrometeor.* 4 (2003), pp. 1147–1167.

[31] Robert J Joyce and Pingping Xie. "Kalman filter–based CMORPH". In: *Journal of Hydrometeorology* 12.6 (2011), pp. 1547–1563.

[32] Phu Nguyen et al. "The PERSIANN family of global satellite precipitation data: A review and evaluation of products". In: *Hydrology and Earth System Sciences* 22.11 (2018), pp. 5801–5816.

[33] Jackson Tan, Walter A Petersen, and Ali Tokay. "A novel approach to identify sources of errors in IMERG for GPM ground validation". In: *Journal of Hydrometeorology* 17.9 (2016), pp. 2477–2491.

[34] Marlon Maranan et al. "A process-based validation of GPM IMERG and its sources using a mesoscale rain gauge network in the West African forest zone". In: *Journal of Hydrometeorology* 21.4 (2020), pp. 729–749.

[35] Meike Kühnlein et al. "Precipitation Estimates from MSG SEVIRI Daytime, Nighttime, and Twilight Data with Random Forests". In: *J. Appl. Meteorol. Climatol.* 53.11 (Nov. 2014), pp. 2457–2480.

[36] Meike Kühnlein et al. "Improving the accuracy of rainfall rates from optical satellite sensors with machine learning—A random forests-based approach applied to MSG SEVIRI". In: *Remote Sens. Environ.* 141 (2014), pp. 129–143.

[37] Hanna Meyer, Johannes Drönner, and Thomas Nauss. *Satellite based high resolution mapping of rainfall over Southern Africa.* 2017.

[38] M Min et al. "Estimating Summertime Precipitation from Himawari-8 and Global Forecast System Based on Machine Learning". In: *IEEE Trans. Geosci. Remote Sens.* 57.5 (May 2019), pp. 2557–2570.

[39] Hanna Meyer et al. "Comparison of four machine learning algorithms for their applicability in satellite-based optical rainfall retrievals". In: *Atmospheric research* 169 (2016), pp. 424–433.

[40] Niklas Boers et al. "Complex networks identify spatial patterns of extreme rainfall events of the South American Monsoon System". In: *Geophysical Research Letters* 40.16 (2013), pp. 4386–4392.

[41] Mathias Vuille, Raymond S Bradley, and Frank Keimig. "Climate variability in the Andes of Ecuador and its relation to tropical Pacific and Atlantic sea surface temperature anomalies". In: *Journal of climate* 13.14 (2000), pp. 2520–2535.

[42] Bastian Manz et al. "Comparative ground validation of IMERG and TMPA at variable spatiotemporal scales in the tropical Andes". In: *Journal of Hydrometeorology* 18.9 (2017), pp. 2469–2489.

[43] S Javanmard et al. *Comparing high-resolution gridded precipitation data with satellite rainfall estimates of TRMM_3B42 over Iran.* 2010.

[44] Pari-Sima Katiraie-Boroujerdy et al. "Evaluation of satellite-based precipitation estimation over Iran". In: *J. Arid Environ.* 97 (Oct. 2013), pp. 205–219.

[45] Elham Ghasemifar et al. "Precipitation rate climatology related to different cloud types using satellite imagery over Iran". In: *Arabian Journal of Geosciences* 11.4 (2018), pp. 1–15.

[46] Jörg Bendix et al. "RadarNet-Sur first weather radar network in tropical high mountains". In: *Bulletin of the American Meteorological Society* 98.6 (2017), pp. 1235–1254.

Chapter 2

Estimating high spatio-temporal resolution rainfall from MSG1 and GPM IMERG based on machine learning: case study of Iran

Nazli Turini [1,*], Boris Thies [1] and Jörg Bendix [1]

[1] Laboratory for Climatology and Remote Sensing, Faculty of Geography, Philipps-Universität Marburg, 35037 Marburg, Germany

---

This chapter is printed in ***Remote Sensing, 11(19), 2307***, DOI: https://doi.org/10.3390/rs11192307

Abstract

A new satellite-based technique for rainfall retrieval in high spatio-temporal resolution (3 km, 15 min) for Iran is presented. The algorithm is based on the infrared bands of the Meteosat Second Generation Spinning Enhanced Visible and Infrared Imager (MSG SEVIRI). Random forest models using microwave-only rainfall information of the Integrated Multi-SatEllite Retrieval for the Global Precipitation Measurement (GPM) (IMERG) product as a reference were developed to (i) delineate the rainfall area and (ii) to assign the rainfall rate. The method was validated against independent microwave-only GPM IMERG rainfall data not used for model training. Additionally, the new technique was validated against completely independent gauge station data. The validation results show a promising performance of the new rainfall retrieval technique, especially when compared to the GPM IMERG IR-only rainfall product. The standard verification scored an average Heidke Skill Score of 0.4 for rain area delineation and an average R between 0.1 and 0.7 for rainfall rate assignment, indicating uncertainties for the Lut Desert area and regions with high altitude gradients.

Keywords: Meteosat; satellite; rainfall retrieval, Random Forest, GPM, IMERG, semi arid areas,Iran

2.1 Introduction

In semi-arid areas, the limited water availability from rainfall poses problems for agriculture and forestry (food and timber products), potable water supply, and energy production by hydro-power via dams. Climate change studies generally point to a reduction of rainfall, especially in semi-arid areas [1], which will most likely aggravate water scarcity in the future. This also holds for the arid and semi-arid regions of Iran, where the signal is strongly varying on the local scale [2, 3, 4, 5, 6]. To monitor changes in rainfall availability, accurate rainfall estimation at fine spatio-temporal resolution is important for water resource management. Thus, a dense ground observation network is also a precondition for proper hydrological modeling. Most arid and semi-arid regions are characterized by few precipitation gauge stations. Iran, where more than 60% of the country is composed of semi-arid regions, is facing two challenges: a strong information demand for water security on the one, confronted with a coarse network of operational rainfall gauges on the other. For this reason, in Iran but also in many other arid and semi-arid regions, satellite rainfall products are the only source providing area-wide precipitation observations in space and time, which renders them potentially attractive for hydrological management in ungauged basins [7]. However,

their applicability in hydrology depends on the quality of the satellite data and the rainfall retrieval method used. Several products exist to derive rainfall from passive single or multi-spectral infrared (IR) sensors, passive microwave sensors, active radar instruments, and data fusion algorithms merging microwave and radar data with IR on geostationary satellites globally (e.g. TRMM [8]; CMORPH [8, 9]; PERSIANN [10]).

Several studies in global rainfall-retrieval inter-comparison missions showed that the microwave and radar-based fusion systems are for the most part superior to purely passive IR techniques, and are particularly superior to rainfall-satellite-based models [11]. Data fusion algorithms increasingly include the GEO-IR (Geostationary Orbit, InfraRed) data, as well as the newest generation of global products, the Integrated Multi-SatEllite Retrieval (IMERG) for the Global Precipitation Measurement Mission (GPM) [12]. GPM was started in 2014 as a new generation of rainfall retrieval as a post-TRMM (Tropical Rainfall Measuring Mission) joint US–Japan mission. The GPM provides multi-channel, dual polarization passive microwave sensors and active scanning radar. The improvements of GPM in comparison to TRMM are: (i) The orbital inclination has been expanded from 35° to 65° to cover more important additional climate zones. (ii) Upgrading the precipitation radar to two frequencies, Ku band (13.6 GHz) and Ka-band (35.5 GHz). Anticipated advantages include a better sensitivity to light precipitation, and information on the particle size distribution in rain and snow. (iii) A GPM Microwave Imager (GMI) with a higher spectral resolution at frequencies of 10.65, 18.7, 23.8, 26.5, 89, 165.5, and 183.3 GHz [13]. Compared to TRMM, GMI was improved particularly by adding high-frequency channels (165.5 and 183.3 GHz) which lead to a better sensibility to light and solid precipitation [12]. However, the integration of GEO-IR data in IMERG is limited to only one thermal band at 10.7 µm, due to the difficulties in handling the data volume of multi-spectral GEO retrievals from various GEO platforms around the globe, and the limitation of visible data to daylight hours [12]. Despite the generally lower accuracy of an IR-based rainfall retrieval, the use of comprehensive IR data for rainfall retrieval—even in data fusion schemes—has been highly recommended based on the experience of the IPWG (International Precipitation Working Group) rainfall retrieval missions [14], particularly due to its high temporal resolution.

On the regional scale, however, regionally adapted algorithms using only passive IR data from geostationary orbit (GEO) revealed good accuracy, particularly when the full spectrum of available bands in combination with machine learning techniques

were used [7, 15, 16, 17, 18, 19, 20]. The main advantage of GEO systems for rainfall retrieval is the high temporal resolution (15–30 min image repetition), which is lacking for passive microwave and radar sensors, perfectly matching the short-term characteristics of rainfall systems.

Concerning the incorporation of geostationary IR data in satellite-based rainfall retrieval algorithms, machine learning techniques are used extensively to identify relationships between predictor variables and rainfall estimates [10, 19, 21, 22, 23, 24, 25, 26]. They offer a high potential in dealing with non-linear and complex relationships between the variables, but also with highly correlated predictor variables [20]. In recent years there has been considerable interest in the application of random forest (RF) in rainfall retrieval techniques [17, 18, 27, 28]. RF is usable as a classification and regression technique and produces more accurate predictions than single-tree algorithms [29]. It offers a number of features compared to other machine learning algorithms that make it suitable for application in the remote sensing of rainfall: (i) It handles large data sets efficiently, while for example neural networks (NNETs) are not efficient in dealing with high-dimensional data without reducing the dimensions [30]. (ii) It has the potential to select predictors and define which are the most important. (iii) It has high accuracy in classification, while it is difficult to ensure classification accuracy with support vector machines (SVMs) for multi-class problems [30]. (iv) There is no need for complex data processing beforehand [30]. Islam et al. [27] classified rainfall areas from a satellite-borne passive microwave radiometer using RF classification. Kühnlein et al. [17],Kühnlein et al. [18] modeled rainfall in Germany using RF, and trained MSG1 data with ground-based radar data. Both obtained promising results for the use of RF in rainfall retrieval. Min et al. [28] recently used Himawari-8 and GPM data to model rainfall using RF. Meyer et al. [20] compared different machine learning techniques (neural network, averaged neural network, support vector machine, and random forest) for satellite-based rainfall retrieval. They concluded that all of them are well suited for satellite-based rainfall retrieval, and none of them were significantly better than the others.

Several studies have applied the above-mentioned globally available data sets to Iran and compared the performance with gauge data. An intercomparison of PERSIANN and TRMM-based products showed the superior performance of the TRMM-based products, but still found some underestimations and bias problems [31, 32] . PODs (probabilities of detection) of 40% and less were achieved, depending on the region. A bias correction could be applied to slightly improve the quantitative precipitation

assessment results [33]. In a recent study in Iran, it could be shown that the new IMERG product outperformed TRMM-based products and ERA-Interim reanalysis rainfall particularly for orographic, stratiform, and heavy precipitation [34]. However, the authors stressed that the occurrence of over- and underestimations indicated a remaining challenge of reliable satellite-based rainfall retrieval in Iran. They emphasized that the limited spatio-temporal coverage of data in the algorithm (e.g., limited MW/radar and operational rain gauge network) in comparison to the complex topography, as well as the high spatio-temporal variability of rainfall in the semi-arid area, were most likely the main reason for the obtained inaccuracies.

Thus, the main aim of the current study was to combine the advantages of second-generation GEO systems and the new IMERG product in order to develop a regionally adapted rainfall retrieval scheme with high temporal resolution based on a machine learning algorithm. In detail, we used the Meteosat Second Generation (MSG) SEVIRI (Spinning Enhanced Visible and InfraRed Imager) multispectral radiances and RF algorithm, and the RF model was regionally trained using passive microwave (sounder and imager) rainfall from GPM IMERG. However, RF model training was restricted to areas and time slots where the best microwave quality of IMERG was available. The area validation of the applied RF model rainfall products was also conducted for pixels from microwave-based IMERG, but for pixels that were independent from the model training data set. The same was true for RF model product point validations with available weather station data, which were not used in the generation of the IMERG product and were thus completely independent.

2.2 Data and Method

This section firstly describes the general rainfall retrieval method (section 2.2.1). Then, we give an overview of the data sets that were used (section 2.2.2, 2.2.3, 2.2.4). After that, we describe the RF model generation and the final rainfall retrieval model in detail (section 2.2.5, 2.2.6, 2.2.7 and 2.2.8).

2.2.1 Rainfall Retrieval Development

The aim of this study was to develop a new satellite rainfall product by combining the available microwave-based GPM IMERG rainfall information, which has the advantage of accurate rainfall estimates, with the high spatio-temporal resolution of

MSG. Toward this end, the new rainfall retrieval algorithm is based on the IR bands of MSG1 and trained with the best microwave-quality data of the IMERG product (i.e., microwave-based IMERG). The general workflow is depicted in Figure 2.1. The basic principle of this algorithm is first to delineate the rainfall area within cloudy regions with an RF classification. In the second step, this information is then used to estimate the rainfall amount with a RF regression model. These two steps are implemented following previous studies which showed promising results for central Europe and other areas [17, 19, 28, 35].

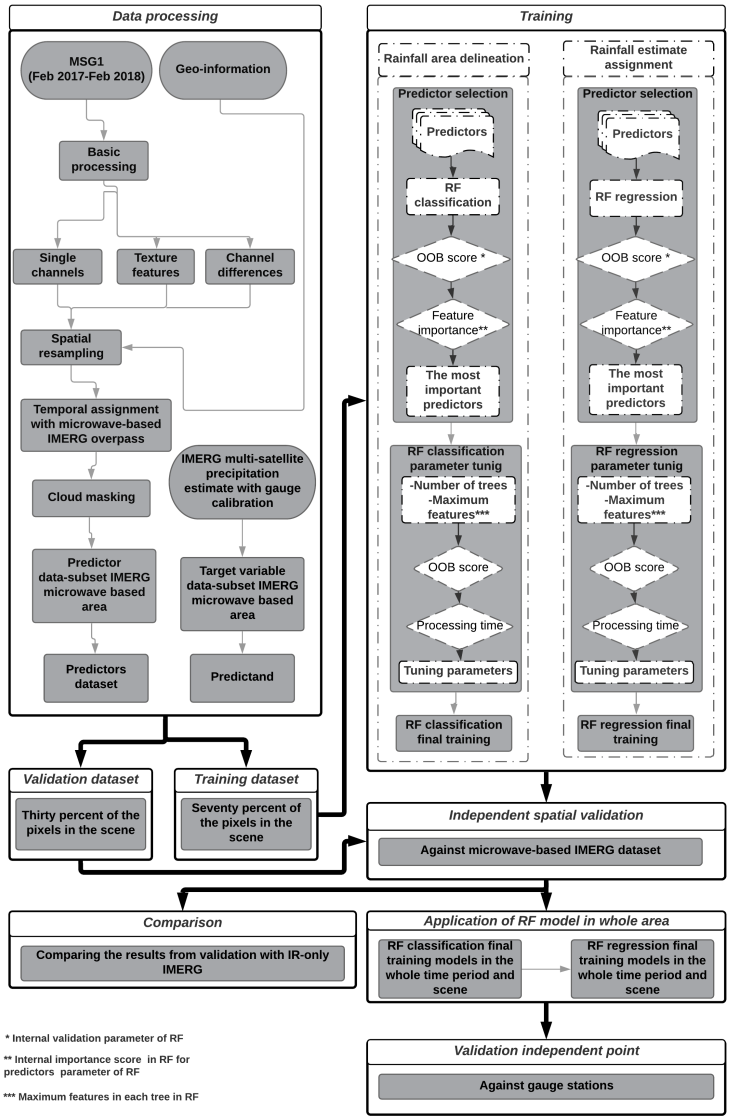

Figure 2.1: Schematic view of the rainfall retrieval workflow.

The work flow of the development of the new rainfall retrieval method is depicted in Figure 2.1. First, the RF model predictors had to be matched to a spatio-temporal homogenous data set: (i) MSG1 SEVIRI IR-channels, (ii) its spatial texture features, (iii) channel differences, and (iv) ancillary geo-information data were processed and collected for areas and time slots that were also covered by the microwave-based IMERG products (rain area and rate) (section 2.2.5) (Figure 2.1, left). The data were used to train and develop the two RF-models: (i) The RF classification to delineate rainy and no-rain cloud areas (Figure 2.1 left, in section 2.3.2.1), and (ii) the RF regression model to estimate rainfall (Figure 2.1, right, in section 2.3.2.2). The training of rainfall area delineation and rainfall estimate assignment were done independently.

Both best-trained RF-models were applied to the study area (Figure 2.2) and the resulting rain area/amounts were validated against an independent microwave-only IMERG dataset from regions which were not used during the training process (see section 2.3.2.3). Finally, the RF-models were applied to the whole time period of available MSG-SEVIRI data in the original spatial and temporal resolution (15 min) of MSG1. Because the first validation was conducted with IMERG (even with pixels not involved in training), a second, completely independent, validation of the RF rainfall estimate was conducted against gauge stations which were neither part of the IMERG product nor used for model training (see section 2.3.2.4). Note that the term "feature" that is generally used in RF models has the same meaning as "predictor".

2.2.2 Predictor Dataset

The rainfall retrieval model presented here uses the IR wavelengths (all bands between 3.9 and 14 μ) from MSG1 SEVIRI. Processing was performed using software developed by Drönner et al. [36]. In addition to the MSG1 data, the cloud mask (CLM) product [37], which is mainly based on the MSG SEVIRI data, was used to outline the domain for cloudy pixels that was used for training the RF models. Several IR bands from MSG1 SEVIRI and different band combinations (DIF) that have been proven to improve the rainfall estimation by satellites were included as predictors [18, 35]. This also holds for the spatial variability in the spectral bands and DIFs [38, 39, 40, 41], where respective metrics were also included as predictors for the RF models. Different texture features were calculated from a 3×3 pixel moving window approach: For the single bands (i) variograms (VARs), (ii) madograms (MADs), (iii) rodograms (RODs) and (iv) cross-variograms (CVs), as well as (v) pseudo cross-variograms (PCs) of each

channel combination [39].

Besides that, an increasing number of studies found that mountainous regions in semi-arid areas are one of the great challenges regarding rainfall satellite retrievals both, in IR and microwave products. This is due to the high weather variability [42] related to the topographic forcing of rainfall formation and decay. Similar conclusions are also drawn for low and mid-elevation areas of Iran [32, 33, 43, 44, 45]. Due to the importance of topography for rain formation, (i) terrain elevation (ELV), (ii) the Topographic Position Index (TPI), (iii) the Topographic Roughness Index (TRI), (iv) slope and (v) aspect were also added as predictors to the training data set. The predictors are derived from the Global 30 Arc-Second Elevation DEM [46]. The list of predictors that are used in this study is depicted in Table 2.1.

Table 2.1: All predictors initially used for rainfall retrieval development. MSG bands are shown with their central wavelength in μ. CV: cross-variogram; ELV: terrain elevation; MAD: madogram; PCV: pseudo CV; ROD: rodogram; TPI: Topographic Position Index; TRI: Topographic Ruggedness Index; VAR: variogram. ΔT indicates the temperature band differences. WV: Wave Length.

MGS band	Derived data	Ancillary geo-information
IR 3.9	ΔT (all band combination)	ELV
WV 6.2	VAR (all bands)	TPI
WV 7.3	MAD (all bands)	TRI
IR 8.7	ROD (all bands)	Slope
IR 9.7	CV (all band combination)	Aspect
IR 10.8	PCV (all band combination)	

2.2.3 GPM IMERG Training and Validation Data

To train and validate the RF model developments for rain area and amount against the predictors (section 2.2.2, Table 2.1), we used the microwave-based rainfall estimates from the IMERG product only. IMERG is a level-3 gridded precipitation product from the GPM constellation. It calibrates, merges, and interpolates the measurements from a network of satellites, together with a precipitation gauge analysis every half hour in 0.1° spatial resolution [47]. IMERG is designed to use as many low Earth orbit (LEO) satellites as possible to compensate for the limitations in available satellite microwave precipitation estimates as effectively as possible, in conjunction with IR estimates from GEO satellites. IMERG has three runs to provide different

user requirements for latency and accuracy. This study focuses on the final run of 30-min IMERG Version 05 (IMERG-V05), using the gauge-adjusted estimates from 12 months of data between February 2017 and February 2018. Since IMERG-V05, the quality index (QI) is included as a new variable with half-hourly resolution in the metadata provided by NASA [47]. The QI is a metric concerning the relative skill of the temporally fluctuating mix of different passive-microwave-and IR-based rainfall estimates in half-hourly IMERG products. Additionally, the time of the overpass of each microwave swath in each scene is also available under the flag HQ observation. For the rainfall retrieval model development, the microwave-based pixels from the multi-satellite precipitation estimates with the gauge calibration sub-dataset of IMERG was used for training and validation. The final compiled data set (including predictor and target variable dataset) was selected on cloudy pixels, where the high-quality IMERG data was available (QI $>$ 90%). Seventy percent of the compiled dataset in each scene was randomly selected as the training dataset, and thirty percent of the remaining pixels in the scene were selected for validation.

2.2.4 Station Data for Independent Point Validation

Precipitation gauge data for February 2017 till January 2018 were obtained from the Islamic Republic of Iran Meteorological Organization (IRIMO) for Khouzestan and Urmia provinces. These data are independent of the gauges used for the IMERG calibration, and are in two different recorded time steps. One group consists of the rainfall in every 6 hours, and another group records data at a daily scale. They were complemented by the data derived from the Urmia Lake Restoration Program (`ULRP.sharif.ir/en`). The data from both organizations underwent quality checks before they were delivered. The distribution of rainfall gauge stations used in this study is shown in Figure 2.2.

2.2.5 Data Processing

With reference to Figure 2.1, our new rainfall retrieval was done in five steps. The first step included data processing. The different temporal and spatial characteristics of MSG1 data (15 min; 3 by 3 km^2 at the sub-satellite point) and IMERG (30 min; 11 by 11 km^2) were addressed to ensure pixel matching between Meteosat, geo-information, CLM, and IMERG data. Thus, MSG1, CLM, and geo-information data were projected and resampled (average) to the spatial resolution of IMERG.

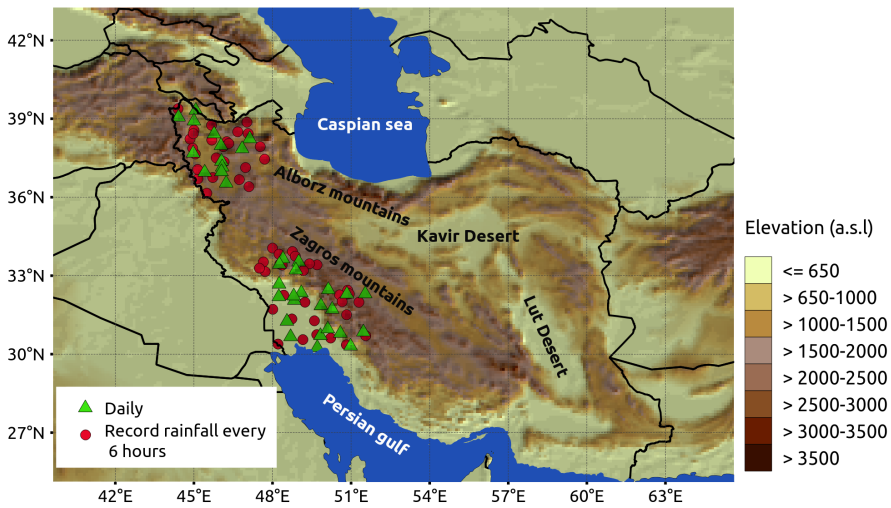

Figure 2.2: Distribution of available rainfall gauge station in the study area.

Because MSG feature and IMERG training data can temporally deviate by hours, the temporal overlap of <7 min was used to ensure proper comparability between both data groups. A seven-minute threshold was determined as an average acquisition time between the MSG1 scan in Iran (occurring between minutes 7 and 10 for each full disk scan of Earth with MSG1) and HQ observation time overpass of IMERG. Then, the QI was used to mask out the microwave-based-only pixels from the entire IMERG data set. Finally, the CLM product was used to limit the training data sets to areas where precipitation is generally possible, as indicated by cloudiness. However, it should be stressed that for the training of the RF models, only pixels with rain rates higher than 0.2 mm/h were considered as rainy, warranting reliable information on rainfall in IMERG [12, 48]. This threshold was chosen due to the estimated minimum detectable rain rates of the Ka- and Ku-band radars [49]. After the last step of preprocessing, a consistent data set for training and validation of the RF models was compiled.

2.2.6 Model Training and Tuning

The first step for the training of the RF models was the selection of the most important predictors. This involved a reduction to the best-performing predictor sets out of the initial feature data space presented in Appendix 2.A. Here, the predictor selection was conducted by applying a recursive feature elimination (RFE) for each month of the training dataset. RFE started with all of the initial 121 predictors and removed

the least significant ones using the feature importance metrics of the RF methods [29]. IIn each step of this iterative RFE procedure, the model quality was calculated using the out-of-bag (OOB) score. The OOB score was measured during model fitting based on the left out data (one-third of the observations) for each tree in the RF [50, 51]. The set of predictors with the best average ranking (sorted based on feature importance) that reached the highest OOB score was filtered from the original set of 121 (Appendix 2.A) for each month and used as the training input for the final RF models.

With the completion of the RFE step, we iteratively tuned the hyperparameters, including the total number of decision trees and the number of input features (n) used at each node to get the optimal setting for the RF classification and regression model in each month, following the successful approach of different studies [18, 28, 39] for RF model training. For each parameter set, RF models were trained based on the tuning data set and the OOB score was calculated. In addition, the balance parameter in the RF package "compute sample weight" from Scikit-learn 0.20.2 [52] in Python 2.7 was also implemented for both RF regression and classification.

o save computation time for RFE and parameter tuning, we randomly selected the data from the whole training dataset. For rainfall area delineation, 10,000 pixels from the available training pixels in the month were randomly selected including 2000 rainy and 8000 cloudy pixels. For the rainfall estimate RFE parameter tuning, we randomly selected 2000 rainy pixels in each month. It should be stressed that the distribution of rainfall rate within a month varies and RF regression models are not able to predict unbalanced datasets [28]. Therefore, in order to increase the rainfall prediction accuracy, the balanced sampling technique [28] was used for RFE and parameter tuning of the RF regression. For each month, the rainfall rate was classified with the range of 1 mm/h and the probability of occurrence of every rain rate class was calculated for each tuning data set. The class with the average probability of occurrence (APO) was selected and the new sample stemmed from the original sample by simply decreasing the low rain rate sample to the APO. Fifty runs were performed for both RFE and parameter tuning to produce fifty series of a randomly selected pixel for each month. Differences between these fifty realizations reflected the whole range of internal variability of the microwave-based IMERG in the region and in the month.

2.2.7 Application of the Rainfall Retrieval Model

After the successful adjustment of the microwave-based IMERG models for rainfall area delineation and rainfall rate assignment, each 15-min image from MSG1 was then processed using the best trained models at the microwave-based IMERG resolution of 11 km to generate rainfall estimates with high spatio-temporal resolution. Since the microwave-based IMERG models are limited in time, the range of the available models in a day differs between 3 and 25, depending on the time of year. To generate the rainfall estimates in MSG1 generic resolution, we applied the models in the scene of the same time slot, and the following scenes until the next microwave-based IMERG RF model was available. In cases where the previous model belonged to the last months, the first model in the upcoming months was applied for the scenes, where a model was available.

2.2.8 Validation

In order to assess the model performances, two different validation strategies were employed:

- The performances of the trained rainfall area delineation and rainfall rate assignment models were investigated on a scene-by-scene basis, using 30% of the independent pixels from each scene.
- The overall performance of the rainfall area delineation and rainfall rate assignment was investigated against gauge station after application of the model in the whole study area for the whole time period.

First, the performance of the rainfall area delineation and rainfall rate assignment on a scene-by-scene routine was investigated after training the model. By extracting the data pairs of the validation data sets on a pixel basis, a total of 287,750 pairs of RF classification/regression and microwave-based IMERG were made available at a half-hourly resolution for validation. Then, in the next step, the performances of RF models were compared in the same location with sub-dataset IR-only IMERG. With the latter analysis, we could reveal if the new multispectral GEO retrievals were superior to the IR-only IMERG solution.

For the validation of rainfall area delineation, all pixels from the validation dataset that were classified as cloudy by CLM were considered. First, we calculated the crosstables for the RF classification and IR-only IMERG using RF-modeled pixel

values in comparison to the microwave-based IMERG as reference. The hits (H), misses (M), false alarms (F) and correct negatives (C) between each pair of the dataset were calculated. A hit was considered when both the reference and the estimate pixels were raining; a miss was indicated when the reference was raining but the estimate was not; a false alarm occurred when the reference was not raining but the estimate was; and a correct negative was when both the reference and the estimate were not raining. From the hits, misses, false alarms, and correct negatives, we calculated the average half-hourly probability of detection (POD), false alarm ratio (FAR), and Heike skill score (HSS) as validation metrics. The detailed equations and the range of these metrics are shown in Table 2.2. The POD indicates the fraction of correctly

Table 2.2: Validation metrics with equation, theoretical range and optimum value.

Name	**Metrics equation**	**Rang**	**Optimum**
Probability of detection	POD=$\frac{H}{H-M}$	[0,1]	1
False alarm ratio	FAR=$\frac{F}{F-C}$	[0,1]	0
Heike skill score	HSS=$\frac{2(H\times C-F\times M)}{(H-M)(M+C)+(H+F)(F+C)}$	[0,1]	1
Mean absolute error	MAE=$\frac{1}{n}\sum_{i=1}^{n}\lvert P_i - O_i\rvert$	-	-
Root mean square error	RMSE=$\sqrt{\frac{\sum_{i=1}^{n}(P_i-O_i)^2}{n}}$	-	-
Correlation coefficient	$R=\frac{(n\sum_{i=1}^{n}(P_iO_i-(\sum_{i=1}^{n}P_i)(\sum_{i=1}^{n}O_i))}{\sqrt{((n\sum_{i=1}^{n}(P_i^2)-(\sum_{i=1}^{n}(P_i))^2)((n\sum_{i=1}^{n}O_i^2)-(\sum_{i=1}^{n}O_i)^2)}}$	[-1,1]	1

modeled rain pixels. A perfect score is 1. The FAR gives the percentage of estimated pixels incorrectly estimated as rain. A perfect score is 0, implying that the RF classification or the IR-only IMERG never estimate a qualified precipitation rate when the microwave-based IMERG indicates no precipitation. The HSS is a metric for the general model performance that quantifies whether the estimate is worse or better than the microwave-based IMERG. A perfect score is 1. To evaluate the ability of the RF regression model to estimate rainfall, the correlation between the reference dataset and the estimated half hourly rainfall was calculated using the correlation coefficient (R). Root Mean Square Error $(RMSE)$ and the Mean Absolute Error (MAE) were also calculated. All rainy pixels from Microwave based IMERG were used for the validation of rainfall estimate.

2.3 Results

2.3.1 Training Results

In each of these steps, first we selected the most important features (results in section 2.3.1.1), then tuned the hyperparameters for the model development (results in section 2.3.1.2) and finally the RF models were applied. Please note that due to the low availability of rainy pixels in June, training and validation was not possible for this month.

2.3.1.1 Results of Recursive Feature Elimination

RFE results are depicted in 2.3. In Figures 2.3a,c, the average RF classification and

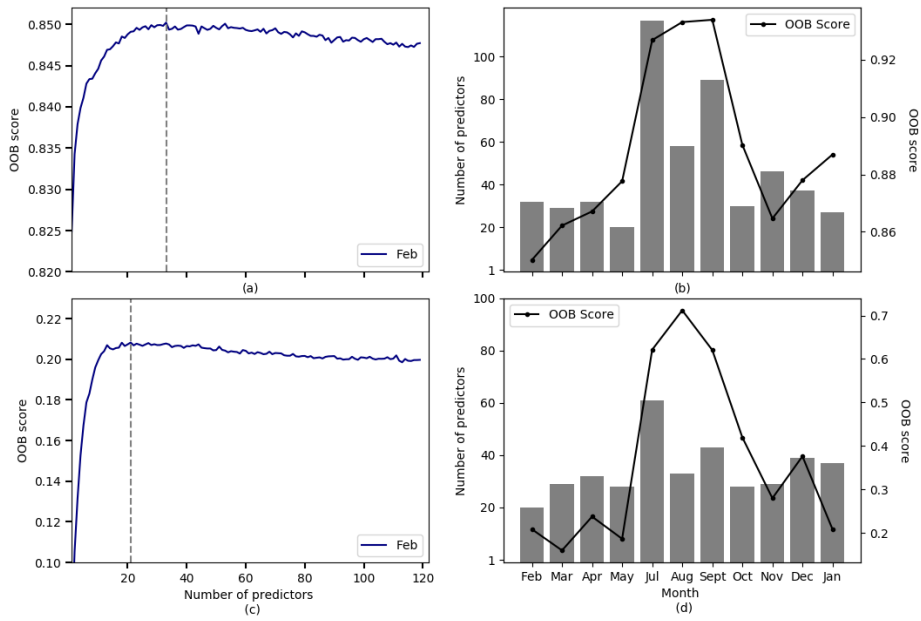

Figure 2.3: Results of the feature elimination. (**a**) OOB score vs Number of features for RF classification (rain area) in February,(**b**) Number of features selected for RF classification and related OOB score for the time period, (**c**) OOB score vs Number of features for RF regression (rain amount) in February, (**d**) Number of features selected for RF regression and related OOB score.

regression in February are respectively shown as examples. The RF classifications for rain are delineated showeing the best model performance with an OOB score of 0.85 at 33 remaining features. The performance of the RF regression model for rain

amount was less pronounced, with the best model performance at an OOB score of around 0.2 and 20 remaining features. In both models, having more features from the set resulted in a worse result. The same process was performed in each month for the whole time period, and the number of features that led to the best RF model performances was defined. The optimum number of features is shown in Figure 2.3b for RF classification and Figure 2.3d for RF regression with respective OOB scores for the study period. The number of features of RF classification in summer (July, August, September) increased significantly. However, July, August, and September showed the highest OOB scores in both RF classification and RF regression.

In the next step, feature importance was used to define the most important predictors considering the optimum number of already-defined predictors.

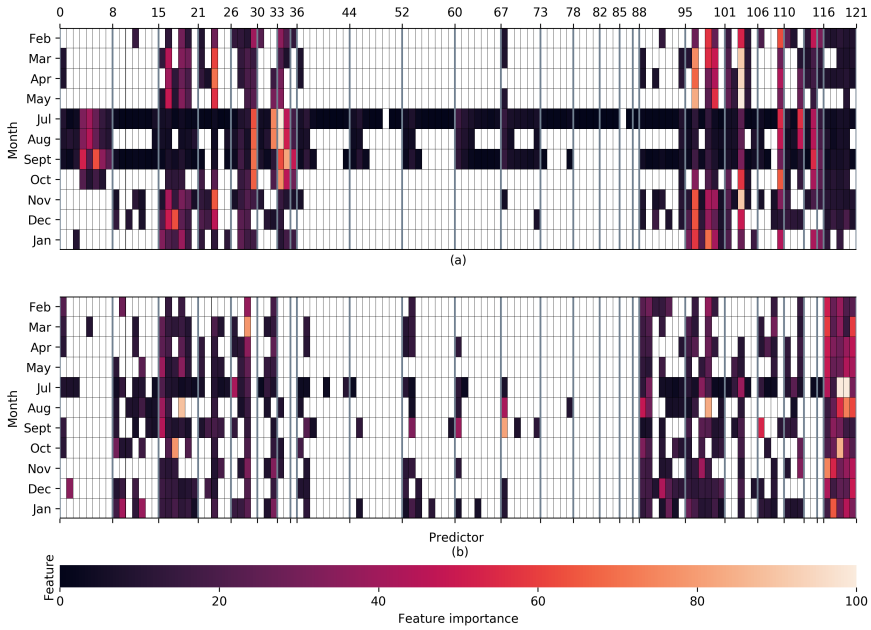

Figure 2.4: Selected predictors and related feature importance for the time period. (**a**) RF classification, (**b**) RF regression. Numbers on the x-axis represent feature IDs (Please refer to Appendix 2.A for the legend and list of features).

Figure 2.4 illustrates the selected predictors and the feature importance for both RF classification and RF regression. In both models, the combination of CV for the IR 8.7 (features 79–82), CV for IR 9.7 (features 83–85), CV for IR 10.8 (features 86 and 87), and CV for IR 12.0 (feature 88) did not play roles at all, except for July which showed greater complexity in the rainfall area delineation due to the lower number of cloudy pixels. This was also true for all MADs (features 45–52). The single channel

of IR 10.8 had a relatively high feature importance in the warm seasons for the RF classification. This channel provides information about the cloud-top temperature, and thus the cloud height [18].

Figure 2.4b shows that the terrain features were identified as having the highest impact in modeling the rainfall amount. Besides that, for both rainfall delineation and rainfall assignment, the ΔT 8.7-10.8 (features 28) and ΔT 10.8-12.0 (features 34) were mostly selected in each month. These band combinations have been proven to provide information about the cloud water path [53] and thus improve rainfall retrieval models [18]. In both models, one or more of the combination of band WV 6.2 with WV 7.3, IR 8.7, IR 9.7, IR 10.8, IR 12.0, and IR 13.4 (features 16–21) was selected in each month. The differences between the brightness temperature in water vapor and IR channels were shown to correspond to deep convective clouds with heavy rainfall [54, 55, 56]. These band combinations have been proven to provide information about the cloud water path [53] and thus improve rainfall retrieval models [18]. In both models, one or more of the combination of band WV 6.2 with WV 7.3, IR 8.7, IR 9.7, IR 10.8, IR 12.0, and IR 13.4 (features 16–21) was selected in each month. The differences between the brightness temperature in water vapor and IR channels were shown to correspond to deep convective clouds with heavy rainfall [54, 55, 56].

2.3.1.2 Parameter Tuning

For RF model training, we tuned the parameters iteratively in order to find an optimal model with regard to the number of decision trees and the number of input features (n).

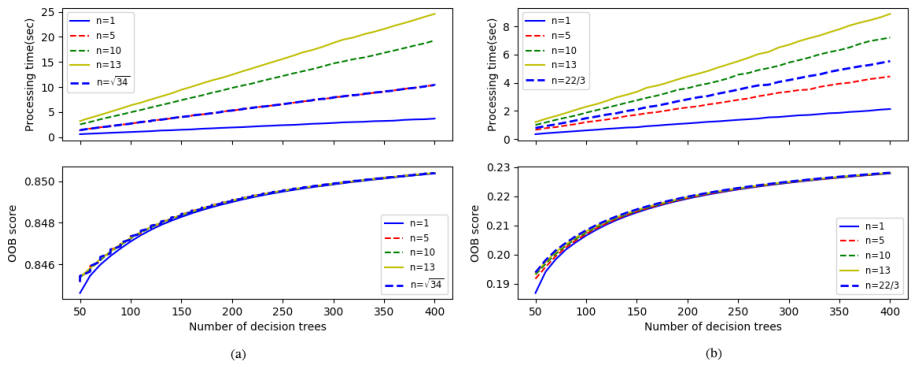

Figure 2.5: Results of the tuning procedure: (**a**) RF classification (rain area), (**b**) RF regression (rainfall), both in February. n = number of input features.

The sample parameter tuning for February is shown as an example in Figure 2.5.

The model performance of rain area and rain estimate assignment increased significantly in the beginning until the number of decision trees reached 250. Beyond this, the increase slowed down. This trend was almost the same for each month of the time period. The OOB score values were almost the same when more features were considered at the nodes and the number of trees increased. As a compromise between prediction accuracy and processing time, a cut-off was made at a number of trees of 250 and n was set to default in both final RF models for the rainfall area delineation $\left(\sqrt{Number of features}\right)$ and rainfall rate assignment (Number of features /3).

2.3.2 Accuracy of Rain Area and Rainfall Retrieval

The validations of the RF models for rainfall area delineation and rainfall rate assignment were conducted independently. In each step, the results of the model were compared pixelwise with the microwave-based IMERG. Furthermore, the results were compared to IR-only IMERG. In order to compare the RF model results with IR-only IMERG, the validation scores for IR-only IMERG were also calculated.

2.3.2.1 Rainfall Area Delineation

The validation scores for rain area delineation were calculated on a pixel basis for each scene. As the ratio of the number of non-rainy pixels to rainy pixels was quite high, we had an unbalanced dataset. An unbalanced dataset in rainfall delineation using RF classification was shown to influence the model accuracy [18, 28]. As suggested by several authors [18, 28], the balanced sampling technique was used to improve model performance. The number of non-rainfall but cloudy pixels that normally define the majority class were randomly downsampled in order to equal the number of majority and minority classes. This technique was applied in two sample weeks from July and August in the training dataset. We defined different scenarios to conduct diverse sensitivity studies. Table 2.3 summarizes the statistics on the verification scores of RF classification with different ratios of majority versus minority class.

Table 2.3: Validation scores for RF classification with different ratio of classes.

Model Name	Cloudy (Majority Class)/ Rainy (Minority Class) Pixels	POD		FAR		HSS	
		July	October	July	October	July	October
Scenario-0	1:1	0.84	0.85	0.80	0.75	0.22	0.30
Scenario-1	2:1	0.82	0.79	0.74	0.68	0.32	0.37
Scenario-2	3:1	0.73	0.74	0.69	0.64	0.36	0.40
Scenario-3	4:1	0.71	0.68	0.68	0.61	0.37	0.42

he HSS and FAR showed better model performance in both months in Scenario-3. Therefore, we implemented the Scenario-3 relation between cloudy and rainy pixels for the whole study period for rainfall area delineation. The verification scores for rain area delineation are presented in Figure 2.6. Given that the evaluation was done on the number of microwave-based IMERG scenes, results are summarized as box-and-whiskers plots and are shown for both the newly developed RF model and the to-date implemented IR-only IMERG procedure.

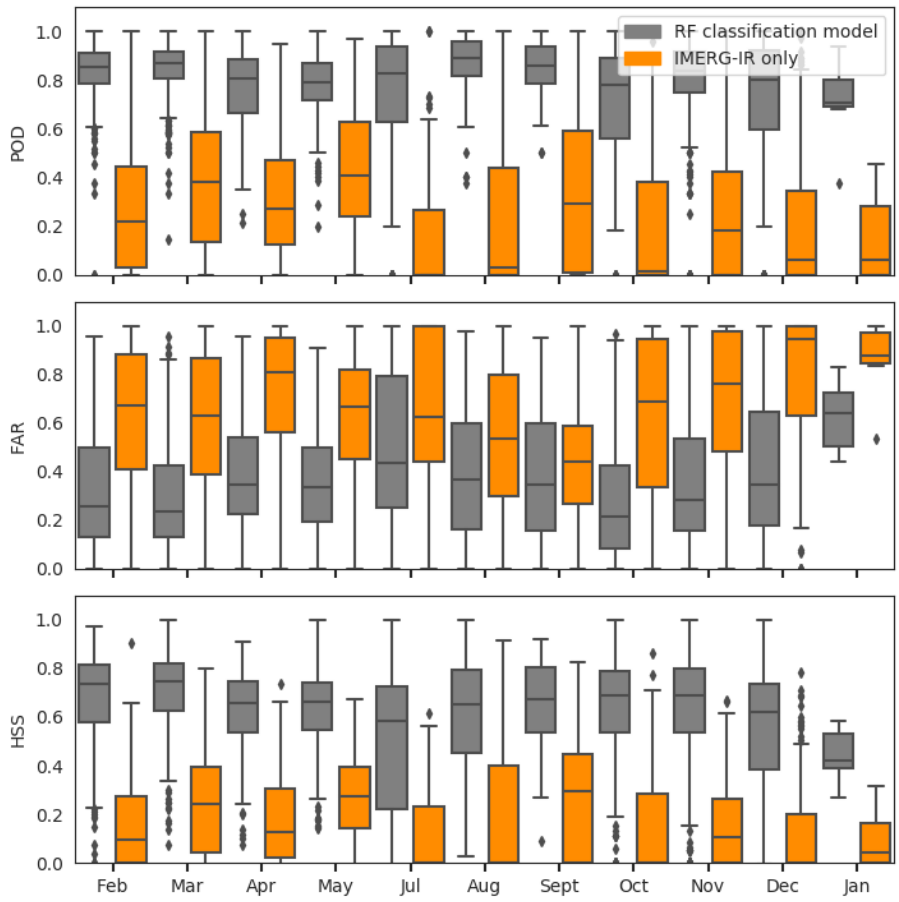

Figure 2.6: Standard verification scores for RF classification model (rain area). The scores are calculated on a scene-by-scene basis. Boxes show 25th, 50th, and 75th percentiles. Whiskers extend to the most extreme data point between 75th-25th percentile. Outliers are shown as points.

Figure 2.7 shows an example of the spatial distribution of the RF prediction of the rain area, showing the rain area detected by RF classification (Figure 2.7b) in comparison to the microwave-based IMERG (Figure 2.7a). The RF classification

showed a good agreement with the observed rain areas.

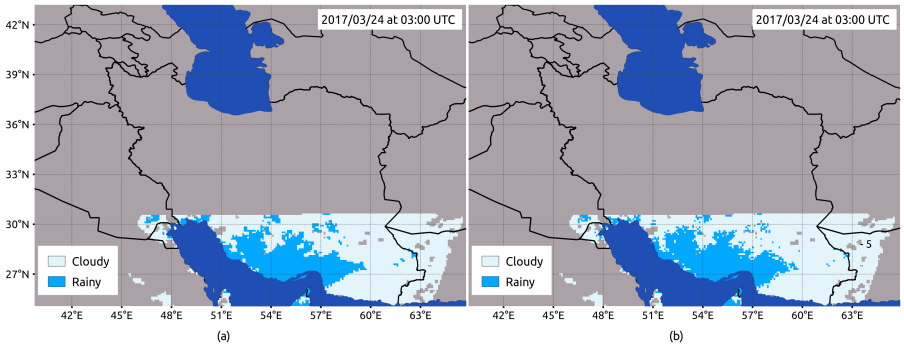

Figure 2.7: Sample satellite scene from 24th March 2017 03:00 UTC. The rainfall area from (**a**) microwave-based IMERG as well as corresponding (**b**) RF classification results. The pixels are selected only where the IMERG microwave was available.

2.3.2.2 Rainfall Rate Assessment

The evaluation metrics for rainfall rate assessment are shown in Figure 2.8. The comparison of the RF regression rainfall assessment and microwave-based IMERG, as well as IR-only IMERG retrievals, was conducted for 1595 scenes of precipitation events in the study period. The number of pixel pairs available for the time period was 287,750.

Figure 2.8 also reveals the occasional high RMSE and MAE between the RF regression and microwave-based IMERG retrievals in almost all months, which are shown as outliers.

As an example Figure 2.9 shows the microwave-based IMERG (Figure 2.9a) and the newly developed rain rate retrieval (Figure 2.9b) for 24 March 2017 at night.

2.3.2.3 Overall Performance of the Merged Rainfall Retrieval Model (Rain Area and Rate)

To assess the overall performance of the rainfall retrieval developed in this study, the RF classification and RF regression was combined and the finally merged product (rain area and rate) was evaluated (Figure 2.10). Thus, all errors from both RF models were accumulated in the final spatio-temporal rainfall estimate. The validation of the model was conducted only for areas that were classified as rainy in the microwave-based IMERG product.

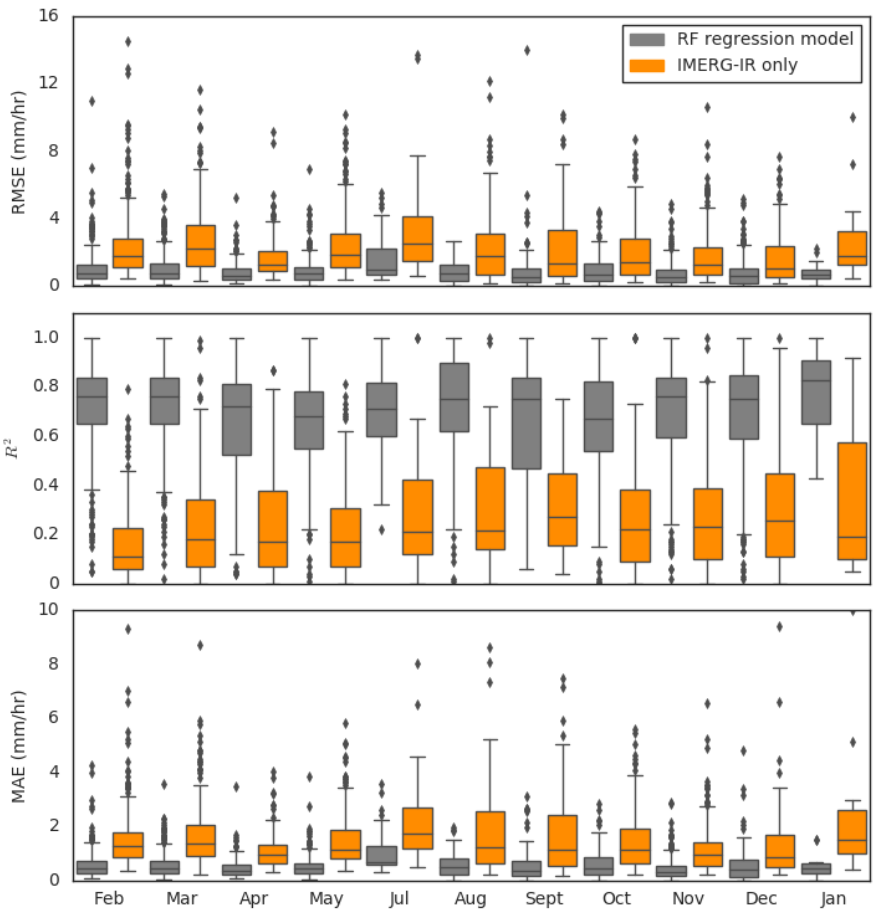

Figure 2.8: Standard validation scores for RF regression model (rain rate). The scores are calculated on a scene-by-scene basis. Boxes show 25th, 50th, and 75th percentiles. Whiskers extend to the most extreme data point between 75th-25th percentile. Outliers are shown as points.

The outliers of RMSE and MAE increased compared to the rain estimate validation in section 2.3.2.2. The high RMSE and MAE could be related to the number of pixels in the calibration dataset, especially for April, September, May, July, October, December, and January. This relationship is shown in Figure 2.11. The higher RMSE and MAE values were normally shown for scenes in months with fewer rainy pixels in the calibration dataset. However, other factors (e.g., the complexity of the rainfall rate, influenced by parameters like elevation diversity in the scene) may have led to uncertainties in the RF model.

Figure 2.12 gives an overview of the model performance along with the altitude during different time periods of the study period. The study period was divided into

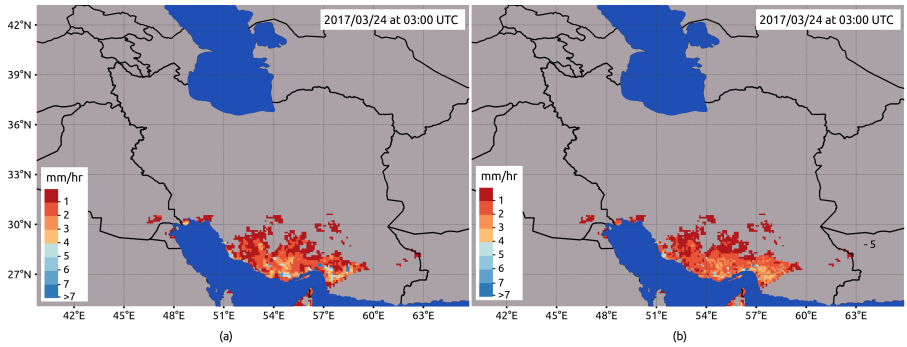

Figure 2.9: Sample satellite scene from 24th March 2017 03:00 UTC. The rainfall estimate for this scene from microwave-based IMERG (**a**) as well as corresponding RF classification (**b**) results. The pixels are selected only where the IMERG microwave was available.

two rainy seasons (i.e., March, April, May (MAM) and October, November, December (OND)) and one dry season (i.e., July, August, September (JAS)). Terrain elevations around 200–500 m showed relatively high maximum RMSE and MAE values for all time periods. These heights can mostly be found in the Lut Desert and along the coast of the Caspian Sea (Figure 2.12a).

Figure 2.13c-d indicates the spatial distribution of the MAE and RMSE, and Figure 2.13e-f, shows the spatial distribution of the MAE and RMSE relative to the average rainfall rate for the whole study period (February 2017 to February 2018) in the study region.

The average RMSE and MAE (Figure 2.13c-d) showed relatively higher values in the Zagros mountainous region (0.5–6 mm/h for MAE and 0.4–16 mm/h) and Alborz mountainous range (0.5–8 mm/h for MAE and 0.5–12 mm/h). Meanwhile, in Figure 2.13c,d the relative RMSE and MAE in the mountainous region show some uncertainties in the area between 50E, 32N and 51E, 33N with the value of 18.67 and in the connection zone between Zagros and Alborz in the north-west of the country with values between 0.5 and 25. The RMSE, MAE, and rainfall rate near the coast of Caspian Sea, at the northern slopes of Alborz mountains (Figure 2.13-c,d) indicated higher errors (20 mm/h). In the Kavir Desert in the center of the country, the RMSE and MAE of the RF model were estimated as 0.1–16 mm/h.

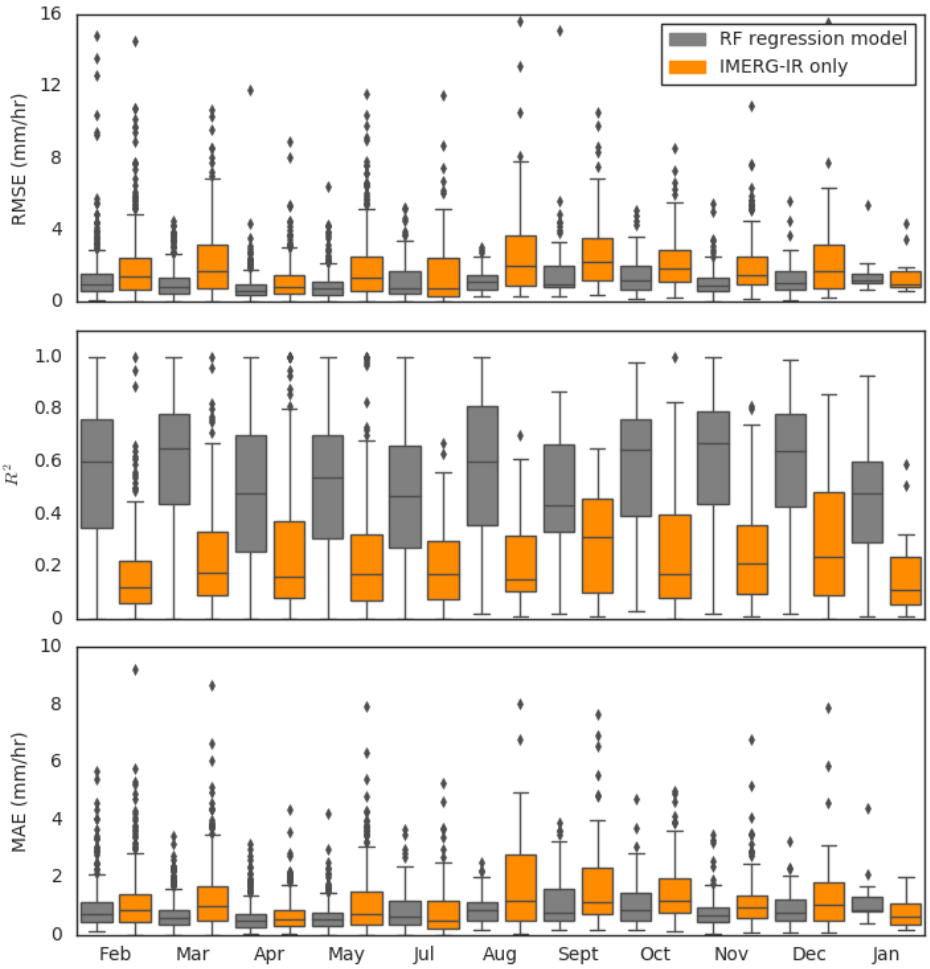

Figure 2.10: Standard validation scores for RF regression model (rain rate). The scores are calculated on a scene-by-scene basis. Boxes show 25th, 50th, and 75th percentiles. Whiskers extend to the most extreme data point between 75th-25th percentile. Outliers are shown as points.

2.3.2.4 Comparison to Gauge Stations

To validate the RF model performance against a completely independent dataset, we used gauge stations from Iran (Figure 2.1) as a reference. In this step, we applied the model to the original spatial and temporal resolution of MSG-1 (3 km^2, 15 minutes) for the whole study period, and the results were compared to the available rain gauges. The 15-min rainfall rates were added up to 6 h and 24 h, respectively. For comparison, the pixel values of the corresponding station coordinates were extracted.

The overall performances of the model against gauge are shown in Figure 2.14 and 2.15. During our research period, the available gauge stations for our study

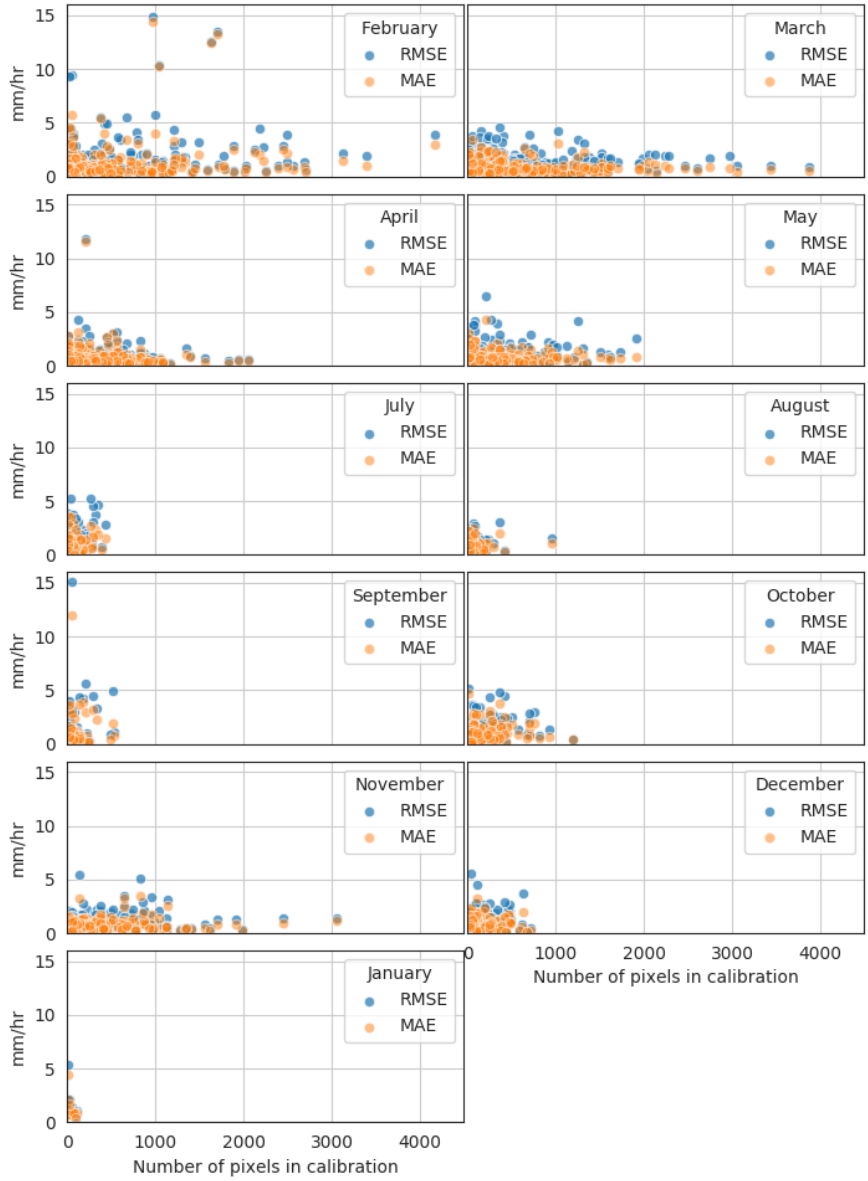

Figure 2.11: RMSE and MAE values as a function of the number of pixels in the training dataset for different months.

were 45 synoptic stations in the temporal resolution of 6 h and 32 stations with daily resolution. Our results indicate the expected seasonal behavior for rain area validation scores. During the dry summer (JAS), the RF model performed worst with a POD less than 0.2, FAR more than 0.6, and poor performance, as indicated by the low HSS. In the rest of the year, the average HSS was 0.3–0.55 and 0.25–0.55 per 6-h and per day, respectively. The best POD ranged between 30% to 70% in winter, autumn, and

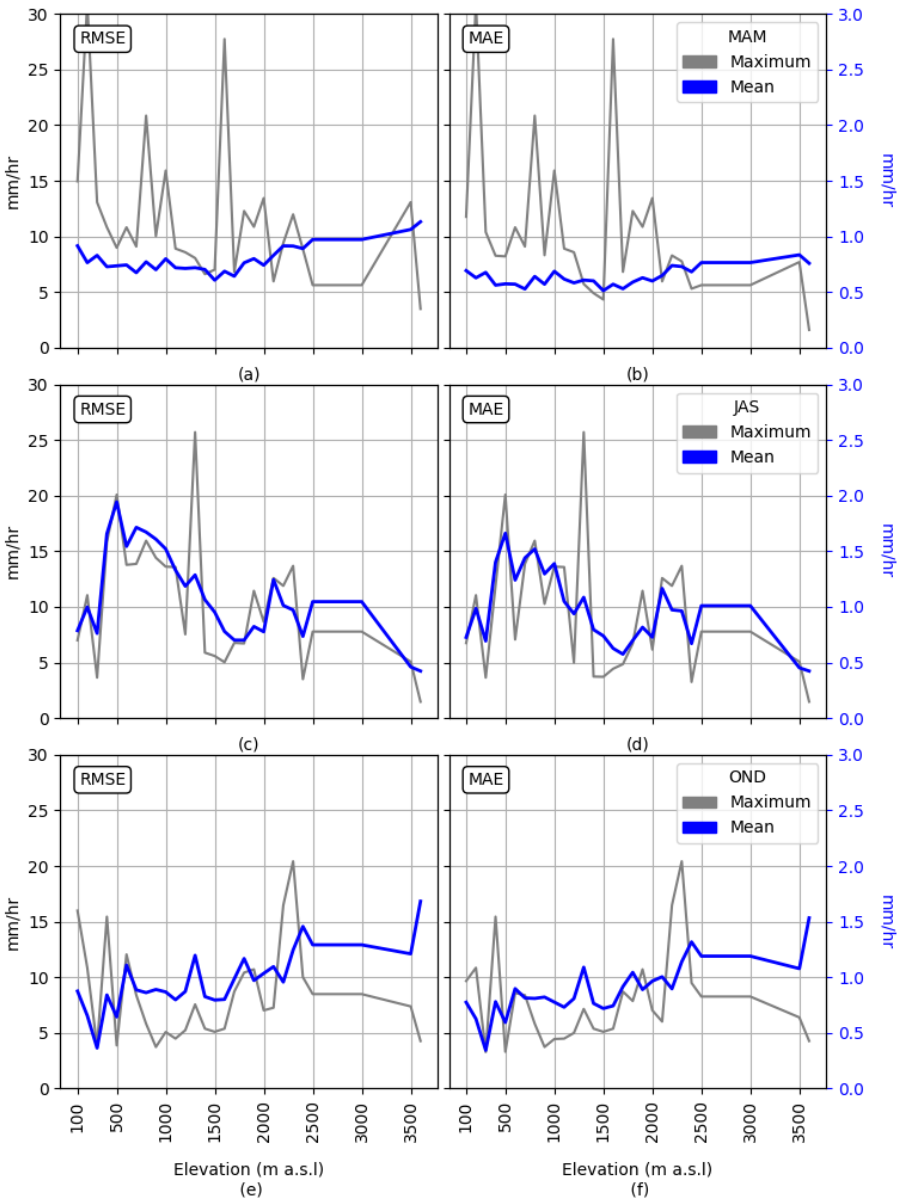

Figure 2.12: Maximum and mean RMSE and MAE values for different elevation levels for different time periods MAM: March-April-May; JAS: July-August-September; OND: October-November-December.(**a**) indicates the mean RMSE for MAM, (**b**) shows average MAE for MAM, (**c**) shows mean RMSE for JAS, (**d**) indicates mean MAE for JAS, (**e**)shows mean RMSE for OND and (**f**) indicates mean MAE for OND.

spring. The average daily RMSE was around 16 mm and the average daily MAE was around 10 mm depending on the month. The overall range of R was between 0.17 and 0.8 for all months except JAS.

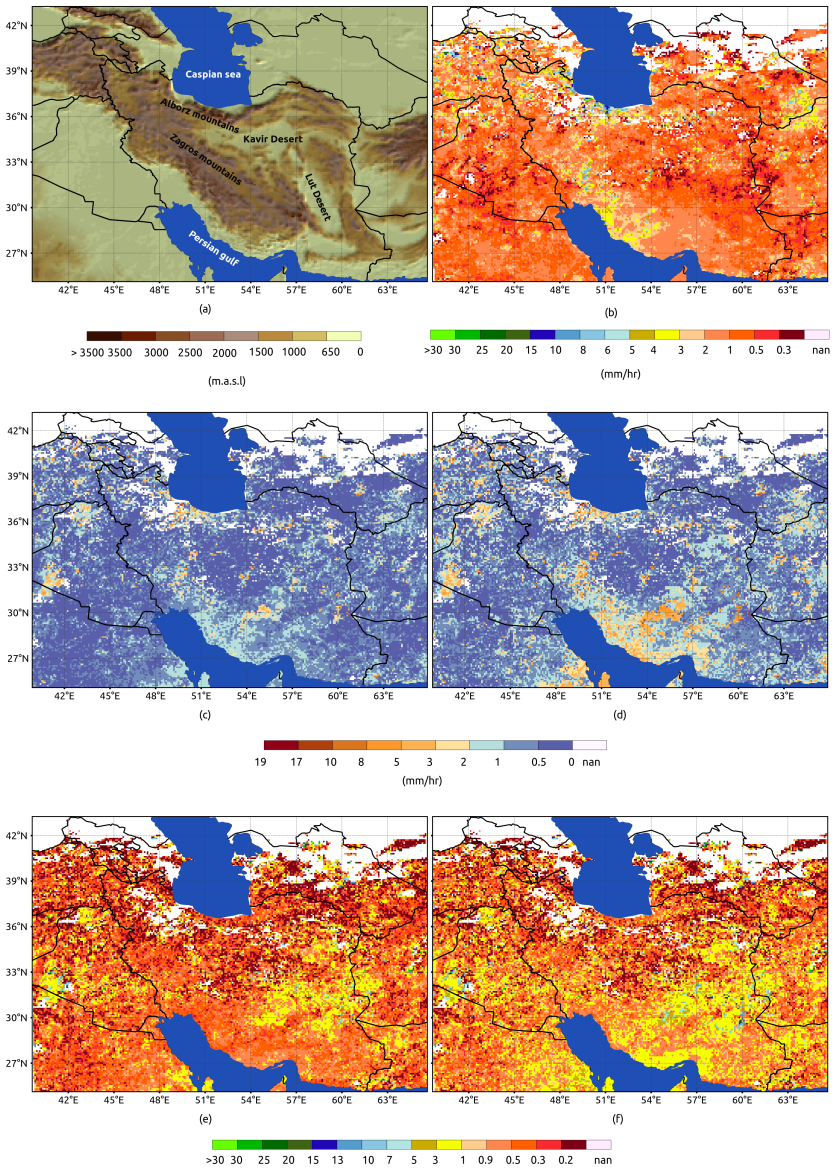

Figure 2.13: Spatial distribution of (**a**) elevation, (**b**) average rainfall rate, (**c**) average MAE, (**d**) average RMSE, (**e**) average MAE to average rainfall rate (MAE rate), and (**f**) average RMSE to average rainfall rate (RMSE rate).

2.4 Discussion

2.4.1 Performance of Rain Area and Rainfall Retrieval Model

Feature elimination and parameter tuning procedures were carried out to determine the final input feature set. The results of the feature selection in RF regression (rain rate) indicate that the models identified the close link between topography and

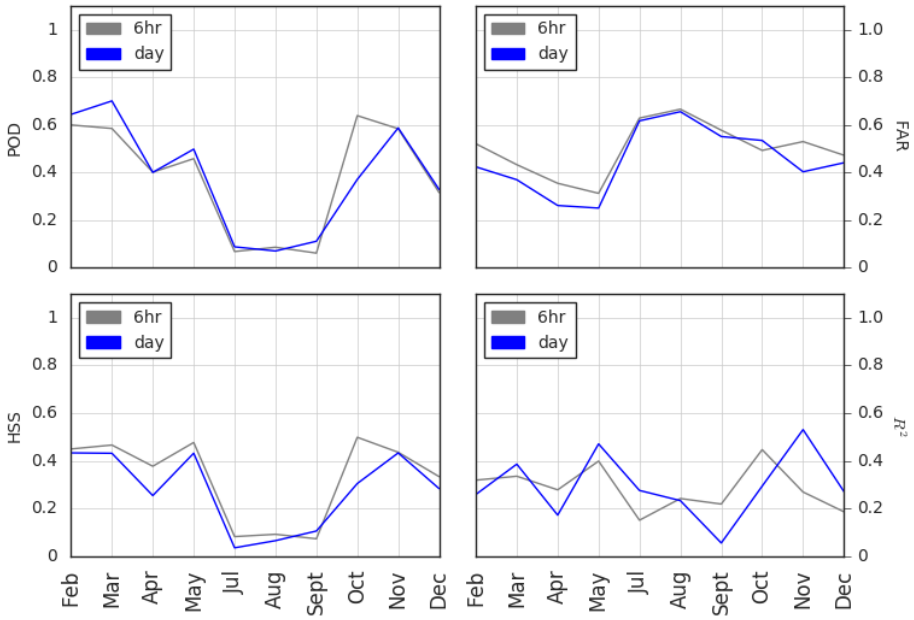

Figure 2.14: Standard validation scores for the RF classification model (rain area delineation) against gauge stations. The scores are based on the data pairs of 6 h/daily for the time period from February 2017 until the end of 2017. The scores were calculated based on all available pairs for the time period for POD, FAR, and HSS. The gray boxes indicate the results for stations with 6-h resolution and the blue boxes for stations with daily resolution. Boxes show 25th, 50th, and 75th percentiles. Whiskers extend to the most extreme data point between 75th and 25th percentile. Outliers are shown as points.

rainfall. Consequently, the feature importance of these five features was relatively high compared to the other features. This is not surprising, as the elevation plays an important role in rainfall amount. Additionally, in rainfall delineation, at least one of these features were selected. In general, the models tended to prioritize band combinations and texture features over the use of single bands. The feature selection of each month for both models shows that the models preferred to use two bands in combination where the dominant texture metric selected in almost all months was the pseudo cross-variogram. This behavior was also shown by [39] in fog retrieval using RF.

The validation of the rainfall retrieval against independent microwave-based IMERG showed promising results, but also highlighted the difficulty of rainfall retrievals at high altitudes and near coastlines.

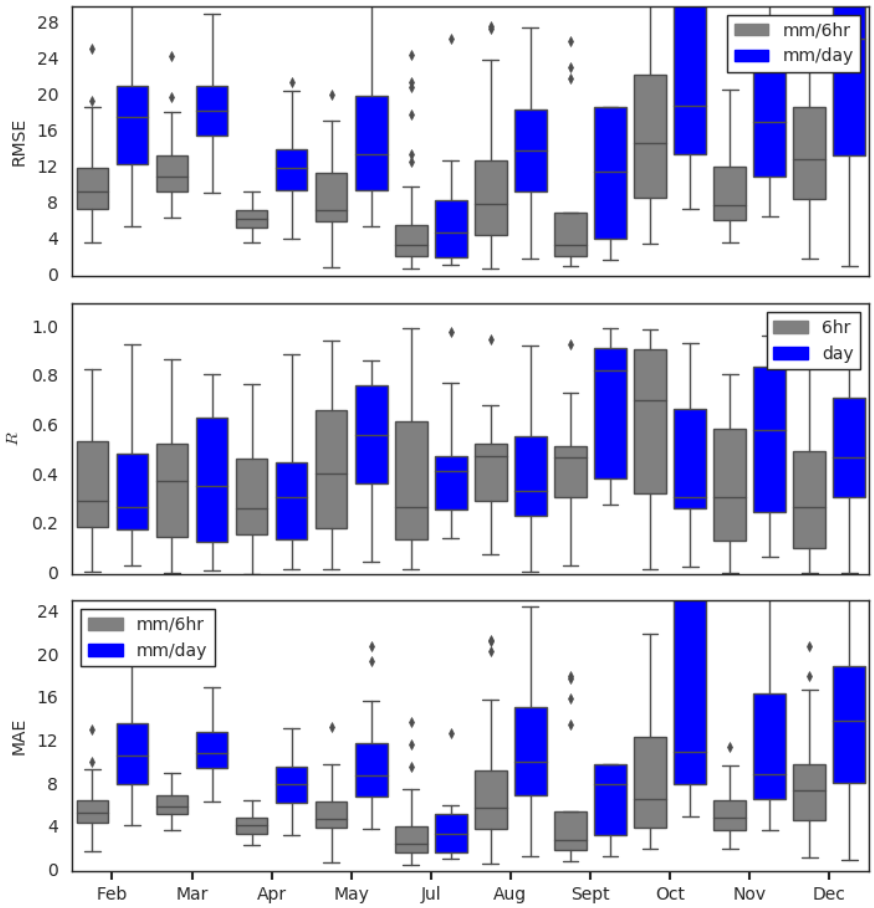

Figure 2.15: Standard validation scores for RF regression model (rain rate) against gauge stations. The scores are based on the data pairs of 6 h/daily for the time period from February 2017 to the end of 2017. The scores were calculated from the pairs in which rainy events from the RF model or gauge were available. The absolute value of R is shown here. The gray boxes indicate the results for stations with 6-h resolution, and the blue boxes for stations with daily resolution. Boxes show 25th, 50th, and 75th percentiles. Whiskers extend to the most extreme data point between 75th and 25th percentile. Outliers are shown as points.

In the rainfall area delineation step, as a general pattern, Figure 2.6 reveals that the predictions of the developed RF classification model clearly outperformed the IR-only IMERG product. Overall, the central tendency of the verification scores for each month were very good for the RF model. However, the extent of the whiskers were rather wide in HSS, indicating that the performance of the model varied. The FAR was relatively high in all months, but was still better than IR-only IMERG. As

indicated by the FAR, there was a general tendency to overestimate the rain area. Additionally, the indices exhibited a seasonal dependency, with more false alarms and lower HSS during summer months (July, August, September). The fact that predictions for summer months were generally slightly worse might be due to the warm air beneath the clouds that might lead to more evaporation of the precipitation during summer (i.e., the same rain from clouds could reach the ground in winter, but not in the summer).

The verification scores for rain area delineation were superior to those in previous studies by Kühnlein et al. [17] and Meyer, Drönner, and Nauss [19] and Min et al. [28], which might be due to the feature selection process that was done in our study but not in the mentioned studies.

In the next step, the RF regression model (Figure 2.8) was capable of predicting rainfall rates accurately, and better than the IR-only IMERG. The performance quality of the RF regression followed a seasonal trend where the RMSE and MAE were slightly higher in July and August—the drier months, with lower rainfall amounts and lower rain areas. Visually (Figure 2.9), there was a good coincidence of rain rates, but the new RF model seemed to exhibit a tendency to underestimate the higher rain rates (3–5 mm/h).

As has been seen so far, RF was able to model the rainfall when each step of the rainfall retrieval was evaluated separately. The performance of the model when both steps of the rainfall retrieval were combined was also investigated. The results are presented in Figure 2.10 as box-and-whisker plots. In comparison to the results in 2.3.2.2, the general performance of the newly developed model was reduced, as expected. The RMSE and MAE showed a less-consistent relationship, and the correlation coefficient between the merged RF model and the microwave-based IMERG was lower than for training. The range of R illustrates more variability in the boxplot. However, compared to the IR-only IMERG validation, R values indicated that the RF model developed in this study still performed significantly better compared to IR only.

On the other hand, the maximum values of MAE show the overestimation of the new RF model. The overestimation of the model in Iran, with its high amount of arid and semi-arid regions, might be attributed to environmental barriers. In this climate, due to the heat under the clouds, raindrops may evaporate before reaching the surface, which leads to an overestimation of the retrieval—particularly in the dry seasons [33].

The advantage of the feature selection was also indicated by the correlation coefficient for the modeled rainfall quantities. The results show an improvement of the infrared-based rainfall retrieval compared to Meyer, Drönner, and Nauss [19]. The correlation coefficient in our study varied between 0.23 and 0.8, while in the study by Meyer, Drönner, and Nauss [19] he average correlation coefficient was around 0.33. However, our model showed slightly higher RMSE values (mm/h) compared to those in the works of Meyer, Drönner, and Nauss [19] and Min et al. [28].

It is important to note that aside from the environmental barrier and land characteristics of the case study, the number of training data sets in RF was seen to influence the model performance—especially for April, September, May, July, October, December, and January. This relationship is shown in Figure 2.11. The lower number of pixels may have led to weak learning of the RF model, especially when the data was complex. This is because RF is a bootstrap model [29], which means that the random samples are chosen from the training dataset, and the performance of the model is highly dependent on the properties and distribution of this dataset. When the sample size is low, the set of possible random selections may not represent the proper distribution of the rainfall, causing the model to perform poorly [57].

The validation of the model in different altitudes and different seasons (Figure 2.12), highlighted the limitation of the RF model in different terrain elevations. One of the challenges of the model was in the elevation range of 200–500 m. These heights are located in Lut and Kavir Deserts and along the coast of Caspian Sea. The lower performance in these areas might be due to decreasing evaporation of raindrops below the cloud in the desert and increasing rainfall rates due to higher humidity near the Caspian Sea.

Additionally, mean RMSE and MAE values increased with increasing elevation during MAM (Figure 2.12a,b) and OND (Figure 2.12e,f). During JAS (Figure 2.12c,d) tthe mean MAE and RMSE values decreased with increasing elevation. During the rainy season (OND and MAM), the relatively poor performance of the RF model for elevations above 1500 m a.s.l. might be attributed to uncertainties in the microwave-only rainfall information of IMERG over snow-covered areas in mountainous terrain [12]. Furthermore, higher RMSE and MAE values might be due to uncertainties in the retrieval of solid precipitation. Additionally, the spatial map of average RMSE and MAE (Figure 2.13c,d) shows that these uncertainties were along the Zagros mountains in the west and the Alborz mountain range in the north of Iran. The RF model performed best for mid-altitudes between 500 and 1500 m a.s.l. Near

the coast of Caspian Sea, at the northern slopes of the Alborz mountains the RMSE and MAE (Figure 2.13-c,d) values indicated higher errors. This might be due to the high rainfall rates (10–30 mm/h) and uncertainties in connection with orographically induced rainfall effects. The MAE and RMSE rates did not show these characteristics. This means the rainfall rates in these places are quite high, and this affected the RMSE and MAE, which was expected (Figure 2.13e,f). However, both parameters indicated uncertainties for the transition zone between the Zagros mountain range and the Lut Desert. These uncertainties might be due to differing climatic influences in both regions. There were spots of high inaccuracy (Figure 2.13e,f) in the area between 54E, 28N and 62E, 33N with average rainfall rates of 0.2–0.5 mm/h. This might be due to the evaporation of the raindrops below the cloud in semi-arid regions, which especially leads to overestimation for low rainfall rates.

One of the greatest drawbacks of using microwave-only IMERG was the timing of the overflight of the microwave satellite in the study region. It is likely that some rainfall events were not recorded due to unfavorable timing of its overflight over Iran, and this introduced uncertainty in the training of our model.

2.4.2 Comparison to Gauge Stations

The overall performance of the model is promising (Figure 2.14 and 2.15), and the results show the seasonal behavior for all rainfall area validation scores. The low number of rainfall events and relatively low amounts of rainfall might be the reason for the poor performance during the summer season. Moreover, the comparison of point data with satellite data might be more vulnerable to uncertainties during summer when highly convective rain clouds predominate. During such events, the spatial displacement due to parallax shifting [19] for MSG1 pixel coordinates relative to the gauge station coordinates might be more relevant. Additionally, wind drift and rainfall evaporation below clouds could cause higher discrepancies between RF model output and station measurements. Note also that despite possible RF model uncertainties, rainfall measurement errors at the ground might also be a topic for discussion. Interestingly, the RF model output showed almost the same performance regardless of the temporal resolution, which is in contrast to the results of [18, 19]. This is due to the fact that six hourly stations and daily stations are independent from each other.

Our technique had a clear advantage in rain area detection compared to global datasets which were evaluated in Iran. Katiraie-Boroujerdy et al. [33] examined the

performance of CMORPH, PERSIAN, and TRMM 3B42 with a spatial resolution of 29 km. The highest POD of 0.4 and the lowest FAR of 0.2 were achieved on a seasonal scale (spring and winter). Our model showed PODs of 0.2–0.7 for spring and winter and lower FAR between 0.1 and 0.6 for spring and winter on a daily and six-hourly scale with a spatial resolution of 3 km. The spatial and temporal resolution affected the performance of the model.

The evaluation results of TRMM 3B42 (POD 0.39–0.5 and FAR 0.55–0.71 at a daily scale and spatial resolution of 29 km) in Iran in another study by Sharifi, Steinacker, and Saghafian [34] demonstrate the advantage of our model in the case of rain area detection in Iran. In the same study, the IMERG V05 (spatial resolution of 11 km and temporal resolution of 30 min) showed relatively better POD compared to TRMM 3B42 with the value of 0.46–0.77 and FAR of 0.43–0.59 at daily resolution, which still shows the better performance of our model. In the same study, the evaluation of rain estimate for IMERG and TRMM showed RMSEs of around 7.10 mm and 7.72 mm in a day respectively. The estimated correlation coefficients were 0.46–0.52 for IMERG and 0.27–0.42 for TRMM. These results indicate that our model performed less accurately than IMERG, but the values of the correlation coefficient and MAE confirmed that our rain estimations were superior to TRMM.

Please note that this comparison needs to be interpreted with caution. Although these comparisons were conducted in the same country, the gauges were not the same. Additionally, Katiraie-Boroujerdy et al. [33] set a minimum number of gauges in each grid pixel to represent the ground-truth rainfall, while we used only one gauge per pixel. The assessment of satellite rainfall products with a low number of gauges in each grid pixel led to an underestimation of the quality of satellite products, since point-scale observations of scarce gauges cannot be a representative of the spatial distribution of rain [58].

2.5 Conclusions

In the present study, a new rainfall retrieval technique using microwave satellite and MSG1 data was developed for Iran as a case study. The method uses geostationary multispectral satellite data to train RF models. Microwave-only GPM IMERG rainfall information was considered as a reference for model training. In a first step, the rainfall area was delineated, followed by rainfall rate assignment. The method was validated against independent microwave-only GPM IMERG rainfall data not used

for model training. Additionally, the new technique was validated against completely independent gauge station data. The validation results indicate that the new technique was capable of retrieving rainfall correctly. This offers the potential for high spatio-temporal (3 km, 15 min) rainfall resolution in near-real-time for Iran, which is important for water resources disciplines and hydrological modeling, as examples. Concerning the importance of the respective predictor variables, elevation and related indices were shown to be important for rainfall area delineation and rainfall rate assignment. However, there were challenging regions with higher uncertainties, such as the coastlines of the Caspian Sea and the Lut Desert. In both regions, the relative humidity seemed to play a critical role. The IR-based technique is based on the indirect relationship between cloud top temperature and rainfall rate. Therefore, it is limited to the characteristics of the top of the cloud. Higher relative humidity near the Caspian Sea may lead to absorption of the humidity of the rainfall drops under the clouds before reaching the ground, and lead to consequent underestimation of rainfall using satellite-based rainfall products. The lower relative humidity in the Lut Desert could cause the evaporation of rain drops below clouds before reaching the ground. As a consequence, satellite-based rainfall retrieval overestimated the rainfall rate at the ground. Therefore, relative humidity could be included as an additional predictor variable for the RF models. The study of [28] showed that the incorporation of atmospheric information from numerical weather models could improve satellite-based rainfall retrievals. In a next step, potential improvements by including relative humidity data as a predictor should be investigated. In addition, the influence of the complex climatic and topographic situation in Iran together with the seasonally differing atmospheric dynamics on the performance of the new rainfall retrieval technique should be investigated in more detail.

In cases where there is not enough data available for feature selection, model tuning and model training (June in our case), RF models from a similar month (e.g., July in our case) or some kind of climatological model could be applied.

The main advantage of the proposed method is its applicability at a global scale. Since it relies only on microwave rainfall information from IMERG for RF model training, it could be applied theoretically on a global scale without the need for ground-based rainfall information. Previous studies mostly trained the RF models with ground-based rainfall measurements, which restricts the usage to the respective regions. For regions without sufficient ground-based rainfall measurements, these methods are not applicable. Our method could be applied to different regions with

different climatology and altitude. This approach has the potential to be applied in nearby semi-arid regions with comparable climatic patterns, such as Iraq or Kuwait. However, we recommend that the influence of the orography and the distance to the sea be verified before application. For other regions with different climatic and orographic patterns and other geostationary satellite data, the processes of feature selection and the tuning of the RF models should be re-implemented in order to adapt the models to the specific circumstances.

Concerning the sufficient accuracy of the obtained results for water resources disciplines and hydrological modeling the comparisons with validation results of other satellite-based retrieval techniques in the discussion (section 2.4 show a good performance of our technique. This is especially true considering the high spatio-temporal resolution of our data. However, the performance of hydrological modeling with the usage of satellite-based rainfall data generally has been shown to depend not just on the rainfall data but also on other factors as hydrological model formulation, topography, precipitation type and seasonality [59]. In order to apply our technique for hydrological modeling in Iran we would have to perform a bias correction of the satellite-based rainfall data with rain gauges, if available in the catchment and to recalibrate the hydrological model based on the satellite-based rainfall data as suggested by Maggioni and Massari [59].

2.A Appendix A

1-IR 3.9	33-ΔT 9.7-13.4	65-CV 3.9-10.8	97-PCV 6.2-8.7
2-WV 6.2	34-ΔT 10.8-12.0	66-CV 3.9-12.0	98-PCV 6.2-9.7
3-WV 7.3	35-ΔT 10.8-13.4	67-CV 3.9-13.4	99-PCV 6.2-10.8
4-IR 8.7	36-ΔT 12.0-13.4	68-CV 6.2-7.3	100-PCV 6.2-12.0
5-IR 9.7	37-VAR(3.9)	69-CV 6.2-8.7	101-PCV 6.2-13.4
6-IR 10.8	38-VAR(6.2)	70-CV 6.2-9.7	102-PCV 7.3-8.7
7-IR 12.0	39-VAR(7.3)	71-CV 6.2-10.8	103-PCV 7.3-9.7
8-IR 13.4	40-VAR(8.7)	72-CV 6.2-12.0	104-PCV 7.3-10.8
9-ΔT 3.9-6.2	41-VAR(9.7)	73-CV 6.2-13.4	105-PCV 7.3-12.0
10-ΔT 3.9-7.3	42-VAR(10.8)	74-CV 7.3-8.7	106-PCV 7.3-13.4
11-ΔT 3.9-8.7	43-VAR(12.0)	75-CV 7.3-9.7	107-PCV 8.7-9.7
12-ΔT 3.9-9.7	44-VAR(13.4)	76-CV 7.3-10.8	108-PCV 8.7-10.8
13-ΔT 3.9-10.8	45-MAD(3.9)	77-CV 7.3-12.0	109-PCV 8.7-12.0
14-ΔT 3.9-12.0	46-MAD(6.2)	78-CV 7.3-13.4	110-PCV 8.7-13.4
15-ΔT 3.9-13.4	47-MAD(7.3)	79-CV 8.7-9.7	111-PCV 9.7-10.8
16-ΔT 6.2-7.3	48-MAD(8.7)	80-CV 8.7-10.8	112-PCV 9.7-12.0
17-ΔT 6.2-8.7	49-MAD(9.7)	81-CV 8.7-12.0	113-PCV 9.7-13.4
18-ΔT 6.2-9.7	50-MAD(10.8)	82-CV 8.7-13.4	114-PCV 10.8-12.0
19-ΔT 6.2-10.8	51-MAD(12.0)	83-CV 9.7-10.8	115-PCV 10.8-13.4
20-ΔT 6.2-12.0	52-MAD(13.4)	84-CV 9.7-12.0	116-PCV 12.0-13.4
21-ΔT 6.2-13.4	53-ROD(3.9)	85-CV 9.7-13.4	117-ELV
22-ΔT 7.3-8.7	54-ROD(6.2)	86-CV 10.8-12.0	118-TPI
23-ΔT 7.3-9.7	55-ROD(7.3)	87-CV 10.8-13.4	119-TRI
24-ΔT 7.3-10.8	56-ROD(8.7)	88-CV 12.0-13.4	120-Slope
25-ΔT 7.3-12	57-ROD(9.7)	89-PCV 3.9-6.2	121-Aspect
26-ΔT 7.3-13.4	58-ROD(10.8)	90-PCV 3.9-7.3	
27-ΔT 8.7-9.7	59-ROD(12.0)	91-PCV 3.9-8.7	
28-ΔT 8.7-10.8	60-ROD(13.4)	92-PCV 3.9-9.7	
29-ΔT 8.7-12.0	61-CV 3.9-6.2	93-PCV 3.9-10.8	
30-ΔT 8.7-13.4	62-CV 3.9-7.3	94-PCV 3.9-12.0	
31-ΔT 9.7-10.8	63-CV 3.9-8.7	95-PCV 3.9-13.4	
32-ΔT 9.7-12.0	64-CV 3.9-9.7	96-PCV 6.2-7.3	

References

[1] Mohammed H I Dore. "Climate change and changes in global precipitation patterns: what do we know?" en. In: *Environ. Int.* 31.8 (Oct. 2005), pp. 1167–1181.

[2] M J Amiri and S S Eslamian. *Investigation of Climate Change in Iran.* 2010.

[3] J Lelieveld et al. "Climate change and impacts in the Eastern Mediterranean and the Middle East". en. In: *Clim. Change* 114.3-4 (Mar. 2012), pp. 667–687.

[4] Reza Modarres and Ali Sarhadi. *Rainfall trends analysis of Iran in the last half of the twentieth century.* 2009.

[5] Reza Modarres and Vicente de Paulo Rodrigues da Silva. *Rainfall trends in arid and semi-arid regions of Iran.* 2007.

[6] Tayeb Raziei et al. *Spatial Patterns and Temporal Variability of Drought in Western Iran.* 2009.

[7] Margaret Wambui Kimani, Joost C B Hoedjes, and Zhongbo Su. "An Assessment of Satellite-Derived Rainfall Products Relative to Ground Observations over East Africa". en. In: *Remote Sensing* 9.5 (May 2017), p. 430.

[8] George J Huffman et al. *The TRMM Multisatellite Precipitation Analysis (TMPA): Quasi-Global, Multiyear, Combined-Sensor Precipitation Estimates at Fine Scales.* 2007.

[9] Robert J Joyce et al. *CMORPH: A Method that Produces Global Precipitation Estimates from Passive Microwave and Infrared Data at High Spatial and Temporal Resolution.* 2004.

[10] Ali Behrangi et al. *PERSIANN-MSA: A Precipitation Estimation Method from Satellite-Based Multispectral Analysis.* 2009.

[11] M R P Sapiano and P A Arkin. *An Intercomparison and Validation of High-Resolution Satellite Precipitation Estimates with 3-Hourly Gauge Data.* 2009.

[12] George J Huffman et al. "NASA global precipitation measurement (GPM) integrated multi-satellite retrievals for GPM (IMERG)". In: *Algorithm theoretical basis document, version* 4 (2015), p. 30.

[13] Willam S Olson, Hirohiko Masunaga, and Combined Radar-Radiometer Algorithm Team Gpm. "GPM combined radar-radiometer precipitation algorithm theoretical basis document (Version 4)". In: *NASA: Washington, DC, USA* (2016).

[14] C Kidd and V Levizzani. *Status of satellite precipitation retrievals*. 2011.

[15] Haralambos Feidas and Apostolos Giannakos. "Classifying convective and stratiform rain using multispectral infrared Meteosat Second Generation satellite data". en. In: *Theor. Appl. Climatol.* 108.3-4 (May 2012), pp. 613–630.

[16] Apostolos Giannakos and Haralambos Feidas. "Classification of convective and stratiform rain based on the spectral and textural features of Meteosat Second Generation infrared data". en. In: *Theor. Appl. Climatol.* 113.3-4 (Aug. 2013), pp. 495–510.

[17] Meike Kühnlein et al. "Precipitation Estimates from MSG SEVIRI Daytime, Nighttime, and Twilight Data with Random Forests". In: *J. Appl. Meteorol. Climatol.* 53.11 (Nov. 2014), pp. 2457–2480.

[18] Meike Kühnlein et al. "Improving the accuracy of rainfall rates from optical satellite sensors with machine learning—A random forests-based approach applied to MSG SEVIRI". In: *Remote Sens. Environ.* 141 (2014), pp. 129–143.

[19] H. Meyer, J. Drönner, and T. Nauss. "Satellite-based high-resolution mapping of rainfall over southern Africa". In: *Atmospheric Measurement Techniques* 10.6 (2017), pp. 2009–2019. DOI: 10.5194/amt-10-2009-2017. URL: https://amt.copernicus.org/articles/10/2009/2017/.

[20] Hanna Meyer et al. "Comparison of four machine learning algorithms for their applicability in satellite-based optical rainfall retrievals". In: *Atmospheric research* 169 (2016), pp. 424–433.

[21] Kou-lin Hsu et al. "Precipitation estimation from remotely sensed information using artificial neural networks". In: *Journal of Applied Meteorology* 36.9 (1997), pp. 1176–1190.

[22] DIF Grimes et al. "A neural network approach to real-time rainfall estimation for Africa using satellite data". In: *Journal of Hydrometeorology* 4.6 (2003), pp. 1119–1133.

[23] Yang Hong et al. "Precipitation estimation from remotely sensed imagery using an artificial neural network cloud classification system". In: *Journal of Applied Meteorology* 43.12 (2004), pp. 1834–1853.

[24] FJ Tapiador et al. "Neural networks in satellite rainfall estimation". In: *Meteorological Applications* 11.1 (2004), pp. 83–91.

[25] D Capacci and BJ Conway. "Delineation of precipitation areas from MODIS visible and infrared imagery with artificial neural networks". In: *Meteorological Applications* 12.4 (2005), pp. 291–305.

[26] G Rivolta et al. "Artificial neural-network technique for precipitation nowcasting from satellite imagery". In: *Advances in Geosciences* 7 (2006), pp. 97–103.

[27] Tanvir Islam et al. "Non-parametric rain/no rain screening method for satellite-borne passive microwave radiometers at 19–85 GHz channels with the Random Forests algorithm". In: *International journal of remote sensing* 35.9 (2014), pp. 3254–3267.

[28] M Min et al. "Estimating Summertime Precipitation from Himawari-8 and Global Forecast System Based on Machine Learning". In: *IEEE Trans. Geosci. Remote Sens.* 57.5 (May 2019), pp. 2557–2570.

[29] Leo Breiman. "Random Forests". In: *Mach. Learn.* 45.1 (Oct. 2001), pp. 5–32.

[30] Vladimir Svetnik et al. "Random forest: a classification and regression tool for compound classification and QSAR modeling". In: *Journal of chemical information and computer sciences* 43.6 (2003), pp. 1947–1958.

[31] S Javanmard et al. *Comparing high-resolution gridded precipitation data with satellite rainfall estimates of TRMM_3B42 over Iran.* 2010.

[32] Saber Moazami et al. "Comparison of PERSIANN and V7 TRMM Multi-satellite Precipitation Analysis (TMPA) products with rain gauge data over Iran". In: *Int. J. Remote Sens.* 34.22 (Nov. 2013), pp. 8156–8171.

[33] Pari-Sima Katiraie-Boroujerdy et al. "Evaluation of satellite-based precipitation estimation over Iran". In: *J. Arid Environ.* 97 (Oct. 2013), pp. 205–219.

[34] Ehsan Sharifi, Reinhold Steinacker, and Bahram Saghafian. *Assessment of GPM-IMERG and Other Precipitation Products against Gauge Data under Different Topographic and Climatic Conditions in Iran: Preliminary Results.* 2016.

[35] Boris Thies, Thomas Nauß, and Jörg Bendix. "Precipitation process and rainfall intensity differentiation using Meteosat Second Generation Spinning Enhanced Visible and Infrared Imager data". In: *J. Geophys. Res.* 113.D23 (Dec. 2008), p. 1121.

[36] Johannes Drönner et al. "FFLSD - Fast Fog and Low Stratus Detection tool for large satellite time-series". In: *Comput. Geosci.* 128 (July 2019), pp. 51–59.

[37] S Finkensieper et al. *CLAAS-2: CM SAF CLoud property dAtAset using SEVIRI–Edition 2, Satellite Application Facility on Climate Monitoring.* 2016.

[38] Jan Cermak and Jörg Bendix. "A novel approach to fog/low stratus detection using Meteosat 8 data". In: *Atmos. Res.* 87.3 (Mar. 2008), pp. 279–292.

[39] Sebastian Egli, Boris Thies, and Jörg Bendix. "A Hybrid Approach for Fog Retrieval Based on a Combination of Satellite and Ground Truth Data". en. In: *Remote Sensing* 10.4 (Apr. 2018), p. 628.

[40] S Egli et al. "A 10 year fog and low stratus climatology for Europe based on Meteosat Second Generation data". In: *Q.J.R. Meteorol. Soc.* 143.702 (Jan. 2017), pp. 530–541.

[41] Hans Martin Schulz et al. "Mapping the montane cloud forest of Taiwan using 12 year MODIS-derived ground fog frequency data". en. In: *PLoS One* 12.2 (Feb. 2017), e0172663.

[42] T Dinku et al. "Validation of satellite rainfall products over East Africa's complex topography". In: *International Journal of Remote Sensing* 28.7 (2007), pp. 1503–1526.

[43] Abolghasem Akbari et al. "Validation of TRMM 3B42 V6 for estimation of mean annual rainfall over ungauged area in semiarid climate". en. In: *Environ. Earth Sci.* 76.15 (Aug. 2017), p. 537.

[44] Mohammadali Alijanian et al. "Evaluation of satellite rainfall climatology using CMORPH, PERSIANN-CDR, PERSIANN, TRMM, MSWEP over Iran". In: *Int. J. Climatol.* 37.14 (2017), pp. 4896–4914.

[45] Pari-Sima Katiraie-Boroujerdy et al. "Trends of precipitation extreme indices over a subtropical semi-arid area using PERSIANN-CDR". en. In: *Theor. Appl. Climatol.* 130.1-2 (Oct. 2017), pp. 249–260.

[46] U.S. Geological Survey. *Global 30 Arc-Second Elevation (GTOPO30)*. 30.

[47] GJ Huffman et al. *NASA Global Precipitation Measurement (GPM) Integrated Multi-satellitE Retrievals for GPM (IMERG) Algorithm Theoretical Basis Document (ATBD) Version 5.2. 2018*. 2011.

[48] GJ Huffman. *IMERG Quality Index*. 2018.

[49] Arthur Y Hou et al. "The Global Precipitation Measurement Mission". In: *Bull. Am. Meteorol. Soc.* 95.5 (May 2014), pp. 701–722.

[50] Trevor Hastie, Robert Tibshirani, and Jerome Friedman. *The elements of statistical learning: data mining, inference, and prediction, Springer Series in Statistics*. 2009.

[51] Gareth James et al. *An Introduction to Statistical Learning: with Applications in R*. en. Springer Science & Business Media, June 2013.

[52] F Pedregosa et al. "Scikit-learn: Machine Learning in Python". In: *J. Mach. Learn. Res.* 12 (2011), pp. 2825–2830.

[53] B Thies, T Nauss, and J Bendix. *First results on a process-oriented rain area classification technique using Meteosat Second Generation SEVIRI nighttime data*. 2008.

[54] Toshiyuki Kurino. *A satellite infrared technique for estimating "deep/shallow" precipitation*. 1997.

[55] G Heinemann et al. *Investigation of summertime convective rainfall in Western Europe based on a synergy of remote sensing data and numerical models*. 2001.

[56] V Levizzani, P Bauer, and F Joseph Turk. *Measuring Precipitation from Space: EURAINSAT and the Future*. en. Springer Science & Business Media, May 2007.

[57] Michael R Chernick. *Bootstrap Methods: A Guide for Practitioners and Researchers*. en. John Wiley & Sons, Sept. 2011.

[58] Guoqiang Tang et al. "Accounting for spatiotemporal errors of gauges: A critical step to evaluate gridded precipitation products". In: *Journal of hydrology* 559 (2018), pp. 294–306.

[59] Viviana Maggioni and Christian Massari. "On the performance of satellite precipitation products in riverine flood modeling: A review". In: *Journal of hydrology* 558 (2018), pp. 214–224.

Chapter 3

Random forest-based rainfall retrieval for Ecuador using GOES-16 and IMERG-V06 data

Nazli Turini [1,*], Boris Thies [1] , Natalia Horna [2], and Jörg Bendix [1]

[1] Laboratory for Climatology and Remote Sensing, Faculty of Geography, Philipps-Universität Marburg, 35037 Marburg, Germany

[2] Instituto Nacional de Meteorología e Hidrología Dirección de Estudios, Investigación y Desarrollo Hidrometeorológico, Quito, Ecuador

---

This chapter is printed in ***European Journal of Remote Sensing, 54(1), 117-139***, DOI: https://doi.org/10.1080/22797254.2021.1884002

Abstract

Accurate rainfall information at a high spatiotemporal resolution for water resource management, particularly in water-scarce remote areas, is characterized by a coarse network of operational precipitation gauge stations. For such regions, satellite-based rainfall products potentially represent a source of reliable and area-wide data on rainfall. This paper presents an algorithm for satellite-based rainfall retrieval in Ecuador. The algorithm relies on the precipitation information from the Integrated Multi-SatEllite Retrieval for the Global Precipitation Measurement (GPM) (IMERG) and infrared (IR) data from the Geostationary Operational Environmental Satellite-16 (GOES-16). It was developed to (i) classify the rainfall area (ii) assign the rainfall rate. In each step, the most important predictors and hyperparameter tuning parameters were selected monthly. Between 19 April 2017 and 30 November 2017, brightness temperature derived from the GOES-16 IR channels and ancillary geo-information were trained with microwave-only IMERG-V06 product using random forest (RF). Validation was done against independent microwave-only IMERG-V06 data not used for model training. The validation results showed the promising performance of the new rainfall retrieval technique (multispectral), especially compared to the IR-only IMERG rainfall product. This indicates that using the multispectral IR data can improve the retrieval performance compared to single-spectrum IR approaches. The standard verification scored a median Heidke skill score of 0.6 for the rain area delineation and R between 0.5 and 0.62 for the rainfall rate assignment, indicating uncertainties for Andes's high elevation. Comparison of RF rainfall rates in 2 km^2 resolution with daily rain gauge measurements reveals the correlation of R = 0.33.

Keywords: Ecuador; GOES-16; GPM IMERG; machine learning; rainfall retrieval; random forest

3.1 Introduction

Precipitation is necessary to study the hydrological cycle and to support water management. In areas characterized by a coarse network of operational rain gauge stations, highly variable spatiotemporal precipitation patterns cannot fully be captured. This particularly holds for regions with a complex climate and topography [1]. Ecuador is one of such areas; the Andes Mountains characterize the country with the highest peaks exceeding elevations of 6268 above sea level (m.a.s.l.), bordered by the Amazon region in the east and the lowlands of the Pacific coast, where the southern coastal part has a semi-arid climate [2, 3, 4]. Because the rain gauge network is coarse in Ecuador, satellite-based rainfall products represent an alternative source

of reliable and area-wide information on rainfall.

Several products exist to derive rainfall from single or multispectral visible (VIS)/infrared (IR) and microwave (MW) sensors, and from merged MW and VIS/IR sensors (e.g., Climate Prediction Center MORPHing technique (CMORPH) [5], Precipitation Estimation from Remotely Sensed Information using Artificial Neural Networks (PERSIANN) [6, 7], and Tropical Rainfall Measuring Mission (TRMM) MultiSatellite Precipitation Analysis (TMPA) [8].

Concerning the combination of geostationary (GEO) IR with MW sensors on polar-orbiting satellites, empirical relationships between IR data and MW-based precipitation information can be derived for rainfall at a high spatiotemporal resolution [9, 10, 11]. Hong et al. [7], Huffman et al. [8], Kidd et al. [12], Levizzani, Bauer, and Joseph Turk [13] and Todd et al. [14] used the probability matching method between the cumulative distribution functions of the MW rain rate and the IR brightness temperature. Regression methods were applied by Kuligowski [15], Martin et al. [16], Miller, Arkin, and Joyce [17] and Vicente, Scofield, and Menzel [18], in which the MW-based rainfall estimates were related to coincident IR data. Huffman et al. [8] merged TRMM rainfall information with MW and GEO IR data in the TMPA product with accurate precipitation estimates at a high spatiotemporal resolution. Typically, MW-based rainfall data are used to calibrate IR-based products and fill the spatial and temporal gaps where MW data is not available. The Integrated Multi-SatEllite Retrieval for the Global Precipitation Measurement (GPM) (IMERG), the TRMM successor, the GPM [19] mission with its GPM core satellite and the so-called GPM constellation, provides a new global 30-min precipitation product with a 0.1° resolution [19]. Different studies have indicated the higher performance of the IMERG compared to other global satellite-based rainfall products ([20, 21, 22, 23, 24].

In Ecuador, several satellite-based rainfall products have been evaluated against gauge networks. PERSIANN [7] shows low consistency with daily rain gauge registration [25] in rain area detection. Manz et al. [23] compared the performance of TMPA and the IMERG against gauge data at different temporal (hourly, three-hourly, daily) resolutions. The IMERG showed better rain area detection and rainfall estimation than TMPA, particularly in the high Andes. In another study by Erazo et al. [26] in the high Andes, TRMM 3B43 Version 7 retrievals showed a high correlation of approximately 0.82 on a monthly scale compared to the interpolated gauge information at a spatial resolution of 0.25°.

Concerning the above-stated use of multiple sensors to increase the accuracy of satellite-based rainfall retrievals, new-generation GEO multispectral sensors, such as Meteosat Second-Generation Spinning Enhanced Visible and Infrared Imager (MSG SEVIRI), HIMAWARI, and the Geostationary Operational Environmental Satellite 16 (GOES-16), offer the potential to use more spectral bands for rainfall retrieval. This higher spectral information can improve the IR-only part of the IMERG product, relying solely on the 10.8 µm channel. Several studies have documented improved satellite-based rainfall estimation by integrating full spectral information compared to a single IR channel [27, 28, 29, 30, 31, 32, 33, 34].

On the regional scale, new GEO satellite systems offer the possibility to retrieve rainfall information at a higher spatiotemporal resolution compared to the IMERG product (GOES-16 (10 min, 2 km^2), MSG SEVIRI (15 min, 3 km^2), and HIMAWARI (10 min, 2 km^2)). This would allow capturing smaller-scale rainfall events that occur due to topographic forcing and other local precipitation processes in a more accurate way [23, 35, 36, 37].

Although the remote sensing of rainfall at a high spatiotemporal resolution is becoming more prevalent, the main challenge of combining data from diverse sensors to make strides in inconsistency, precision, scope, and convenient rainfall estimates still remains [27]. Recently,machine learning (ML) techniques have been used to retrieve rainfall from multispectral GEO data [6, 7, 29, 30, 31, 32, 33, 34, 38, 39]. They offer high potential for dealing with nonlinear and complex relationships between a target variable, such as rainfall, and its predictors [40]

The objective of this study was to provide accurate rainfall information at a high spatiotemporal resolution for Ecuador. We aimed to develop an algorithm to generate regionally adapted rainfall products for Ecuador based on the new GOES-16 system. The high spatiotemporal resolution of GOES-16 offers excellent potential to provide rainfall information in a quasi-continuous manner. The algorithm uses multispectral IR from GOES-16 to estimate surface rainfall rates based on RF [41]. Microwave-only precipitation information from IMERG-V06 was used as a reference to train the RF model (see the section 3.2.4.3 for more detail). The developed algorithm includes two steps: (i) Classification of the rainfall area and (ii) assignment of the rainfall rate. In each step, feature selection and tuning of the RF model are implemented. We validated the RF model results against the independent microwave-based IMERG-V06 rainfall data not used for model training. To analyze a potential improvement in comparison to algorithms that rely only on one infrared channel we also validated

the results of the IMERG IR-only dataset against the MW-based rainfall data. Additionally, we applied the RF models to an independent time period and validated the results with independent gauge data. In this step, we also validated the results of the IR-only IMERG products against the gauge data.

3.2 Methodology and data

3.2.1 The architecture and configuration of the rainfall retrieval model

We developed a new satellite-based rainfall retrieval method that uses a combination of GEO data and polar orbiting MW-based rainfall information to produce high spatio-temporal rainfall information. The novelty is the application of machine learning random forest methods for this purpose. Microwave-only precipitation information from the IMERG-V06 was used as a reference to train the RF models. The RF rainfall retrieval algorithm workflow is shown in Figure 3.1. The algorithm was developed in a processing framework in Python 2.7 using the Scikit-learn 0.20.2 package [42].

In the first step, the predictors and the target variable (i.e., rainfall) are processed to generate training/validation and application datasets in the same spatiotemporal resolution. Rainfall area delineation is then conducted by RF classification, where all cloudy pixels from the binary class of cloud mask (BCM) [43] are classified into rainy or non-rainy. After the rainfall rate assignment is realized by RF regression, the respective RF regression model is applied to the second step's RF classification model. The quality of both RF models (i.e., the RF classification and RF regression models) is assessed using the validation dataset. Finally, the RF models are applied to the independent time period and validated against the independent gauge data.

The RF classification and RF regression training is conducted based on the MW overpasses in the IMERG, and the feature selection and tuning of the hyperparameters are performed monthly. The term "feature" used in the RF models has the same meaning as "predictor." The number of available models for one day ranges from 1 to 4 on average, depending on the time of year (Figure 3.2). In regions with complex topography, the higher temporal resolution models lead to better precipitation estimates [29].

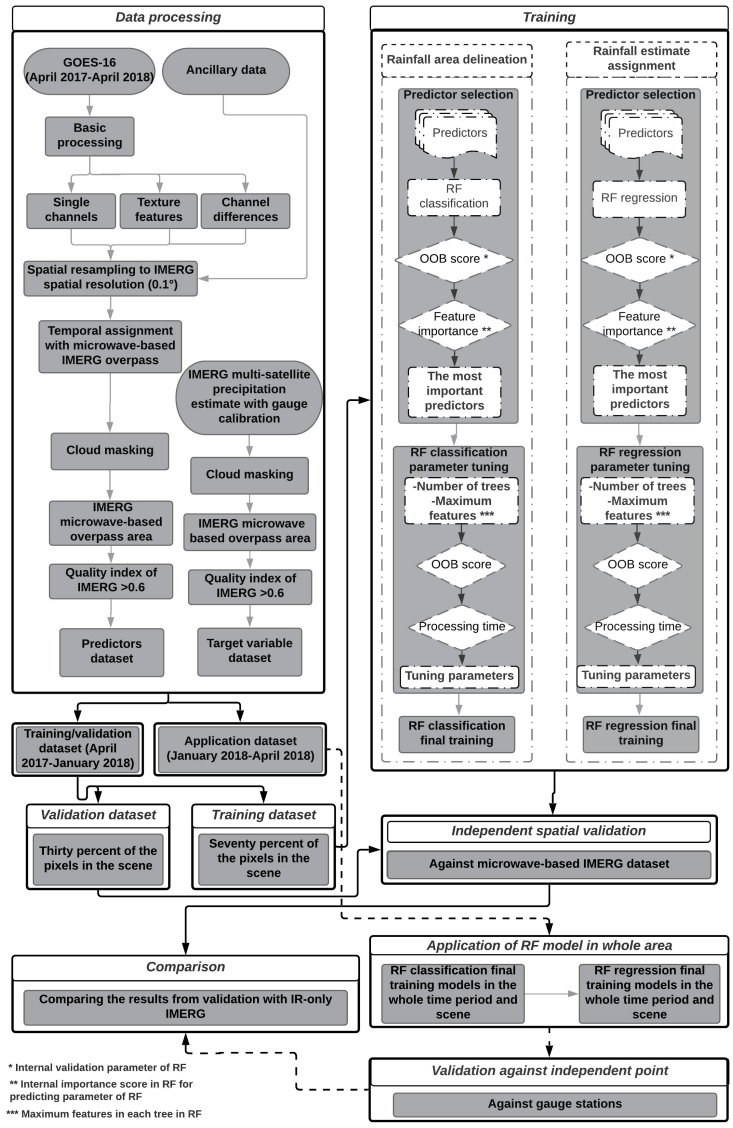

Figure 3.1: The adapted workflow of the rainfall retrieval for Ecuador with the new GOES-16 system. GOES-16; IMERG; OOB; RF.

3.2.2 Data processing—matching between GOES-16 and the microwave-based IMERG

To train and validate the rainfall retrieval model, multiband GOES-16 Advanced Baseline Imager (ABI) IR data, IMERG data, and the digital elevation model (DEM) were downloaded and extracted for Ecuador (Figure 3.1—data processing stage). he GOES-16 and IMERG data were processed in Python 2.7. Because of the different spatial resolutions of the GOES-IR bands and the BCM (2 km^2), IMERG (11 km^2),

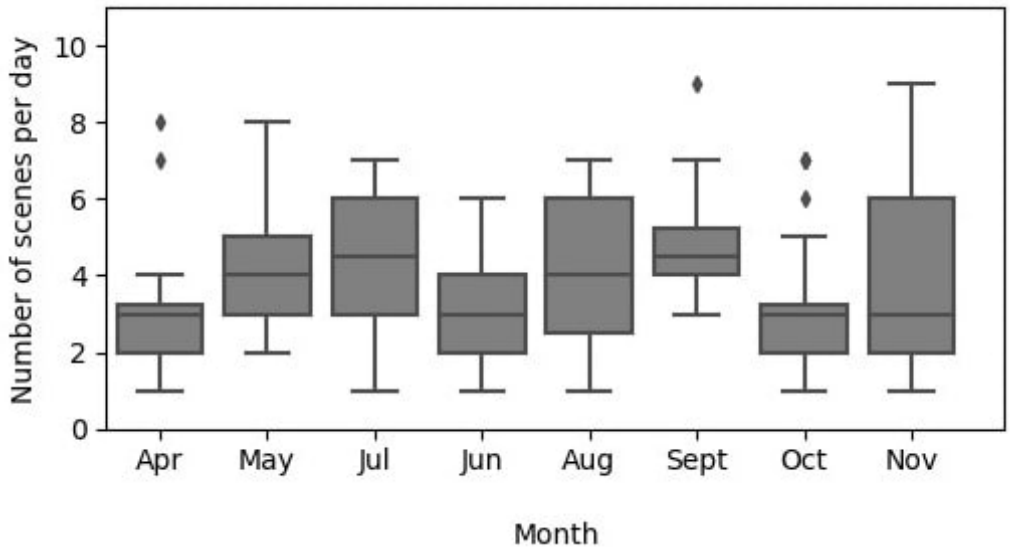

Figure 3.2: The number of scenes with enough data for the RF model training and validation for Ecuador. Boxes show the 25th, 50th, and 75th percentiles. Whiskers extend to the most extreme data points between the 75th and 25th percentiles. Outliers are shown as diamonds.

and DEM (1 km^2), we used the average resampling techniques in gdal [44] to ensure pixel matching between the different datasets. All of the data were projected to WGS84 and resampled to the spatial resolution of the IMERG (11 km^2).

We used different sub-datasets in the IMERG product (Table 3.A.1 in Appendix 3.A). We selected training and validation pixels from "precipitationCal" when the overpass of passive microwaves (PMWs) was available ("HQobservation"). We filtered the pixels where the "PrecipitationQualityIndex" was >0.6 (which indicates the current half-hour microwave swath data) [45].

In the pixels of the training and validation datasets, we also selected the "IRprecipitation" from the IMERG. This dataset provides level 3 IR retrieval from PERSIANN-CCS in the IMERG. These IR data are calibrated to the merged PMW-only estimates regionally [45]. We used this dataset to compare it to the results of our rainfall retrieval.

To compile the most solid dataset for model training and validation, we defined the following criteria: (i) For temporal matching; we collected paired GOES-16 and the microwave-based IMERG where the difference in the observation time (scan time for GOES and "HQobservationTime" for the IMERG) between both datasets was within 7 min; (ii) the IMERG "PrecipitationQualityIndex" was considered to select pixels

with the high-quality merged MW-only precipitation estimates ("HQprecipitation"); (iii) following Hou et al. [46], we used a threshold of 0.2 mm/h to distinguish between rainy and non-rainy pixels in the IMERG product; (iv) we only considered cloudy pixels detected by the BCM. The predictor variables listed in Table 3.1 were extracted for the pixels fulfilling all criteria only, together with the corresponding MW-only precipitation estimate. Then the dataset is divided into training/validation dataset and application (temporally independent validation). The training/validation dataset was randomly divided into a training dataset (70%) and a validation dataset (30%).

Table 3.1: Overview of the predictor variables considered for the RF regression and the RF classification. Geostationary Operational Environmental Satellite (GOES) bands are shown with their central wavelength in micrometers (μ). ΔT indicates the temperature band differences. CV, cross-variogram; EL, terrain elevation; IR, infrared; MAD, madogram; PCV, pseudo-CV; ROD, rodogram; TPI, Topographic Position Index; TRI, Topographic Ruggedness Index; VAR, variogram; WV, water vapor

GOES satellite		Ancillary geoinformation
GOES bands	Derived data	
IR 3.9	ΔT (all band combination)	ELV
WV 6.2	VAR (all bands)	TPI
WV 6.9	MAD (all bands)	TRI
WV 7.3	ROD (all bands)	Slope
IR 8.4	CV (all band combination)	Aspect
IR 9.6	PCV (all band combination)	
IR 10.3		
IR 11.2		
IR 12.3		
IR 13.3		

To consider the complex diurnal precipitation processes in Ecuador, the above mentioned approach was applied on a scene-based, whenever possible. According to the criteria mentioned above, whenever enough rainy pixels of the MW-based IMERG rainfall product were available for a scene of the study area, we compiled a scene-based dataset. Of this scene-based dataset 70% of the pixels were used for model training and the remaining 30% of the pixels were used for validation.

Figure 3.2 provides an overview of the number of scenes used for the RF model training and validation in Ecuador for each month. The overall pixels used for the RF model training and validation were 1,202,213 and 516,145, respectively.

3.2.3 Training and validation of the RF models

3.2.3.1 Model training and hyperparameter selection for the RF models

For rain area delineation cloudy pixels were separated into rainy and non-rainy areas by the implementation of RF classification in Scikit-learn-0.20.2 [42] in Python 2.7 (Figure 3.1—Training). The classification training dataset was extremely unbalanced. The average ratio between the non-rainy and rainy pixels in a scene was approximately 10:1. To address this imbalance, we kept all of the observations belonging to the minority rainy class (microwave-based IMERG >0.2 mm/h) and randomly selected (with replacement) non-rainy pixels according to different ratios (Table 3.A.2 in Appendix 3.A). Finally, we decided on five times more non-rainy pixels than rainy pixels, which provided the highest Heidke skill score (HSS) (Table 3.A.2 in Appendix 3.A).

The first step for RF classification is determining the most important predictors and hyperparameter tuning (Figure 3.1-Training). Both steps are conducted monthly. Concerning feature selection, a common precipitation retrieval approach based on GEO IR data is defining a relationship between cloud-top brightness temperatures and reference rainfall amounts, assuming the rainfall rate increases as the cloud-top temperature decreases. As shown in several studies [6, 27, 34], other GEO-derived rainfall-relevant features could improve rainfall retrieval from satellites.

In this study, selecting the most important predictors was achieved by applying recursive feature elimination (Figure 3.A.1 in Appendix 3.A). This process determines the best-performing predictor sets out of the initial predictor space (Table 3.1). The RF modeling was started with all 181 predictors, and the least significant predictors were removed based on the "feature importance" metrics using Scikit-learn for RF methods [41]. At the end of each iteration, before removing the least important predictor, the model's quality was calculated using the out-of-bags (OOB) score [41, 42]. Ultimately, we filtered the predictors with the best average ranking based on feature importance and the highest OOB score from the original set of 181 monthly.

Then, to obtain robust RF performance results, we tuned and optimized the hyperparameters. We iteratively tuned the hyperparameters monthly, including the total number of decision trees and the number of input features (n) used at each node, to determine the optimal setting for the RF classification. Moreover, a grid search of the parameter options was conducted to identify the best combination of hyperparameters based on the OOB score and optimal processing time.

For addressing the imbalance between the non-rainy and rainy pixels monthly, we selected 2000 pixels randomly from the minority class (rainy pixels) and 10,000 pixels from the majority class (non-rainy pixels) for both the predictor selection and the hyperparameter tuning [34]. Additionally, we used the 'class_weight='balanced' in RF from Scikitlearn0.20.2 [42] to include a balanced weight bootstrap subsample of the RF models. This balance mode automatically adjusts weights inversely proportional to the class frequencies [42]. To ensure spatially and temporally robust results, we repeated the predictor selection and hyperparameter tuning 50 times to produce 50 independent datasets of randomly selected pixels for each month [34].

For the rainfall rate assignment, the RF regression model was trained with rainfall information from the microwave-based IMERG (rainfall rate >0.2 mm/h). The feature selection and hyperparameter tuning were conducted in the same way as for the RF classification. As rainfall rates are not evenly distributed, unbalanced rainfall datasets are difficult to predict by RF. To obtain more balanced rainfall datasets, we applied two different undersampling methods. In this case, undersampling signifies the removal of low rainfall rates with high frequencies in favor of high rainfall rates with low frequencies.

The first undersampling was applied during the monthly feature selection and hyperparameter tuning. We classified the rainfall rate monthly with a range of 1 mm/h and estimated the probability of occurrence (PO) of every class. The average probability of occurrence (APO) was calculated by simply summing up all POs to the number of defined classes each month. If the PO in a class was higher than the APO, we randomly selected rainfall pixels from said class until the PO reached the APO. If the classes of precipitation rate ranges contained fewer pixels than the APO, we took all of these classes' values.

We applied the second undersampling during the monthly feature selection and hyperparameter tuning and on the RF scene-based training. Here, we used the sample weight in the fit command of the RF package "compute sample weight," which assigns a balanced weight to each rainfall class in the bootstrap subdataset [42]. Table 3.A.3 in Appendix 3.A summarizes the model's performance with and without applying the classweight or computesampleweight functions in RF.

3.2.3.2 Validation of rainfall area delineation and rainfall rate assignment

The result RF classification and RF regression was validated against the independent microwave-based IMERG rainfall from the validation datase. Validation was done for

the detected rainfall area and the assigned rainfall rate separately and the combined final rainfall product (RF-combined).

To analyze the performance of the RF classification, we calculated the HSS, probability of detection (POD), and false alarm ratio (FAR) in the study area over the study period (Table 3.A.4 in Appendix 3.A). Meanwhile, to evaluate the performance of the RF regression, we used the correlation coefficient (R), the root-mean-square error (RMSE), and the mean absolute error (MAE) (Table 3.A.4 in Appendix 3.A). The validation statistics were calculated for every scene for which enough validation pixels were available. To analyze a potential improvement of our approach compared to existing retrieval models that rely only on one IR channel, we validated the IR-only sub-dataset in the IMERG in the same way.

We have also used these validation metrics to analyze the spatial performance of the rain area delineation and rain rate assignment. We evaluated all metrics for each pixel in the study area. Moreover, to better understand the model performance with respect to the rainfall rate in the different regions, the relative RMSE and MAE were calculated by dividing their values in each pixel by the average MW-based IMERG rainfall rate over the whole period. Furthermore, the mean differences between the MW-based IMERG rainfall rate and the RF-combined model from the validation dataset were investigated. To calculate the mean difference, we subtracted the MW-based IMERG rainfall in each pixel from that of the RF-combined model and averaged it over the whole period.

3.2.3.3 Application and validation of the model in GOES native resolution

To generate the RF rainfall retrieval at a high spatiotemporal resolution (2 km^2, 15 min), we applied the models in the scenes where the microwave-based IMERG was available in the same time slot and the following scenes until the next microwave-based IMERG RF model was available.

To analyze our approach's potential improvement compared to the IR-only IMERG, we also generated the RF rainfall retrieval for 11 km^2 and 15 min. The rainfall area delineation and rainfall rate assignment's overall performance was investigated against gauge stations (Figure 3.4) ffor the studied period using the HSS and R, respectively (Table 3.A.4 in Appendix 3.A). For this purpose, the RF rainfall retrieval data (15 min and 2 km^2/11 km^2) were aggregated to the gauge data's daily resolution. The aggregation was conducted when at least 92 scenes of the RF rainfall retrieval were available. The RF-only IMERG data were aggregated daily when at least 42 scenes

from the IR-only IMERG were available. We used a threshold of 0.6 mm/day to delineate between rainy and non-rainy days. The R was calculated for days with rain in all datasets.

3.2.4 Dataset

3.2.4.1 GOES

GOES-16 is placed at 75.2°W longitude as its operational location [47, 48]. TThe primary instrument is the Advanced Baseline Imager (ABI), a multispectral passive imaging radiometer. ABI measures the Earth's radiance in 16 spectral channels ranging from visible (0.47 µm) to long-wave IR (13.3 µm) every 15 min. Included are ten IR bands between 3.9 and 13.4 µm with a nominal spatial resolution of 2 km^2 at the sub-satellite point. GOES-16 has been available since 19 April 2017, and this study used data from only one year, 19 April 2017 to 19 April 2018. The dataset from 19 April 2017 to 30 November 2017 is used for training and validation, and the dataset between 1 January to 19 April 2018 is used for application and temporally independent validation of the algorithm.

Several studies have shown that multispectral satellite data provide information about microphysical and optical cloud properties [49, 50, 51, 52, 53]; therefore, such data can improve satellite-based rainfall retrievals [29, 30, 31, 32, 34]. Thies, Nauss, and Bendix [54] demonstrated that the channel differences between IR bands provide information about the cloud phase, the cloud top, and the cloud water path, which can improve satellite-based rainfall retrievals [29, 32, 34]. We, therefore, considered the IR bands and the IR channel differences as predictor variables in our RF-based approach.

Spatial information, such as the variance within spectral bands, which are important for capturing clouds' heterogeneity, cannot be obtained by only looking at single pixel values [55]. Information about the spatial variance within a given raster dataset has improves the output of satellite-based cloud detection and rainfall retrieval techniques [29, 30, 34, 55, 56]. To consider the spatial variability of raining clouds, texture features were calculated from these predictor variables using a 5 × 5 pixel moving window approach. For individual predictors, variograms (VARs), madograms (MADs), and rodograms (RODs) were calculated, while for each possible predictor variable combination, cross-variograms (CVs) and pseudo cross-variograms (PCVs) were calculated [29, 30, 34, 55] (please refer to Schultz et al. [56] for more

information). IIn addition to the GOES-16 IR channels, the BCM was used to restrict the rainfall retrieval algorithm to cloudy pixels. A list of the predictors based on GOES spectral bands is shown in Table 3.1.

3.2.4.2 Ancillary geo-information

Due to their high weather variability, mountainous regions present a great challenge to satellite-based rainfall retrievals [57, 58]. Therefore, in this study, the terrain elevation (ELV), Topographic Position Index (TPI), Topographic Roughness Index (TRI), slope, and aspect (orientation of the slope) were considered. The ELV was provided by the Global 30 Arc-Second Elevation DEM [59]. The TRI, slope, and aspect were retrieved from the ELV in GRASS GIS-7 [60], and the TPI was calculated from the ELV in SAGA [61]. Table 3.1 provides an overview of the predictors. Initially, we considered 181 predictors for the development of the RF models.

3.2.4.3 IMERG

The IMERG is a product that merges and intercalibrates all available MW-based precipitation estimates, MW-calibrated IR estimates, and rain gauge measurements globally [45]. Here, we used the IMERG-V06, which is the latest available version, for which Tan et al. [62] demonstrated the general improvement in the precipitation field compared to version-05. The IMERG-V06 uses five PMW instruments to estimate rainfall. The PMW precipitation estimates were intercalibrated by applying the CMORPH algorithm [5] to compute the motion vectors from the IR measurements and the diverse atmospheric variables in numerical models to produce the gridded rainfall at a fine resolution quasi-globally (11 km^2, 30 min). This gridded product was completed by microwave-calibrated rainfall estimates retrieved from an artificial neural network model from PERSIANN-CCS [7] and GEO IR. The final rainfall estimate was calibrated with monthly gauge data from the Global Precipitation Climatology Center (GPCC) [45] (for more information, refer to Huffman et al. [45]). The different sub-datasets in the IMERG final half-hourly product used in this study are shown in Table 3.A.1 in the Appendix 3.A.

The microwave-based rainfall estimates from the IMERG-V06 product with the highest quality (see section 3.2.2) were used as a reference for developing the GOES-IR rainfall retrieval. The spatial distribution of the MW-based IMERG average rainfall rate for the study period is illustrated in Figure 3.3a. Overall, the rainfall rate varied between 0.2 and >8 mm/h. The rainfall distributed unevenly

over the country, depending on the altitude of the regions. The Amazon area was rainier compared to the Andes and the Pacific coastal plains. The rainfall in mountainous areas showed more variability in space, ranging between 0.2 and 6 mm/h. In transition areas from the Andes to the Amazon rainforest, the rainfall rate increased, mostly in the southeast of Ecuador. The rainfall in these regions was predominantly of the subscale convective systems [63]. For the semi-arid areas in the Southwest of Ecuador and the Northwest of Peru lower rainfall rates between 0.2 and 4 mm/h can be seen.

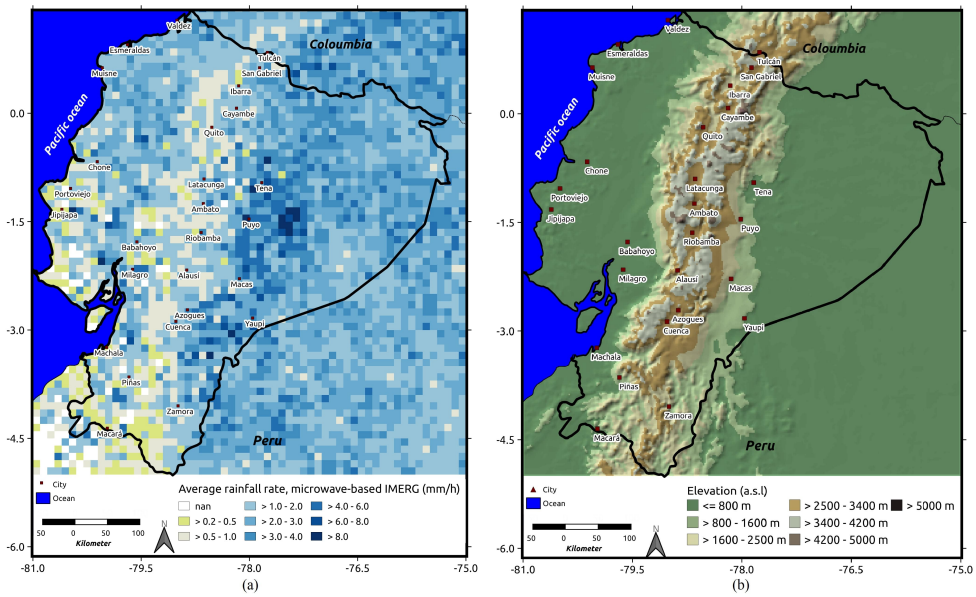

Figure 3.3: Spatial distribution of (a) the microwave-based IMERG average rain rate from 19 April 2017 to 30 November 2020, and (b) the elevation.

3.2.4.4 Gauges

We used a rain gauge network comprising 22 stations with daily resolution (Figure 3.4) to validate the final RF rainfall retrieval. The data were acquired from the National Institute of Meteorology and Hydrology (INAMHI) in Ecuador. These data are not part of the GPCC network and were thus not considered for the gauge-calibrated final IMERG product.

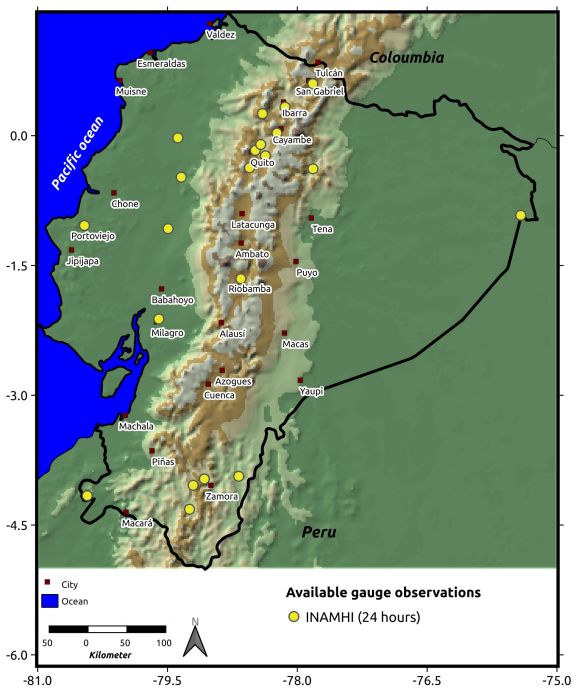

Figure 3.4: The distribution of the gauges used in this study. INAMHI, National Institute of Meteorology and Hydrology.

3.3 Results

3.3.1 Feature selection and the most important predictors

Figure 3.5a illustrates the optimum number of predictors for RF classification (orange) and RF regression (blue) with the respective optimum OOB score. The RF classification showed a number of features between 18 and 25 for an OOB score of approximately 0.85 and did not vary much between the months. The RF regression offered a higher variability between the months, with the best model performance for 25 features with an OOB score of 0.6. Figure 3.5b shows the selected features and the feature importance for both the RF classification and the RF regression. Ancillary geoinformation played a vital role in modeling the rain area and the rainfall amount, which is not surprising, as elevation played a crucial role in the rain dynamics. The texture features were also identified as important predictors for the RF models. This especially holds for the PCV calculated for the different channel combinations.

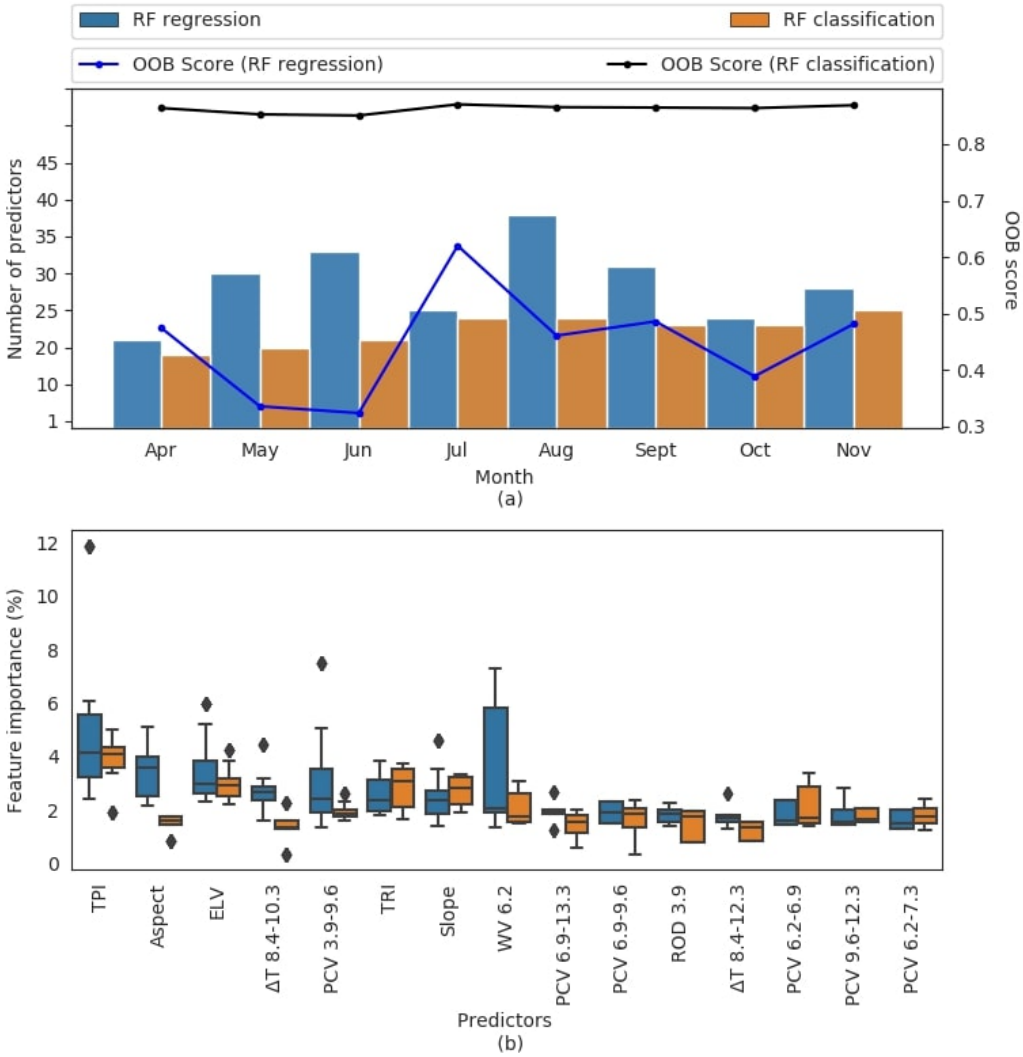

Figure 3.5: Feature selection: (a) Number of features selected for the RF classification and regression with the related optimum OOB score for the training/validation period. (b) The most important predictors and related features for both the RF classification and the RF regression. The predictors were selected when chosen at least three times for both the RF regression and the RF classification. Boxes show the 25th, 50th, and 75th percentiles of the feature importance. Whiskers extend to the most extreme data points between the 75th and 25th percentiles. Outliers are shown as diamonds.

3.3.2 Temporal validation of the RF rainfall retrieval

To assess the quality of the RF rainfall retrieval during the validation/training period (19 April 2017 to 31 November 2017), verification scores for the RF classification, the

RF regression, and the RF-combined model were investigated. The verification scores are shown as a monthly boxplot to understand the model performance at different times of the study period (Figure 3.6, Figure 3.7, and Figure 3.8). December 2017 was not included due to the low availability of GOES-16 data.

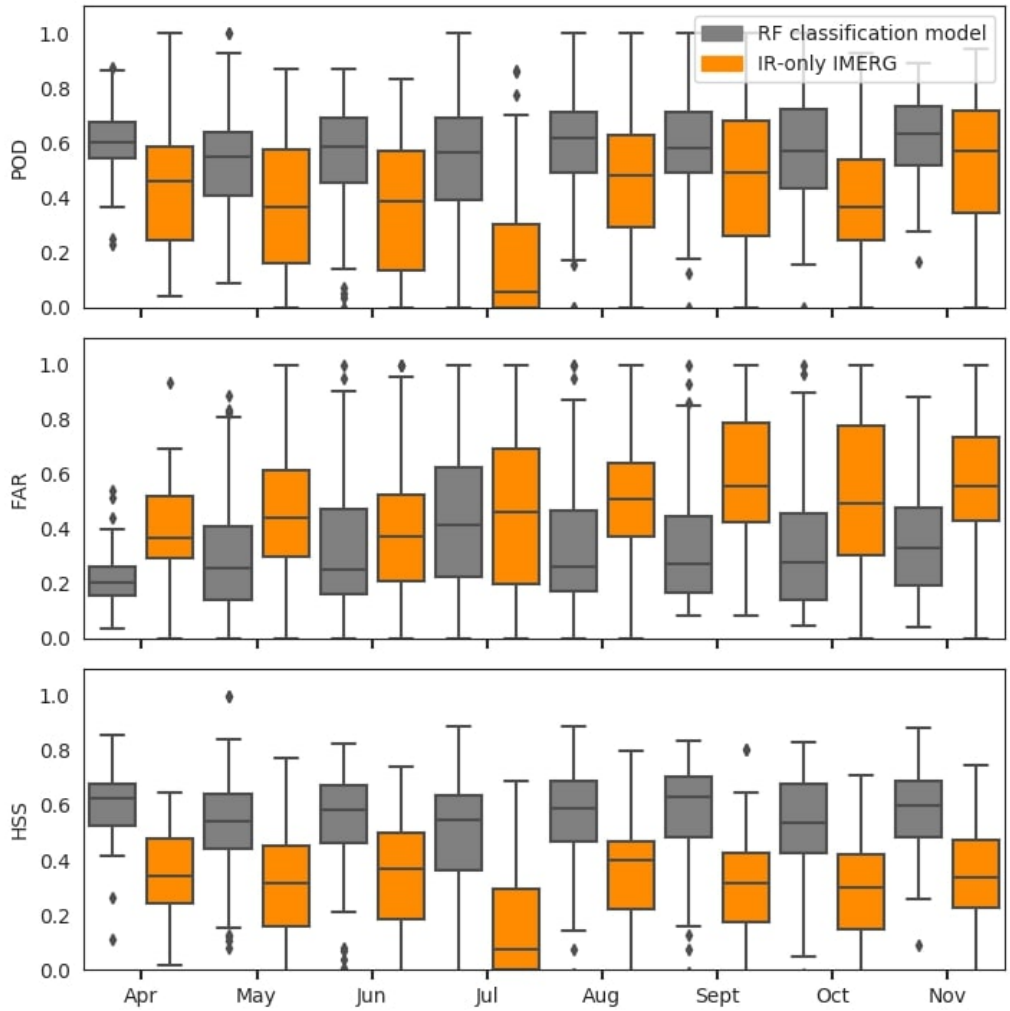

Figure 3.6: Box plots of the verification scores for the rainfall area delineation (RF classification), over the microwave swath in training/validation period. Boxes show the 25th, 50th, and 75th percentiles. Whiskers extend to the most extreme data points between the 75th and 25th percentiles. Outliers are shown as diamonds.

The boxes show the monthly 25th, 50th, and 75th percentiles of the verification indices. The whiskers extend to the maximum and minimum verification scores in a month between the 75th and 25th percentiles. Beyond the whiskers, the scores are

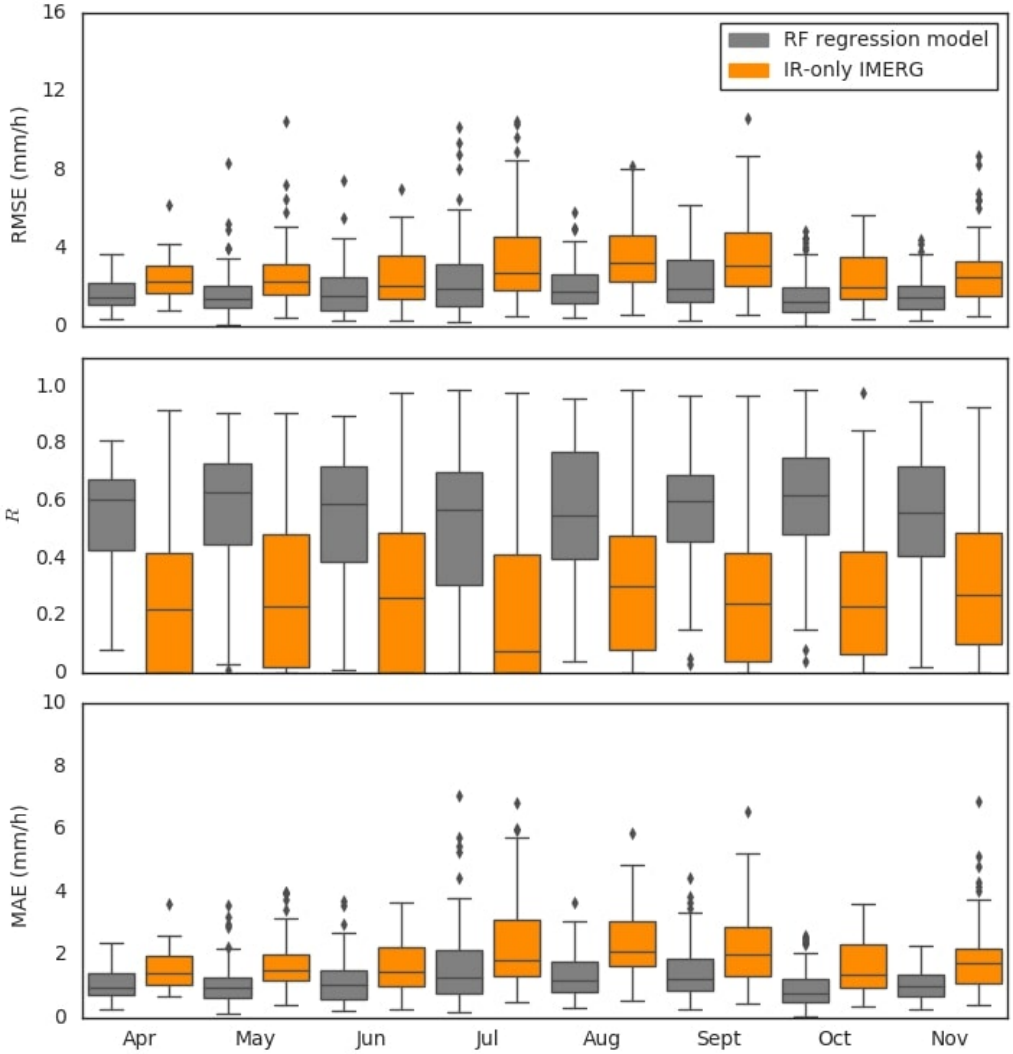

Figure 3.7: Box plots of the verification scores for the rainfall rate assignment over the microwave swath in training/validation period. Boxes show the 25th, 50th, and 75th percentiles. Whiskers extend to the most extreme data points between the 75th and 25th percentiles. Outliers are shown as diamonds.

considered outliers and are plotted as individual diamonds [64].

Regarding the RF classification (Figure 3.6, the median of the POD per month varied between 0.55 and 0.63 in October 2017 and November 2018, respectively. The overall performance indicated by the HSS experienced slight changes between the different months, with higher amplitudes in April and September and an overall median of HSS of 0.6. The average FAR per month ranged from 0.21 to 0.4. Compared to the IR-only IMERG, the RF classification models show better

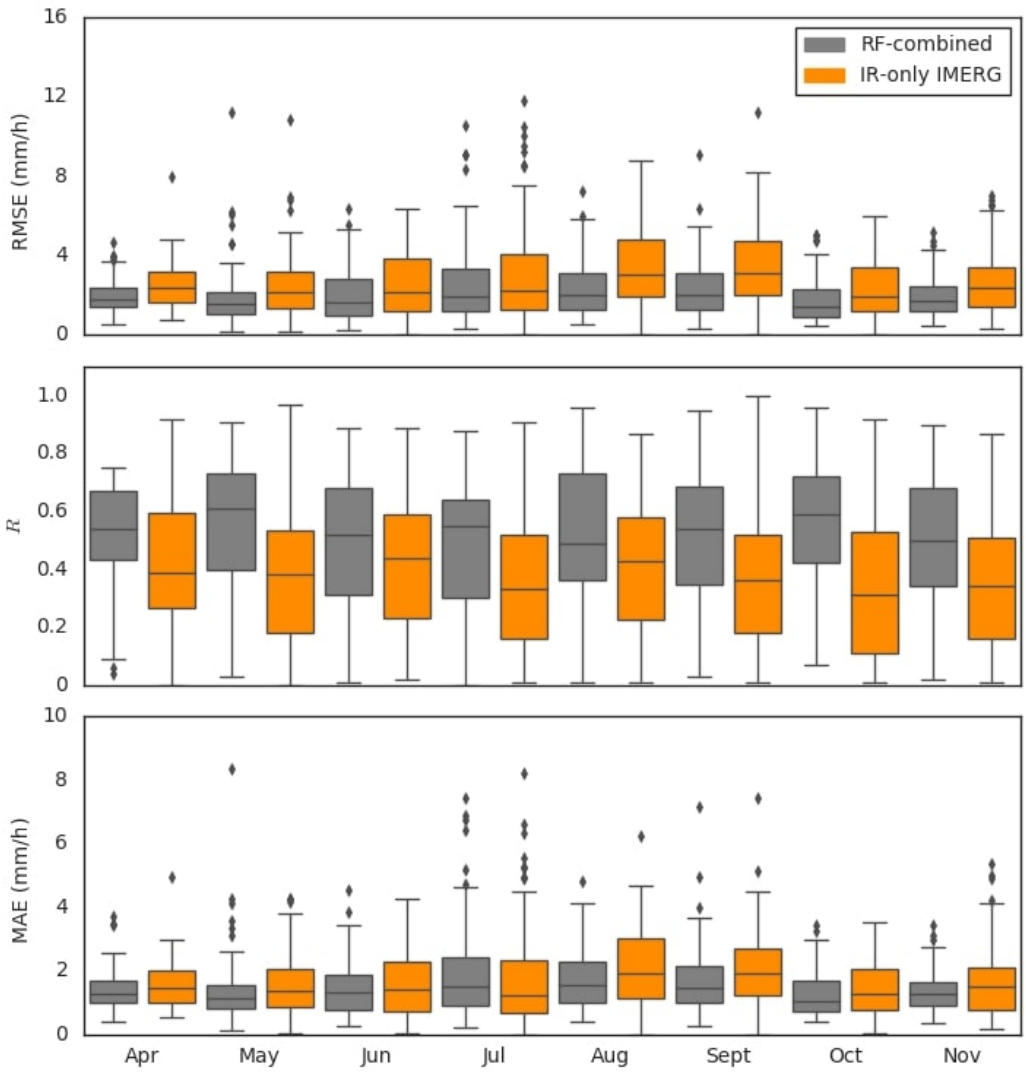

Figure 3.8: Box plots of the verification scores for the rainfall rate assignment combined with the rain area delineation (RF-combined model), over the microwave swath in training/validation period. Boxes show 25th, 50th, and 75th percentiles. Whiskers extend to the most extreme data points between the 75th and 25th percentiles. Outliers are shown as diamonds.

performance.

For the RF regression, the median of the R, RMSE, and MAE per month (Figure 3.7) was 0.6, 1.5 mm/h, and 1.4 mm/h, respectively. The monthly variation in the values indicated no changes. As with the RF classification, the RF regression model outperformed the IR-only IMERG results.

Altogether, the RF-combined model validation resulted in R values between 0.5 and 0.62 (Figure 3.8). Compared to the validation results for the independent

RF regression (Figure 3.7), this is of lower quality. Again, the RF-combined model outperformed the IR-only IMERG.

Figure 3.9 displays the monthly mean and maximum rainfall amounts for the RF-combined model and the MW-based IMERG. Concerning the mean rainfall rate, the RF-combined model showed an overestimation compared to the MW-based IMERG, although the annual cycle was in good accordance in both datasets. The extreme events were analyzed if the maximum rainfall amount per month in the MW-based IMERG could be reproduced by the RF-combined model for the same location and the same time step. The graph indicates that the RF models had problems detecting high rainfall amounts compared to the MW-based IMERG and underestimated the rainfall amount.

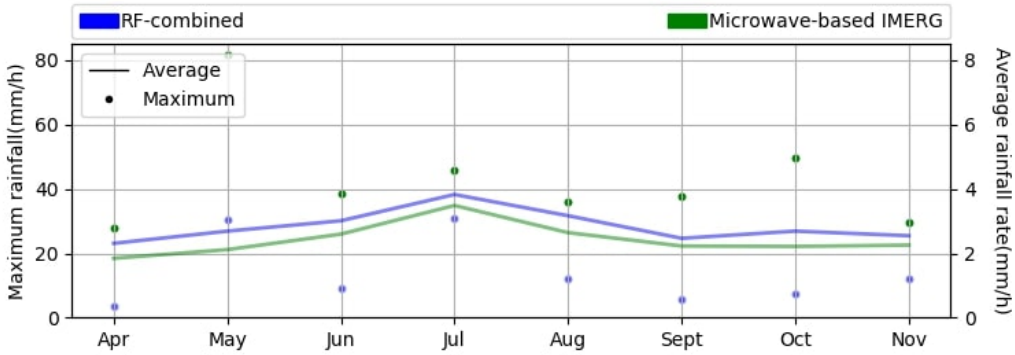

Figure 3.9: The monthly mean and maximum rain rates for RF-combined model and the microwave-based IMERG in the training/validation period.

3.3.3 Spatial validation of the RF rainfall retrieval

Figure 3.10 shows the spatial performance of the RF classification for the studied period. The HSS (Figure 3.10a) and POD (Figure 3.10b) share similarities in their spatial distribution. In the east of Ecuador, with the Amazon rainforest and a higher average rainfall rate (Figure 3.3a), the overall performance of the RF was better, proven by higher POD (Figure 3.10 b), higher HSS (Figure 3.10a), and lower FAR (Figure 3.10c) values.

Along the Ecuadorian coast with lower average rainfall rates (Figure 3.3a), the HSS (Figure 3.10a) was between 0.1 and 0.8 with higher uncertainties near the cities of Jipijapa (in the south) and Muisne (in the north). The performance of the RF classification models seemed to be influenced by the topography (Figure 3.3 b). The HSS values (Figure 3.10a) are lower in areas around the peak elevations near Azogues,

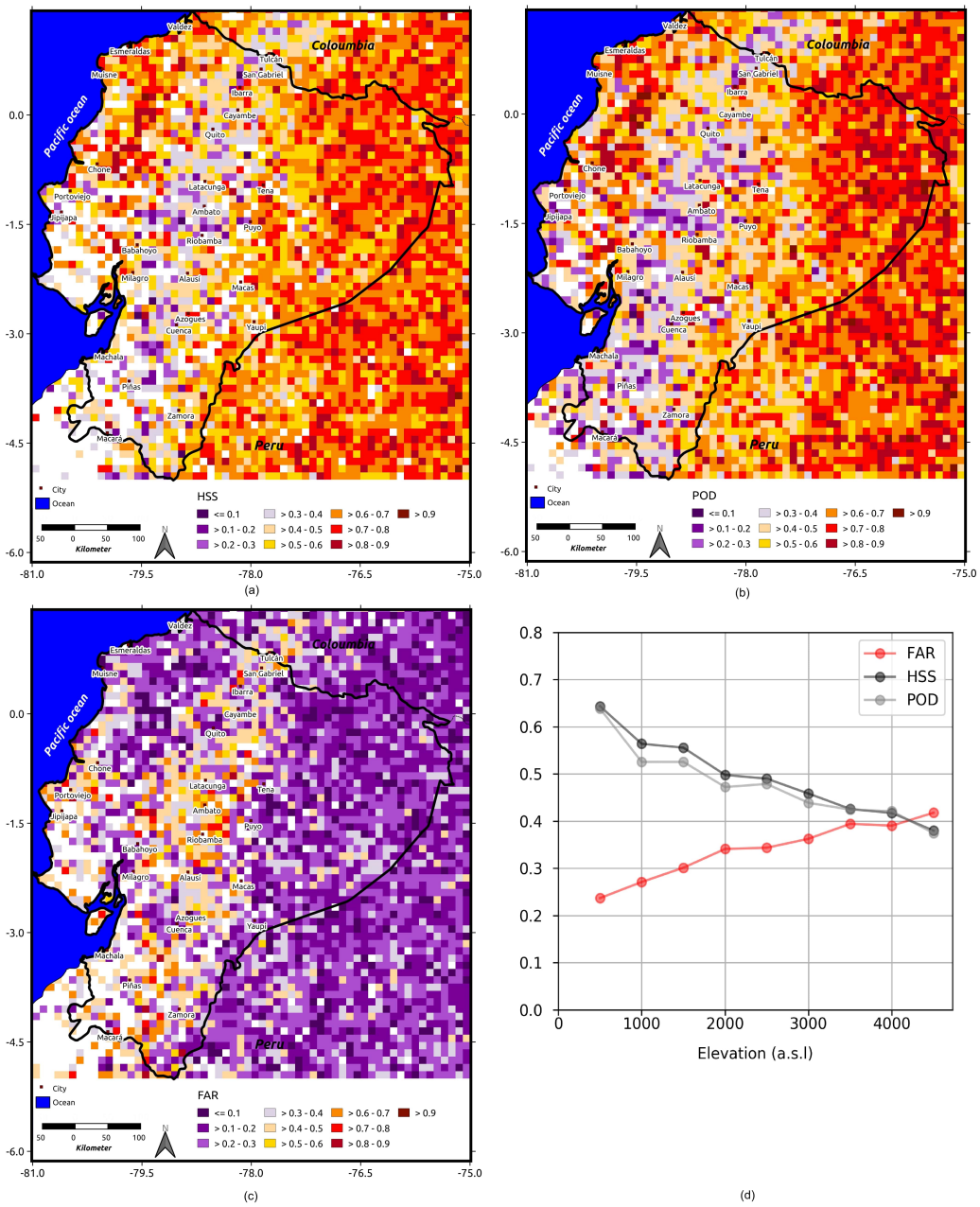

Figure 3.10: Distribution of (a) POD, (b) FAR, and (c) HSS in the study region for the retrieval of the rain area. The performance of the RF classification along the elevation is shown in (d) over the training/validation period. The variables were calculated for each grid point of the validation dataset over the training/validation period.

Ambato (Chimborazo area), Cuenca (Cajas National Park), and Sangolqui-Quito (Pichincha volcano). The FAR (Figure 3.10c) showed comparatively higher values in

these high-elevation areas.

The RF classification showed some uncertainties from the coastal transition areas to the Andes and the Andes to the Amazon rainforest. As an example, this was indicated by the high FAR value of approximately 0.75 at –78.5°W and –1.5°S (Imbabura Volcano), as well as the lower POD and HSS values for these regions. Altogether, the evaluation results indicate inaccuracies in the RF classification for the highest elevations around the volcanoes.

Figure 3.10d provides an overview of the RF classification performance, along with the altitude. A terrain elevation of approximately 0–500 .a.s.l has the best performance; such heights are located in the Amazon and the coastal areas (Figure 3.3b). With increasing elevation, the rain area delineation's performance decreased until 3500 .a.s.l For regions above 3500 .a.s.l, the models performed poorly. Altogether, the graph confirms the low performance of the rain area delineation in the higher elevation and volcano regions of the Andes.

The evaluation results of the RF-combined model are displayed in Figure 3.11. The calculated mean differences between the average rainfall rates from the RF-combined model and the MW-based IMERG product indicates an overestimation by the RF-combined model over almost the entire Ecuador. In the mid-east of Ecuador and the southern parts of the Andes, the RF-combined model showed an underestimation. Moreover, across the eastern slopes of the Andes, with generally higher rainfall rates, the model underestimated the rainfall (Figure 3.3).

The relative MAE (Figure 3.11b) and relative RMSE (Figure 3.11c) show similar spatial performances, which seem to be related to the spatial distribution of the average rainfall rate in Figure 3.3a. For areas with lower average rainfall rates in mountainous regions, higher relative MAE and RMSE values were calculated. This is also true for the western parts of the coastal plains and the semi-arid areas of northwestern Peru and southwestern Ecuador. The RF-combined model performed better in the Amazon basin. Figure 3.11d shows the better performance of the RF-combined model for higher rainfall rates concerning R and MAE. The mean differences between the MW-based IMERG and RF-combined model rainfall rates increased for higher rainfall rates.

The RMSE and MAE values for the study area are between 0 and 4 mm/h (Figure 3.12a, b) . Higher RMSE and MAE values can be seen in the transition zones from lower to higher altitudes across the eastern and western slopes of the Andes. For example, high MAE and RMSE values occurred at –79.45° W and –1.15° S and at

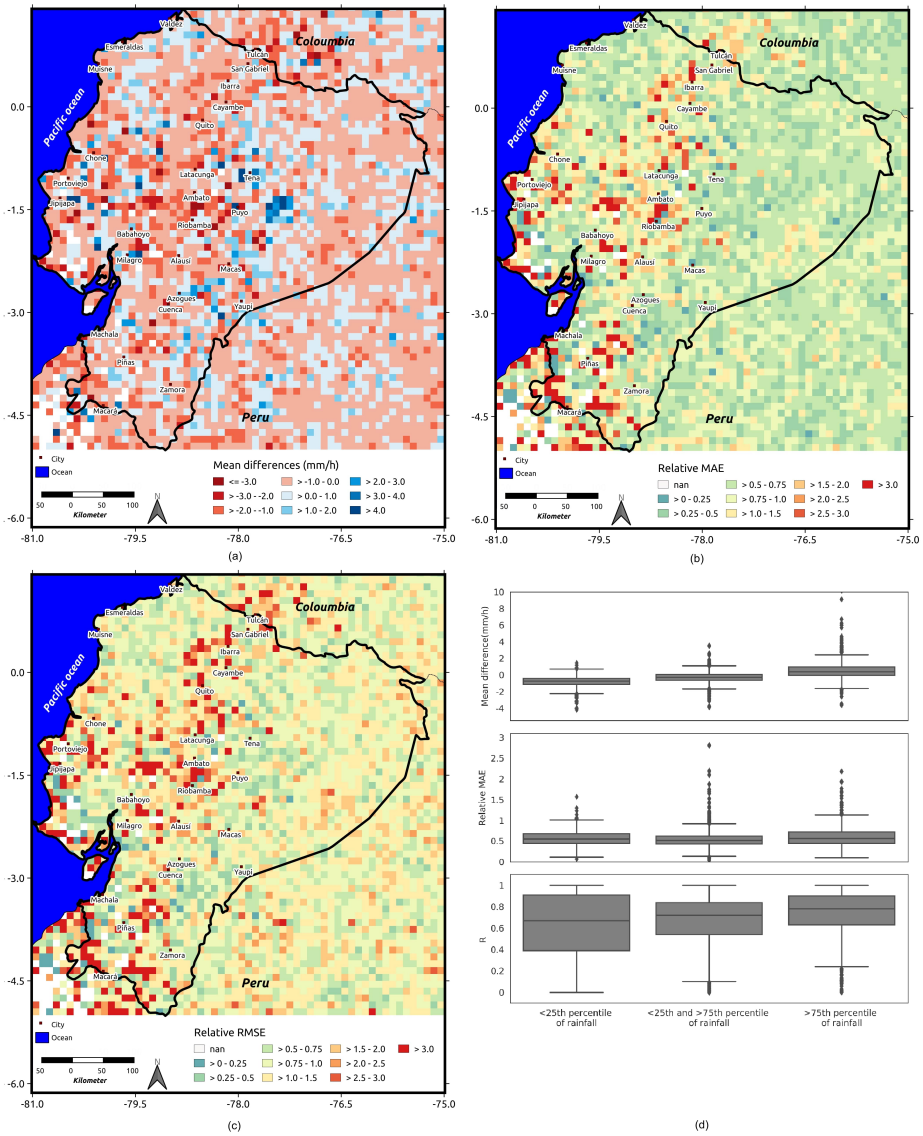

Figure 3.11: Spatial distribution of (a) the mean differences between the MW-based IMERG and the RF-combined model rain rates; (b) the relative MAE; (c) the relative RMSE; (d) the performance of the rainfall retrieval as box plots for low, medium, and high precipitation rates according to percentiles. The boxes display the 25th, 50th, and 75th percentiles. The relative MAE and RMSE were calculated by dividing the MAE and RMSE values in each pixel by the average MW-based IMERG rainfall rate over the training/validation period. Nan is the values in which no data from MW-based IMERG was available.

–77.3° W and 1.36° S. This corresponds to areas with higher mean rainfall rates (Figure 3 a). The R values show a higher spatial variability in the RF-combined

model's performance, and lower R values can be found in some higher elevated areas and along the coast. Generally, the model performance slightly increases with elevation but decreases at very high elevations (Figure 3.12d).

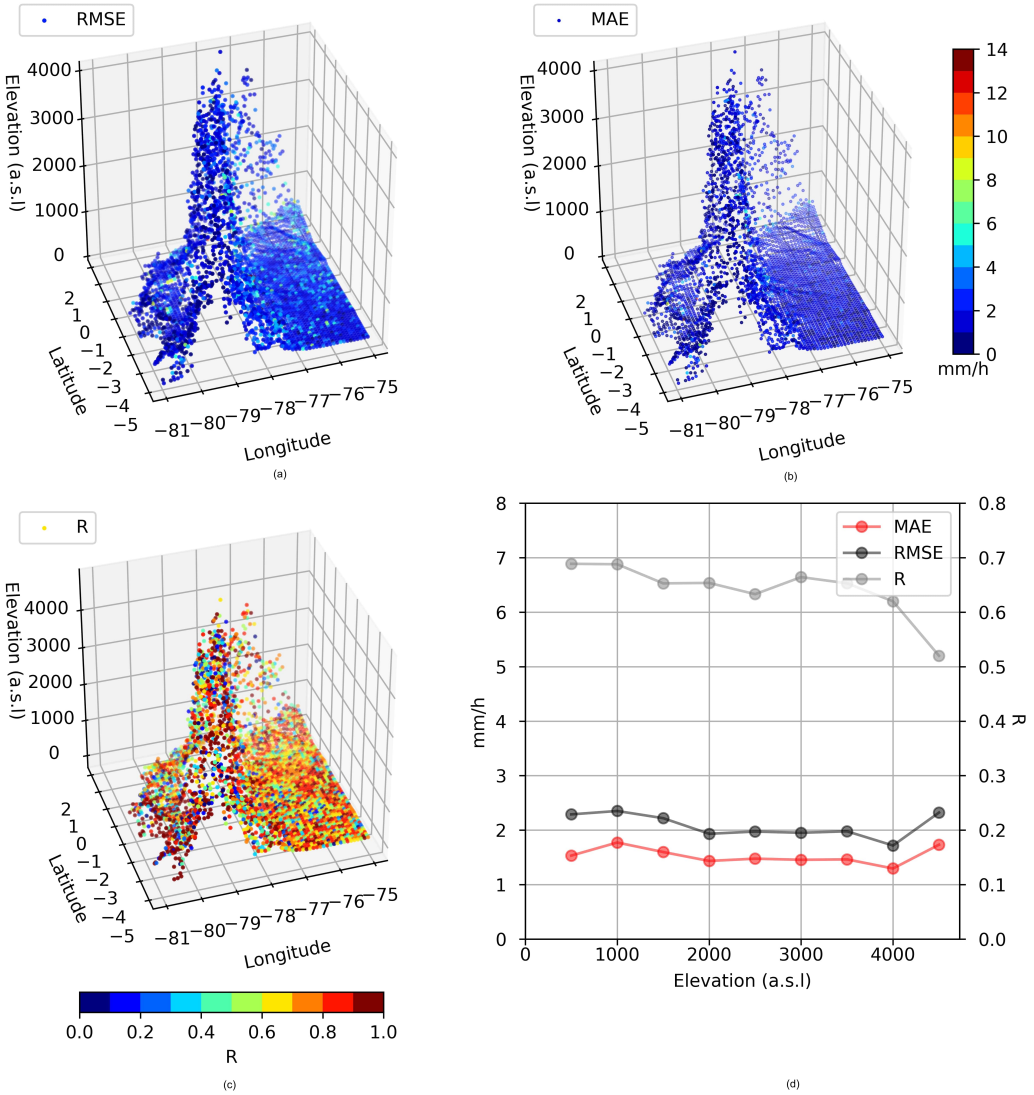

Figure 3.12: The (a) RMSE, (b) MAE, and (c) R in relation to latitude, longitude, and elevation. The (d) RMSE, MAE, and R spatially averaged in relation to elevation over the training/validation period.

3.3.4 The overall performance of the RF rainfall retrieval compared to gauge data

We compared the final product of the RF rainfall retrieval in two different spatial resolutions against independent daily gauge measurements from 1 January to 19 April 2018.

The results for the RF rainfall retrieval in 11 km^2 resolution showed a median HSS of 0.35 for all INAMHI rain gauge stations (Figure 3.13a), while the HSS for the IR-only IMERG product tends toward 0.2. The RF rainfall retrieval shows a better performance in estimating the rainfall rate (Figure 3.13a) with R values around 0.34 (Figure 3.13a).

Figure 3.13 c, d displays the spatial distribution of the HSS and R values for the RF rainfall retrieval in 15 min and 2 km^2 resolution. The worst HSS was related to the transition areas from the Andes to the Amazon rainforest. The highest HSS of 0.5 was obtained for the station near Portoviejo. The R value was also the most substantial for the station near Portoviejo, and was high (0.4– 0.7) in the western/northern parts of Ecuador and the Amazon region. For the northern stations, lower R values were observed. The median R value for all the stations was 0.33, and the best correlation was 0.70. The HSS did not show much variability across the different regions.

3.4 Discussion

The feature selection results for the RF classification and the RF regression indicated that the models identified the close link between topography and rainfall. The feature importance of ancillary geoinformation was relatively high compared to the other predictors and was frequently selected. This shows that elevation plays a vital role in the rainfall model. The selected predictors for both models showed that the models preferred to use two bands in combination, where the dominant texture metric selected in almost all months was the PCV. This was also shown by Egli, Thies, and Bendix [55] and Turini, Thies, and Bendix [34].

The models showed a high R (0.64) with a low RMSE (2.78 mm/h) and a low MAE (1.66 mm/h). The variability of the R per month (Figure 3.8) indicated a connection to the detected rain area (Figure 3.6). Following the rain delineation models' lower performance in July 2017 and October 2017, the RF-combined model's quality was also worse for these months.

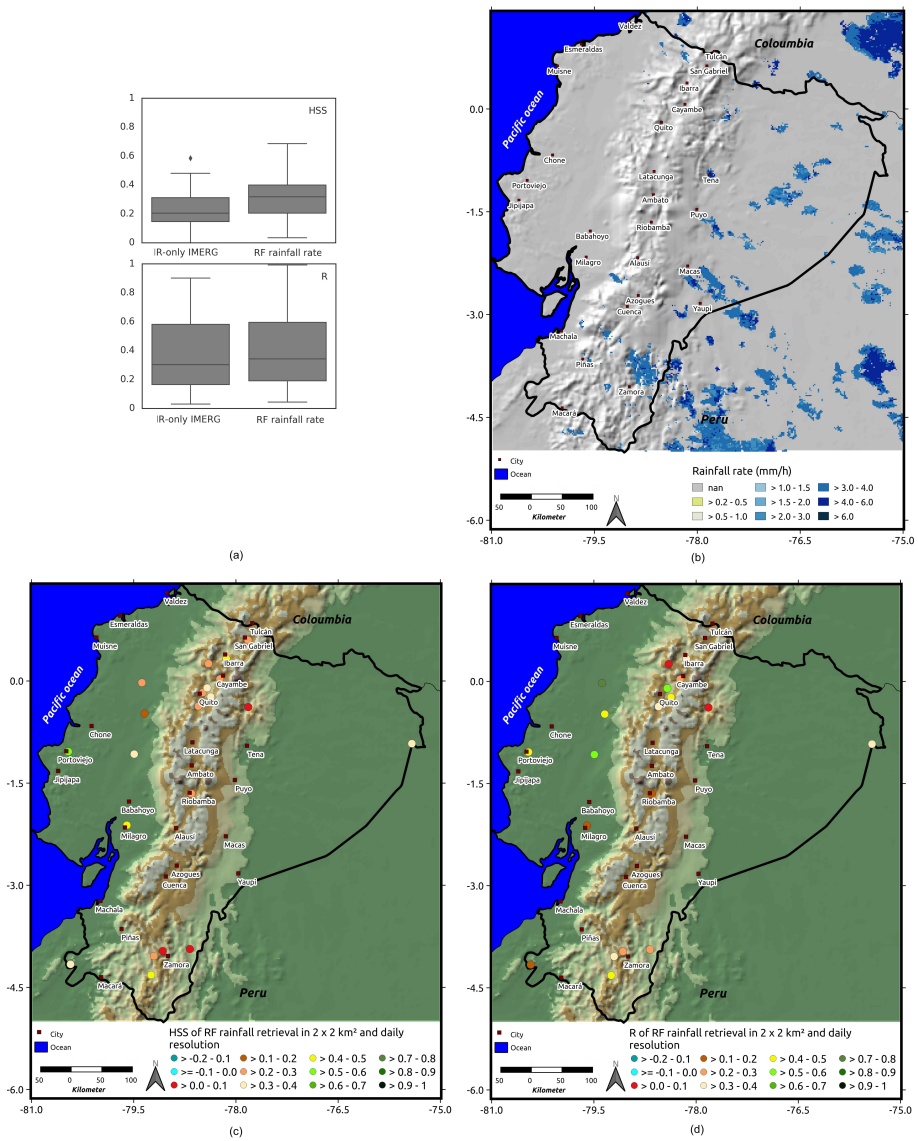

Figure 3.13: (a) Boxplot of the validation measures of HSS and R for the comparison of RF rainfall retrieval and the IR-only IMERG at an 11 km^2 resolution against the INAMHI gauge data. The scores were calculated based on all the available data for the period between 1 January 2018 and 19 April 2018. The boxes display the 25th, 50th, and 75th percentiles. (b) An example of the RF-based rainfall rate for 12 January 2018 at 18:00 UTC at a high spatiotemporal resolution (15 min and 2 km^2). (c) Spatial distribution of the HSS for the RF rainfall retrieval in 2 km^2 and at daily resolution. (d) Spatial distribution of the R for the RF rainfall retrieval in 2 km^2 and at daily resolution.

The verification scores for the rain area delineation showed an improvement in comparison to previous studies. On average, the HSS in our study was 0.6, while in the studies by Kühnlein et al. [31] and Min et al. [39] was between 0.2 and 0.5 and 0.53, respectively. This might be due to our study's feature selection process, but not in the mentioned studies. For Ecuador, the study of Ward et al. [25] revealed POD of 0.36 and FAR of 0.2 for the rain area in the TRMM 3B42 product at a daily timescale and a spatial resolution of 0.25° in a small basin of Paute in Ecuador near Cuenca. In this region, our RF models for the rain area delineation obtained POD between 0.3 and 0.48 and FAR between 0.2 and 0.3 in 15 min and 0.1°. This shows the application of new ML algorithms such as RF could improve MW–IR blending algorithms.

Concerning the rainfall rate assignment, the median R in our study was between 0.5 and 0.62 for half-hourly retrievals, while Kühnlein et al. [31] obtained R between 0.14 and 0.46 for Germany at an hourly resolution. In another study, Kühnlein et al. [32] achieved R between 0.69 and 0.72 on an hourly scale in Germany. Our product had a slightly lower performance than that of Kühnlein et al. [32], which might be due to the more complex topography in Ecuador than Germany. Small-scale regional conventions are common in Ecuador [63], while Germany has large-scale advective systems, particularly in winter, which are easier to detect. Subscale convective rainfall systems due to local topographic conditions [63] are probably not captured by GOES data, while the large-scale advective rainfall systems in Germany are easier to detect.

The validation of the TRMM in Ecuador with interpolated rainfall data from intense gauges revealed a mean R of 0.82 for a monthly spatial resolution of 0.25° [26]. Kühnlein et al. [32] showed that the performance of rainfall products increases by increasing the time interval.

Figure 3.9 indicates that the RF models have problems in predicting high rainfall rates, which was also shown by Kühnlein et al. [32]. Since the applied RF regression model is a very low-order regression model (only the average of the observations over the leaves was used), extreme events were underestimated compared to the training dataset's average values [32]. Therefore, estimating the extreme events useful for flood management, e.g., under El Niño conditions (e.g., Bendix et al. [65] remains a challenge for the proposed RF-based rainfall retrieval.

The RF classification results indicated a relationship to the different climate zones in the study area. In the semi-arid regions in the southwest of Ecuador and the northwest of Peru, the RF models showed lower HSS and POD (Figure 3.10a,b) than

the more rainy regions in the Amazon rainforest. For the RF-combined model, higher MAE and RMSE were found in the semi-arid areas with lower rainfall rates (Figure 3.3 and Figure 3.10). Training separate models for different climate zones might be an approach for further improvement.

The spatial details of the RF models' performance enable us to identify better the error sources and their contributions to different climates. The spatial variability in the RF model performance could also be attributed to the fact that the training and validation pixels were selected randomly in each scene. As a result, the RF models were better able to capture the short-term variability of the rainfall distribution. The more extended training period provided more information from the MW swats in different regions and times [27, 34]. Another reason for the spatial differences in the verification score could be related to the different viewing geometries between the GEO and the polar-orbiting MW systems [27, 34]. These problems introduce some lags in rainfall events that might be problematic for rainfall structure analysis [27]. Furthermore, differences between the MW systems considered in the GPM constellation might be an issue. According to Tan et al. [62], MW sensors' different properties could lead to different rainfall rates for the same rainfall event, even when the same retrieval scheme is applied.

The results confirmed the rainfall estimation limitations of satellites across regions with a complex topography (Figure 3.10d and Figure 3.11d). In Ecuador, high-elevation areas and volcanoes are covered by ice, which is erroneous in the MW-based IMERG [66]; this is a surface-screening problem. The snow and ice on the ground weaken the upwelling microwave signal, erroneously considered the PMW retrieval's rainfall [67].

Compared to the RF-only IMERG, the RF models showed distinct improvements in rain area delineation (Figure 3.7) and rainfall rate assignment (Figure 3.8). This is in agreement with the results of Kolbe et al. [29, 30] and Turini, Thies, and Bendix [34]. Also, we compared our product with INAMHI gauge measurements. The RF-based rainfall retrieval performed better on the 11 km^2 and 15 min scale than the IR-only IMERG (Figure 3.11a). This illustrates the higher potential of using multispectral GEO data rather than only one IR channel rainfall retrieval, as is done in the IMERG.

We found an R of 0.33 and a HSS of 0.27 for the RF-based rainfall retrieval (2 km^2, 15 min). Zubieta et al. [68] examined TRMM-based products' performance (TMPA V7 and TMPA RT) and the IMERG-V03 with a spatial resolution of 0.25° and 0.1°, respectively, in the Peruvian–Ecuadorian Amazon basin. In this study, the daily HSS

varied from 0 to 0.2 in the Andean region. Our RF-based rainfall retrieval showed HSS values from 0.05 to 0.5 for the same areas at a 2 km^2 and 15 min resolution.

The evaluation results for the IMERG and TMPA obtained by Manz et al. [23] at a daily scale and 0.25° revealed higher R in regions with higher precipitation, confirming our results. In the same study, the IMERG-V05 (R of 0.2 to 0.5) showed a better R than the TMPA product (R of 0.2), which still confirms the better performance of our RF-based rainfall retrieval (R of 0.33).

It must be noted that the evaluation of satellite-based precipitation products using a few gauges has uncertainties. One reason is the different measurements and viewing geometry. Another issue is the point observations from a scarce gauge network that cannot represent the spatial rainfall distribution. In regions with substantial precipitation variability at the local scale, such as in Ecuador, this is more relevant for validating satellite-based rainfall products [69]. Another point is the daily temporal aggregation of our satellite-based rainfall product. Due to the scan cycle, some rain events might not be captured by our retrieval method. More rain gauges with a higher temporal resolution and a ground-based radar network would be ideal for a more realistic validation.

3.5 Conclusion

The validation showed that the RF models could retrieve good rainfall information over Ecuador with higher accuracy than the IR-only IMERG. This illustrates the viability of our approach and the benefit of using multispectral IR data. Meanwhile, the spatial variability of the evaluation illustrates the influence of different climate zones and topography in Ecuador, which should be investigated in more detail in future studies.

High precipitation values were underestimated by the proposed algorithm, as mentioned earlier, due to RF regression problems with extreme values. This is an important issue for future research. We need more training datasets with extreme events; therefore, the ML algorithm can differentiate between heavy and light rain. A two-step classification approach could be used for defining extreme rainfall events. The first step delineates rainy and non-rainy areas. In the second step, the rainfall area is divided into “non-extreme rainfall events” and “extreme rainfall events.” A regionally defined threshold could separate non-extreme rainfall events and extreme rainfall events based on rainfall amounts. After classification, the RF regression

models could be trained and applied separately for different classes. Another possibility could be using other ML techniques such as neural networks or extreme learning machine algorithms [70].

This study was limited to the available microwave-only data of the IMERG. Therefore, some rainfall events might not have been recorded due to the overflight of the microwave satellite in Ecuador, which introduces uncertainty in our model's training.

The RF-based rainfall retrieval showed medium performance against daily-scale ground-based rainfall measurements. To obtain ideas for further improvement of the algorithm, we are currently investigating the error structure in more detail using high-resolution gauge and weather radar data.

3.A Appendix A

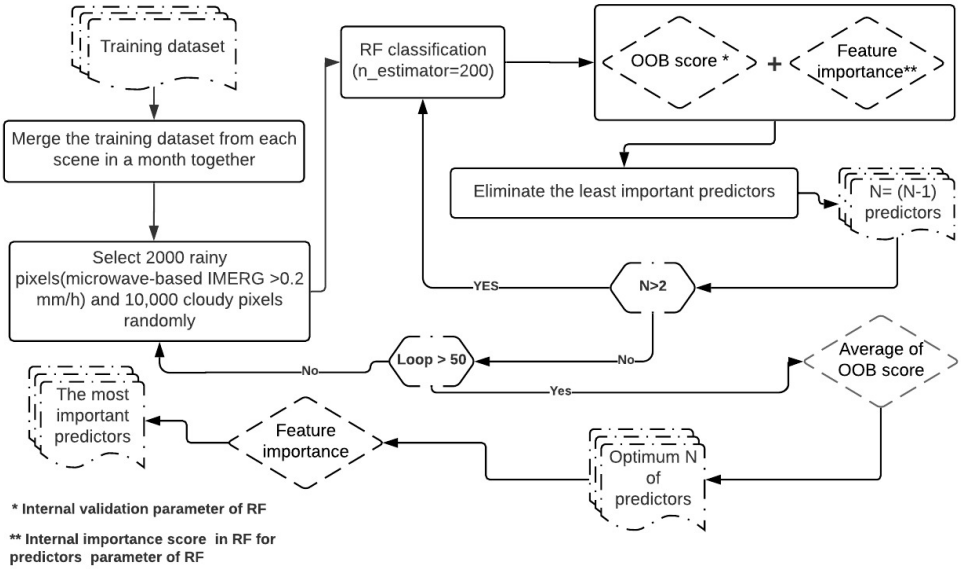

Figure 3.A.1: The architecture of recursive feature elimination for selecting the most important predictors in RF classification.

Table 3.A.1: List of the different sub-datasets in the IMERG-V06 product (half-hourly data final run) and definitions used in this study

Sub-dataset	Definitions
precipitationCal	Multi-satellite precipitation estimate with gauge calibration
HQobservationTime	Microwave satellite observation time
IRprecipitation	IR-only precipitation estimate
PrecipitationQualityIndex	Quality Index for precipitationCal field

Table 3.A.2: Median HSS scores for the random forest (RF) classification with different class ratios and applying "`class_weight = balanced"` in RF over the training/validation period in Ecuador

Model name	**Ratio between non-rainy (majority class) and rainy (minority class) pixels**	**HSS**	**POD**	**FAR**
Scenario-0	1:1	0.41	0.87	0.63
Scenario-1	2:1	0.53	0.77	0.54
Scenario-2	3:1	0.57	0.70	0.40
Scenario-3	4:1	0.58	0.65	0.35
Scenario-4	5:1	0.6	0.62	0.31

Table 3.A.3: Median HSS and R for the RF classification (ratio of 1:5) and the RF regression with and without applying the class_weight function in the RF model

Median HSS with a 1:5 ratio distribution for the training/validation period		**Median R with for training/validation period**	
Including class weight balance	**Without class weight balance**	**Including class weight balance**	**Without class weight balance**
0.6	0.58	0.64	0.6

Table 3.A.4: Validation metrics with equations, theoretical ranges, and optimum values, TP, true positive; FN, false negative; FP, false positive; TN, true negative; P rainfall from RF regression; O microwave-based IMERG rainfall; n, number of pixels considered in the validation.

Name	**Metrics equation**	**Range**	**Optimum**	**Validation**
Probability of detection	POD=$\frac{H}{H-M}$	[0,1]	1	Spatial temporal
False alarm ratio	FAR=$\frac{F}{F-C}$	[0,1]	0	Spatial temporal
Heidke skill score	HSS=$\frac{2(H\times C-F\times M)}{(H-M)(M+C)+(H+F)(F+C)}$	[0,1]	1	Spatial temporal
Mean absolute error	MAE=$\frac{1}{n}\sum_{i=1}^{n}\lvert P_i-O_i\rvert$	-	-	Spatial temporal
Root mean square error	RMSE=$\sqrt{\frac{\sum_{i=1}^{n}(P_i-O_i)^2}{n}}$	-	-	Spatial temporal
Correlation coefficient	$R=\frac{(n\sum_{i=1}^{n}(P_iO_i-(\sum_{i=1}^{n}P_i)(\sum_{i=1}^{n}O_i))}{\sqrt{((n\sum_{i=1}^{n}(P_i^2)-(\sum_{i=1}^{n}(P_i))^2)((n\sum_{i=1}^{n}O_i^2)-(\sum_{i=1}^{n}O_i)^2)}}$	[-1,1]	1	Spatial temporal
Mean differences	Average (microwave-based IMERG minus RF-combined model)			Spatial

References

[1] Jochen Seidel et al. "Precipitation Characteristics at Two Locations in the Tropical Andes by Means of Vertically Pointing Micro-Rain Radar Observations". In: *Remote Sensing* 11.24 (2019). ISSN: 2072-4292. DOI: 10.3390/rs11242985. URL: https://www.mdpi.com/2072-4292/11/24/2985.

[2] Wouter Buytaert et al. "Spatial and temporal rainfall variability in mountainous areas: A case study from the south Ecuadorian Andes". In: *Journal of hydrology* 329.3-4 (2006), pp. 413–421.

[3] Boris F Ochoa-Tocachi et al. "Impacts of land use on the hydrological response of tropical Andean catchments". In: *Hydrological Processes* 30.22 (2016), pp. 4074–4089.

[4] Rütger Rollenbeck and Jörg Bendix. "Rainfall distribution in the Andes of southern Ecuador derived from blending weather radar data and meteorological field observations". In: *Atmospheric Research* 99.2 (2011), pp. 277–289. ISSN: 0169-8095. DOI: https://doi.org/10.1016/j.atmosres.2010.10.018. URL: https://www.sciencedirect.com/science/article/pii/S0169809510002826.

[5] Robert J Joyce et al. *CMORPH: A Method that Produces Global Precipitation Estimates from Passive Microwave and Infrared Data at High Spatial and Temporal Resolution*. 2004.

[6] Ali Behrangi et al. *PERSIANN-MSA: A Precipitation Estimation Method from Satellite-Based Multispectral Analysis*. 2009.

[7] Yang Hong et al. "Precipitation estimation from remotely sensed imagery using an artificial neural network cloud classification system". In: *Journal of Applied Meteorology* 43.12 (2004), pp. 1834–1853.

[8] George J Huffman et al. *The TRMM Multisatellite Precipitation Analysis (TMPA): Quasi-Global, Multiyear, Combined-Sensor Precipitation Estimates at Fine Scales*. 2007.

[9] Robert F. Adler et al. "Estimation of Monthly Rainfall over Japan and Surrounding Waters from a Combination of Low-Orbit Microwave and Geosynchronous IR Data". In: *Journal of Applied Meteorology and Climatology* 32.2 (1993), pp. 335–356. DOI: 10.1175/1520-0450(1993)032<0335:EOMROJ>

2.0.CO;2. URL: https://journals.ametsoc.org/view/journals/apme/32/2/1520-0450_1993_032_0335_eomroj_2_0_co_2.xml.

[10] Christian Kummerow and Louis Giglio. "A method for combining passive microwave and infrared rainfall observations". In: *Journal of Atmospheric and Oceanic Technology* 12.1 (1995), pp. 33–45.

[11] Liming Xu et al. "A Microwave Infrared Threshold Technique to Improve the GOES Precipitation Index". In: *Journal of Applied Meteorology* 38.5 (1999), pp. 569–579. DOI: 10.1175/1520-0450(1999)038<0569:AMITTT>2.0.CO;2. URL: https://journals.ametsoc.org/view/journals/apme/38/5/1520-0450_1999_038_0569_amittt_2.0.co_2.xml.

[12] Chris Kidd et al. "Satellite rainfall estimation using combined passive microwave and infrared algorithms". In: *Journal of Hydrometeorology* 4.6 (2003), pp. 1088–1104.

[13] V Levizzani, P Bauer, and F Joseph Turk. *Measuring Precipitation from Space: EURAINSAT and the Future*. en. Springer Science & Business Media, May 2007.

[14] Martin C Todd et al. "A combined satellite infrared and passive microwave technique for estimation of small-scale rainfall". In: *Journal of Atmospheric and Oceanic Technology* 18.5 (2001), pp. 742–755.

[15] Robert J. Kuligowski. "A Self-Calibrating Real-Time GOES Rainfall Algorithm for Short-Term Rainfall Estimates". In: *Journal of Hydrometeorology* 3.2 (2002), pp. 112–130. DOI: 10.1175/1525-7541(2002)003<0112:ASCRTG>2.0.CO;2. URL: https://journals.ametsoc.org/view/journals/hydr/3/2/1525-7541_2002_003_0112_ascrtg_2_0_co_2.xml.

[16] David W. Martin et al. "Estimates of daily rainfall over the Amazon Basin". In: 95.D10 (Sept. 1990), pp. 17, 043–17, 050. DOI: 10.1029/JD095iD10p17043.

[17] S. W. Miller, P. A. Arkin, and R. Joyce. "A combined microwave/infrared rain rate algorithm". In: *International Journal of Remote Sensing* 22.17 (2001), pp. 3285–3307. DOI: 10.1080/01431160152609155. eprint: https://doi.org/10.1080/01431160152609155. URL: https://doi.org/10.1080/01431160152609155.

[18] Gilberto A Vicente, Roderick A Scofield, and W Paul Menzel. "The operational GOES infrared rainfall estimation technique". In: *Bulletin of the American Meteorological Society* 79.9 (1998), pp. 1883–1898.

[19] George J Huffman et al. "NASA global precipitation measurement (GPM) integrated multi-satellite retrievals for GPM (IMERG)". In: *Algorithm theoretical basis document, version* 4 (2015), p. 30.

[20] Fengrui Chen and Xi Li. "Evaluation of IMERG and TRMM 3B43 monthly precipitation products over mainland China". In: *Remote Sensing* 8.6 (2016), p. 472.

[21] Hao Guo et al. "Early assessment of integrated multi-satellite retrievals for global precipitation measurement over China". In: *Atmospheric Research* 176 (2016), pp. 121–133.

[22] Na Li et al. "Statistical assessment and hydrological utility of the latest multi-satellite precipitation analysis IMERG in Ganjiang River basin". In: *Atmospheric research* 183 (2017), pp. 212–223.

[23] Bastian Manz et al. "Comparative ground validation of IMERG and TMPA at variable spatiotemporal scales in the tropical Andes". In: *Journal of Hydrometeorology* 18.9 (2017), pp. 2469–2489.

[24] Satya Prakash et al. "From TRMM to GPM: How well can heavy rainfall be detected from space?" In: *Advances in Water Resources* 88 (2016), pp. 1–7. ISSN: 0309-1708. DOI: https://doi.org/10.1016/j.advwatres.2015.11.008. URL: https://www.sciencedirect.com/science/article/pii/S0309170815002675.

[25] E Ward et al. "Evaluation of precipitation products over complex mountainous terrain: A water resources perspective". In: *Advances in Water Resources* 34.10 (2011), pp. 1222–1231.

[26] Bolívar Erazo et al. "Validation of Satellite Estimates (Tropical Rainfall Measuring Mission, TRMM) for Rainfall Variability over the Pacific Slope and Coast of Ecuador". In: *Water* 10.2 (2018). ISSN: 2073-4441. DOI: 10.3390/w10020213. URL: https://www.mdpi.com/2073-4441/10/2/213.

[27] Ali Behrangi et al. "REFAME: Rain Estimation Using Forward-Adjusted Advection of Microwave Estimates". In: *Journal of Hydrometeorology* 11.6 (2010), pp. 1305–1321. DOI: 10.1175/2010JHM1248.1. URL: https://journals.ametsoc.org/view/journals/hydr/11/6/2010jhm1248_1.xml.

[28] Apostolos Giannakos and Haralambos Feidas. "Classification of convective and stratiform rain based on the spectral and textural features of Meteosat Second Generation infrared data". en. In: *Theor. Appl. Climatol.* 113.3-4 (Aug. 2013), pp. 495–510.

[29] Christine Kolbe et al. "Precipitation Retrieval over the Tibetan Plateau from the Geostationary Orbit—Part 1: Precipitation Area Delineation with Elektro-L2 and Insat-3D". In: *Remote Sensing* 11.19 (2019). ISSN: 2072-4292. DOI: 10.3390/rs11192302. URL: https://www.mdpi.com/2072-4292/11/19/2302.

[30] Christine Kolbe et al. "Correction: Kolbe, C., et al. Precipitation Retrieval over the Tibetan Plateau from the Geostationary Orbit—Part 2: Precipitation Rates with Elektro-L2 and Insat-3D. Remote Sensing 2020, 12, 2114". In: *Remote Sensing* 12.21 (2020). ISSN: 2072-4292. DOI: 10.3390/rs12213594. URL: https://www.mdpi.com/2072-4292/12/21/3594.

[31] Meike Kühnlein et al. "Precipitation Estimates from MSG SEVIRI Daytime, Nighttime, and Twilight Data with Random Forests". In: *J. Appl. Meteorol. Climatol.* 53.11 (Nov. 2014), pp. 2457–2480.

[32] Meike Kühnlein et al. "Improving the accuracy of rainfall rates from optical satellite sensors with machine learning—A random forests-based approach applied to MSG SEVIRI". In: *Remote Sens. Environ.* 141 (2014), pp. 129–143.

[33] Hanna Meyer, Johannes Drönner, and Thomas Nauss. *Satellite based high resolution mapping of rainfall over Southern Africa.* 2017.

[34] Nazli Turini, Boris Thies, and Joerg Bendix. "Estimating High Spatio-Temporal Resolution Rainfall from MSG1 and GPM IMERG Based on Machine Learning: Case Study of Iran". In: *Remote Sensing* 11.19 (2019). ISSN: 2072-4292. DOI: 10.3390/rs11192307. URL: https://www.mdpi.com/2072-4292/11/19/2307.

[35] John T. Abatzoglou, Kelly T. Redmond, and Laura M. Edwards. "Classification of Regional Climate Variability in the State of California". In: *Journal of Applied Meteorology and Climatology* 48.8 (2009), pp. 1527–1541. DOI: 10.1175/2009JAMC2062.1. URL: https://journals.ametsoc.org/view/journals/apme/48/8/2009jamc2062.1.xml.

[36] Yagmur Derin et al. "Multiregional satellite precipitation products evaluation over complex terrain". In: *Journal of Hydrometeorology* 17.6 (2016), pp. 1817–1836.

[37] Frédéric Satgé et al. "Assessment of satellite rainfall products over the Andean plateau". In: *Atmospheric Research* 167 (2016), pp. 1–14.

[38] D Capacci and BJ Conway. "Delineation of precipitation areas from MODIS visible and infrared imagery with artificial neural networks". In: *Meteorological Applications* 12.4 (2005), pp. 291–305.

[39] M Min et al. "Estimating Summertime Precipitation from Himawari-8 and Global Forecast System Based on Machine Learning". In: *IEEE Trans. Geosci. Remote Sens.* 57.5 (May 2019), pp. 2557–2570.

[40] Hanna Meyer et al. "Comparison of four machine learning algorithms for their applicability in satellite-based optical rainfall retrievals". In: *Atmospheric research* 169 (2016), pp. 424–433.

[41] Leo Breiman. "Random Forests". In: *Mach. Learn.* 45.1 (Oct. 2001), pp. 5–32.

[42] F Pedregosa et al. "Scikit-learn: Machine Learning in Python". In: *J. Mach. Learn. Res.* 12 (2011), pp. 2825–2830.

[43] Andrew Heidinger. *Algorithm theoretical basis document: ABI cloud mask*. University of Wisconsin–Madison, 2011.

[44] GDAL/OGR contributors. *GDAL/OGR Geospatial Data Abstraction software Library*. Open Source Geospatial Foundation. 2020. URL: https://gdal.org.

[45] George J Huffman et al. "NASA Global Precipitation Measurement (GPM) Integrated Multi-satellitE Retrievals for GPM (IMERG). Algorithm Theoretical Basis Document, Version 06". In: *Algorithm Theoretical Basis Document (ATBD) Version* 4 (2019), p. 26.

[46] Arthur Y Hou et al. "The global precipitation measurement mission". In: *Bulletin of the American Meteorological Society* 95.5 (2014), pp. 701–722.

[47] Steven J Goodman. "GOES-R series introduction". In: *The GOES-R Series*. Elsevier, 2020, pp. 1–3.

[48] Timothy J Schmit et al. "A closer look at the ABI on the GOES-R series". In: *Bulletin of the American Meteorological Society* 98.4 (2017), pp. 681–698.

[49] T Inoue. "On the temperature measurements and effective cirrus emissivity clouds by window determination region of semi-transparent in the". In: *J. Meteorol. Soc. Jpn* 63 (1985), pp. 88–99.

[50] Itamar M Lensky and Daniel Rosenfeld. "A night-rain delineation algorithm for infrared satellite data based on microphysical considerations". In: *Journal of Applied Meteorology* 42.9 (2003), pp. 1218–1226.

[51] SC Ou et al. "Remote sensing of cirrus cloud parameters using advanced very-high-resolution radiometer 3.7-and 10.9-μm channels". In: *Applied Optics* 32.12 (1993), pp. 2171–2180.

[52] Robert S Stone et al. "The remote sensing of thin cirrus cloud using satellites, lidar and radiative transfer theory". In: *Journal of Applied Meteorology and Climatology* 29.5 (1990), pp. 353–366.

[53] Kathleen I Strabala, Steven A Ackerman, and W Paul Menzel. "Cloud Properties inferred from 8 12-μm Data". In: *Journal of Applied Meteorology and Climatology* 33.2 (1994), pp. 212–229.

[54] B Thies, T Nauss, and J Bendix. *First results on a process-oriented rain area classification technique using Meteosat Second Generation SEVIRI nighttime data*. 2008.

[55] Sebastian Egli, Boris Thies, and Jörg Bendix. "A Hybrid Approach for Fog Retrieval Based on a Combination of Satellite and Ground Truth Data". en. In: *Remote Sensing* 10.4 (Apr. 2018), p. 628.

[56] Martin G. Schultz et al. "Tropospheric Ozone Assessment Report: Database and metrics data of global surface ozone observations". In: *Elementa* 5 (2017). ISSN: 23251026. DOI: 10.1525/elementa.244.

[57] T Dinku et al. "Validation of high-resolution satellite rainfall products over complex terrain". In: *International Journal of Remote Sensing* 29.14 (2008), pp. 4097–4110.

[58] T Dinku et al. "Validation of satellite rainfall products over East Africa's complex topography". In: *International Journal of Remote Sensing* 28.7 (2007), pp. 1503–1526.

[59] ORNL DAAC. *Spatial Data Access Tool (SDAT)*. 2017.

[60] M Neteler et al. *GRASS GIS: A multi-purpose Open Source GIS. Environmental Modeling and Software (31): 124–130*. 2012.

[61] Olaf Conrad et al. "System for automated geoscientific analyses (SAGA) v. 2.1. 4". In: *Geoscientific Model Development* 8.7 (2015), pp. 1991–2007.

[62] Jackson Tan et al. "Diurnal cycle of IMERG V06 precipitation". In: *Geophysical Research Letters* 46.22 (2019), pp. 13584–13592.

[63] Jörg Bendix et al. "Formation of convective clouds at the foothills of the tropical eastern Andes (South Ecuador)". In: *Journal of Applied Meteorology and Climatology* 48.8 (2009), pp. 1682–1695.

[64] John D Hunter. "Matplotlib: A 2D graphics environment". In: *Computing in science & engineering* 9.03 (2007), pp. 90–95.

[65] Jörg Bendix et al. "RadarNet-Sur first weather radar network in tropical high mountains". In: *Bulletin of the American Meteorological Society* 98.6 (2017), pp. 1235–1254.

[66] George Huffman. *IMERG V06 quality index*. 2019.

[67] Veljko Petković and Christian D. Kummerow. "Understanding the Sources of Satellite Passive Microwave Rainfall Retrieval Systematic Errors Over Land". In: *Journal of Applied Meteorology and Climatology* 56.3 (2017), pp. 597–614. DOI: 10.1175/JAMC-D-16-0174.1. URL: https://journals.ametsoc.org/view/journals/apme/56/3/jamc-d-16-0174.1.xml.

[68] Ricardo Zubieta et al. "Hydrological modeling of the Peruvian–Ecuadorian Amazon Basin using GPM-IMERG satellite-based precipitation dataset". In: *Hydrology and Earth System Sciences* 21.7 (2017), pp. 3543–3555.

[69] Guoqiang Tang et al. "Accounting for spatiotemporal errors of gauges: A critical step to evaluate gridded precipitation products". In: *Journal of hydrology* 559 (2018), pp. 294–306.

[70] Ravinesh C Deo and Mehmet Şahin. "Application of the extreme learning machine algorithm for the prediction of monthly Effective Drought Index in eastern Australia". In: *Atmospheric Research* 153 (2015), pp. 512–525.

Chapter 4

Assessment of Satellite-Based Rainfall Products Using a X-Band Rain Radar Network in the Complex Terrain of the Ecuadorian Andes

Nazli Turini [1,*], Boris Thies [1], Rütger Rollenbeck [1], Andreas Fries [2], Franz Pucha-Cofrep [3], Johanna Orellana-Alvear [1,4], Natalia Horna [5] and Jörg Bendix [1]

[1] Laboratory for Climatology and Remote Sensing, Faculty of Geography, Philipps-Universität Marburg, 35037 Marburg, Germany

[2] Unidad Ingeniería Civil y Geología (UCG), Hidrología y Climatología Working Group, Universidad Técnica Particular de Loja, Loja, 1101608, Ecuador

[3] Institute for Environmental Sciences, Brandenburg University of Technology (BTU) Cottbus-Senftenberg, Burger Chaussee 2, 03044 Cottbus, Germany

[4] Departamento de Recursos Hídricos y Ciencias Ambientales, Universidad de Cuenca, Cuenca EC010207, Ecuador

[5] Department of Geography and Environmental Management, University of Waterloo, Waterloo, ON N2L 3G1, Canada

---

This chapter is printed in ***Atmosphere, 12(12), 1678***, DOI: https://doi.org/10.3390/atmos12121678

Abstract

Ground based rainfall information is hardly available in most high mountain areas of the world due to the remoteness and complex topography. Thus, proper understanding of spatio-temporal rainfall dynamics still remains a challenge in those areas. Satellite-based rainfall products may help if their rainfall assessment are of high quality. In this paper, microwave-based integrated multi-satellite retrieval for the Global Precipitation Measurement (GPM) (IMERG) (MW-based IMERG) was assessed along with the random-forest-based rainfall (RF-based rainfall) and infrared-only IMERG (IR-only IMERG) products against the quality-controlled rain radar network and meteorological stations of high temporal resolution over the Pacific coast and the Andes of Ecuador. The rain area delineation and rain estimation of each product were evaluated at a spatial resolution of 11 km^2 and at the time of MW overpass from IMERG. The regionally calibrated RF-based rainfall at 2 km^2 and 30 min was also investigated. The validation results indicate different essential aspects: (i) the best performance is provided by MW-based IMERG in the region at the time of MW overpass; (ii) RF-based rainfall shows better accuracy rather than the IR-only IMERG rainfall product. This confirms that applying multispectral IR data in retrieval can improve the estimation of rainfall compared with single-spectrum IR retrieval algorithms. (iii) All of the products are prone to low-intensity false alarms. (iv) The downscaling of higher-resolution products leads to lower product performance, despite regional calibration. The results show that more caution is needed when developing new algorithms for satellite-based, high-spatiotemporal-resolution rainfall products. The radar data validation shows better performance than meteorological stations because gauge data cannot correctly represent spatial rainfall in complex topography under convective rainfall environments.

Keywords: complex terrain; Ecuador; GPM IMERG; rainfall; radar network; satellite retrieval

4.1 Introduction

Understanding precipitation amounts and patterns is essential for sustainable water management and monitoring the hydrological cycle [1]. In complex mountainous regions characterized by high spatiotemporal variability, coarse networks of operational precipitation gauge stations are often lacking. The spatiotemporal variability, combined with lack of gauge data, makes the time series and area-averaged rainfall analysis more complicated in these regions [2]. This also applies to the complex topography of the Andes in Ecuador.

Early satellite-based rainfall retrieval efforts estimated rainfall from geostationary infrared (IR) data , using the indirect relationship between precipitation rate and the temperature of cloud on top [3]. Hence, the algorithms and the product accuracy were limited to the top of the cloud's characteristics. Unlike IR, microwave (MW) sensors measure thermal radiance from actual precipitation particles in the clouds; consequently, MW retrieval generally provides superior precipitation information [4].

A recent result of the continuous technological improvement of low-Earth-orbiting passive MW satellites and spaceborne radars in the MW band is the Global Precipitation Measurement (GPM) mission [5]. GPM was launched in 2014 as post Tropical Rainfall Measuring Mission (TRMM) [6]. Compared with TRMM, the GPM improved sensitivity to light precipitation and distribution of rain and snow. These improvements have achieved by a two-frequencies precipitation radar (Ku band (13.6 GHz) and Ka-band (35.5 GHz)) as well as the GPM multi-channel microwave imager (GMI) that accommodates higher spectral resolution at frequencies of 10.65, 18.7, 23.8, 26.5, 89, 165.5, and 183.3 GHz [5, 7, 8].

However, several studies showed that machine learning could improved the regionally calibrated retrievals using simply passive IR data from geostationary orbit (GEO) [3, 8, 9, 10, 11, 12, 13]. Compared to the passive MW and radar sensors, the GEO systems provide the high temporal (10–30 min) and spatial (2–4 km^2) resolution. It is essential to capture the short-term characteristics of rainfall systems in the retrieval [8]

A few studies have investigated the performance of satellite-based rainfall products over Ecuadorian areas. The Precipitation Estimation from Remotely Sensed Information using Artificial Neural Networks (PERSIANN) [14] shows low agreement with rain gauge in daily resolution [2] in rain area detection. Manz et al. [15] investigated the performance of the integrated multi-satellite retrievals for GPM (IMERG) [5] and TRMM multi-satellite precipitation analysis (TMPA) [6] against gauge data with different temporal resolutions (hourly, 3 h, and daily). In their study, IMERG showed better agreement than TMPA, especially on the high elevation of Andes. Erazo et al. [16] reported that at high elevations in the Andes, TRMM 3B43 Version 7 retrievals showed a higher correlation ($R^2 = 0.82$) on monthly compared with interpolated gauge data at a spatial resolution of 27.75 km^2. The result of the validation of the regionally developed algorithm in Ecuador, the random forest-based rainfall (RF-based rainfall) of Turini et al. [3] with an 11 km^2 resolution, obtained a median Heike skill score (HSS) around 0.35 for daily gauge stations, meanwhile the

lower performance of the IR-only from the IMERG (IR-only IMERG) showed by HSS = 0.2. In their method, they used the Random forest algorithm to retrieve rainfall. In this text, the RF-based rainfall stands for the rainfall retrieval from random forest algorithm [3]. The RF-based rainfall retrieval performed in estimating the rainfall rate with correlation coefficient (r) values 0.34 [3].

To improve satellite-based products' overall performance, understanding the sources of error on the highest possible temporal resolution is crucial [6, 17]. Given the high spatiotemporal variability of rainfall in Ecuador, spatiotemporally high-resolution validation sources for rainfall are lacking. Therefore, as stated before, only a couple of studies have investigated the performance of satellite-based rainfall products at higher spatiotemporal resolution [15, 18].

Different studies have found that, due to the variability of weather and climate in complex terrain, the satellite retrievals are posed to challenges both in IR and MW [3, 8, 12, 13, 19]. Dinku et al. [19] evaluated the impact of topography on IR-based Tropical Applications of Meteorology using Satellite and ground-based observation (TAMSAT) [20] in East Africa for 1998–2012, comprising five different countries: Uganda, Kenya, Tanzania, Rwanda, and Burundi. In the study, the elevation varied between 1500 and 4500 m [19]. TAMSAT showed an underestimation. Dinku et al. [19] argued that the underestimation corresponded mainly to convective and orographic rainfall during the rainy season (March, April, and May), mostly in the windward exposition.

In this work, we aimed to validate different satellite-based rainfall products to identify and understand sources of errors in the complex elevation of the Andes in Ecuador on a sub-daily time scale. Our aim was not just to compare satellite-based rainfall products with ground measurements but also to identify the sources of the differences between the satellite-based rainfall products and ground measurements. Therefore, in this study, we evaluated the performance of MW-based IMERG in comparison with RF-based rainfall and IR-only IMERG against high-spatiotemporal-resolution data from ground based radar network and high temporal resolution of meteorological stations to characterize the impact of climatic and topographic conditions on satellite-based rainfall products at the time of MW overpass. We also assessed the performance of regionally trained RF-based rainfall in Ecuador on the subdaily time scale (30 min) and high spatial resolution (2 km^2) with the aim of finding the source of possible errors for further development.

Following a description of the climatology of the study area, the satellite-based

rainfall products, ground based radar data and meteorological stations are described in Section 4.2.1. Section 4.2.2 introduces the evaluation methodology with a focus on rain area detection and rain estimation. The results are presented in Section 4.3 and discussed in Section 4.4. Finally, the important findings are summarized in Section 4.5.

4.2 Materials and Methods

4.2.1 Data

4.2.1.1 Radar

In the current study, the data from two rainfall radars, which are part of the Radarnet-Sur network in Southern Ecuador, were used. The westernmost radar system is located on Cerro Guachaurco (3100 m above sea level (m.a.s.l) (GUAXX radar)). Another radar system is located at 4450 (m.a.s.l) (to the best of our knowledge, this is the highest worldwide) on the Paragüillas peak on the north border of the Cajas National Park in Southern Ecuador (CAXX radar). The radars have a maximum range of 100 km^2 and provide images with spatial resolutions of 500 m every 5 min. For more information about the Radarnet-Sur network (Figure 4.1a) infrastructure, please refer to Bendix et al. [21]. The coverage of radars in this study is shown in 4.1a.

Radarnet-Sur calibration strategies have been continuously developed since 2006. The calibration strategy is based on a statistical procedure that uses the available rain gauge data. The data processing and correction algorithms in this empirical calibration consisted of four steps: (i) clutter and noise removal; (ii) atmospheric and geometric attenuation correction; (iii) interpolation of blind sectors; (vi) application of the empirically derived daily variable Z/R relationship. In this equation Z means radar reflectivity factor and R stands for rainfall intensity. For more information about the calibration algorithm, please refer to [22]. The final product from the radars used a blending technique for overlapping areas and temporal data gaps were completed using additional data from the rain gauges. For further information about the extended calibration strategy, please refer to [23].

The observed rainfall data from the radars were quality-controlled for detecting possible inconsistencies and selecting high-quality data. All the scenes from the radars were visually inspected. National Institute of Meteorology and Hydrology (INAMHI)

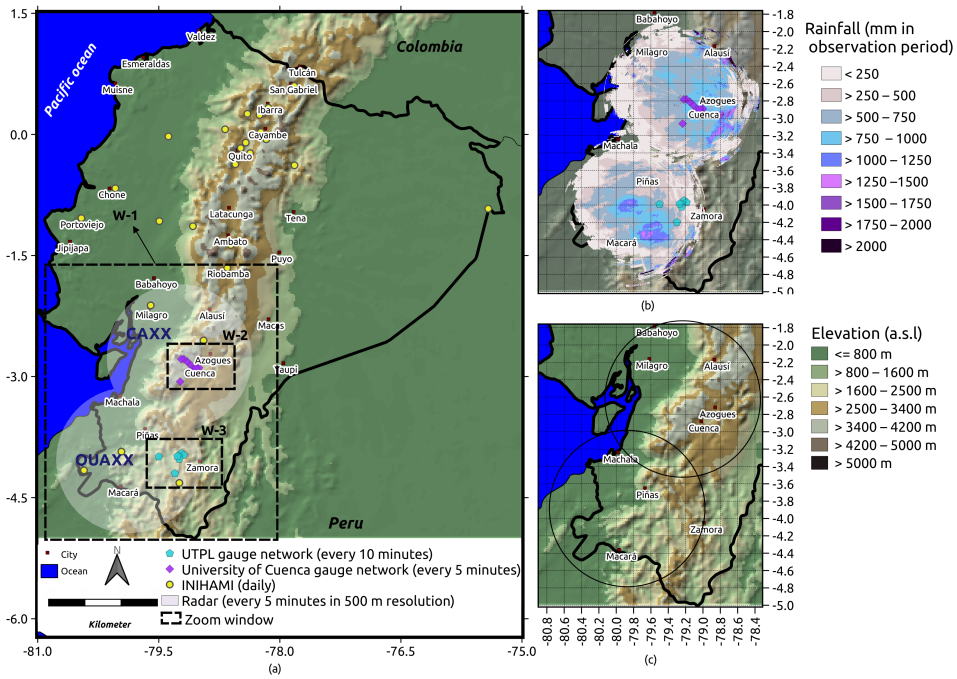

Figure 4.1: The distribution of (a) meteorological stations (19 April 2017 to 28 February 2018) and spatial coverage of radars (GUAXX: 16 June 2017 to 1 February 2018; CAXX: 19th April 2017 to 1 July 2017) used in this study, (b) the radars in the study period (GUAXX: 16 June 2017 to 1 February 2018; CAXX: 19th April 2017 to 1 July 2017). For validation purposes, we excluded the radar data in the very near range (<10 km distance from the radar site) to avoid contamination through noise. We also excluded the far range >50 km due to possible attenuation errors. Nevertheless, we show the rainfall amount in the entire radar range for better illustration. The extent of study area is shown in windows (W)-1. (c) Spatial distribution of the elevation in the radar coverage area. W-2 and W-3 rectangles outline the extent of Figure 4.2a,b.

(daily), the Universidad TécnicaParticular de Loja (UTPL) gauge network (10 min resolution), and the Cuenca University gauge network were used as references. The scenes in which there were no rain in the radar but rain in each of the gauges and vice versa were removed. Additionally, obviously failed recordings were manually removed. Furthermore, we used the infrared channel IR 3.9 from GOES-16 to detect the movement of cold clouds and radar rainfall rate. Although we have enough data available in our observation period, electronic technical problems and other issues caused data failure.

We delivered the final products of radar reflectivity and rainfall rate after

attenuation and clutter correction for the time period between April 2017 and the end of January 2018 (GUAXX: 16 June 2017 to 1 February 2018; CAXX: 19 April 2017 to 1 July 2017). The reflectivity ranged from −31.5 to 91.5 dBZ with a total of 256 possible values.

The spatial distribution of the sum of the radar rainfall for the observation period is shown in Figure 4.1b. The rainfall sum , showing totals between 250 and 4492 mm. The rainfall pattern is different over the study region, covering a climatically diverse area. The spatiotemporal rainfall distribution in the radar coverage is generally affected by the Andes mountains, the El Niño–Southern Oscillation (ENSO), the biannual migration of the intertropical convergence zone (ITCZ), and also the cold von Humboldt current in the Pacific Ocean, [15, 24, 25]. On the eastern sides of the Andes, the strong topographic slopes and easterly winds result in orographic effects [26, 27], which is causing the cyclical spatiotemporal rainfall behavior

4.2.1.2 Meteorological Stations

A meteorological station network, comprising 21 high-temporal-resolution rain stations, was used in this study. Meteorological station data were obtained from UTPL and University of Cuenca. Meteorological stations from UTPL and University of Cuenca provide rain data every 10 and 5 min, respectively. Daily rainfall information was acquired from INAMHI. Meteorological station data from 19 April 2017 to 28 February 2018 were used as validation information to examine radar quality. The high temporal resolution meteorological stations from UTPL and the University of Cuenca are used to validate the satellite-based products at the time of MW-overpasses. We obtained the data from all organizations after quality checks.

The quality check for the station data from the University of Cuenca is performed by drawing a cumulative precipitation curve that identifies abnormal records (outliers and wrong measurements). These measurements are disregarded from the time series. In addition, correlation to nearby stations is also performed as a double check if necessary. In order to maximize the quality of the measurements, regular maintenance of the stations in the field (every three weeks or fewer) is performed. For the INAMHI data,it is checked if daily values are between 0 and 250 mm, which is the maximum daily precipitation value registered at a national scale.

Figure 4.1a shows the distribution of the meteorological stations used in this study.

It should be noted that these data are not included in the Global Precipitation Climatology Center (GPCC) network and therefore not used for the gauge-calibrated

final IMERG product.

4.2.1.3 Integrated Multi-Satellite Retrievals for GPM

IMERG is a level 3 product which integrates all MW sensors, MW-calibrated IR estimates, and rain gauge measurements on a global scale [28]. All MW estimates, after calibration, were subjected to the Climate Prediction Center MORPHing technique (CMORPH) [29] to calculate the motion vectors from the IR measurements and the different atmospheric variables from numerical models. In regions without direct PMW overpasses, the algorithm uses the retrieved rainfall from PERSIANN-CCS [14] and GEO IR (IR-only IMERG) to complete the gridded product. In the last step, the monthly rain data from the GPCC were used to as a bias correction of the rainfall estimate [28].

In this study, the latest available version of IMERG (IMERG-V06 [28]), which displayed an overall improvement in the precipitation estimation compared with version-05 [30], was used.

The IMERG provides rainfall estimates with the spatial resolution of 0.1° (11 km^2) in every 30 min. We focused on the final product of IMERG Version 06 (IMERG-V06), gauge-adjusted retrievals for the study period. NASA also provided the quality index (QI) as a variable in 30 min resolution [31]. The QI indicates the relative quality of rainfall estimates in half-hourly IMERG products, fluctuating temporally between passive MW (PMW) and IR-based rainfall estimates. Additionally, the time of the overpass of each MW swath is provided in metadata with the name of 'HQobservationTime'.

For our validation, the multi-satellite precipitation estimates with the gauge calibration subdata set of IMERG (precipitationCal), as well as "IRprecipitation" was used. In this study, IRprecipitation and IR-only IMERG are equivalent.

4.2.1.4 Random Forest-Based Rainfall

The random forest-based rainfall (RF-based rainfall) product is the regionally calibrated rainfall retrieval scheme developed Ecuador by Turini et al. [3]. The algorithm uses random forest (RF) to calculate rainfall rates in surface level by means of multi-spectral IR data from Geostationary Operational Environmental Satellite 16 (GOES-16). The algorithm is trained based on MW-only precipitation data from IMERG-V06. The RF-based rainfall product was implemented by (i) delineating the rain area, and (ii) assigning of the rainfall rate at 11 km^2 spatial resolution and for

the time of a MW overpass. As predictors, GOES IR bands, band combinations, geostatistical texture features calculated from the original GOES IR bands, and ancillary data were used. Turini et al. [3] used the geostatistical texture features to capture the clouds' heterogeneity. They calculated the texture features using a 5×5 pixel moving window method. First, for each GOES IR band, variograms (VARs), madograms (MADs), and rodograms (RODs) and then, for each possible bands combination, cross-variograms (CVs) and pseudo cross-variograms (PCVs) were calculated. Please refer to Schulz et al. [32] for more information about definitions and equations of texture features. The most important features were obtained monthly for each of the steps (rain area delineation and rainfall rate assignment) separately. The model tuning and feature selection results showed that, in addition to the ancillary data, the information recorded in the geostatistical texture features was the most important for rain area delineation and rainfall rate assignment [3].

The PCV was the dominant texture feature selected in almost all months, both for rain area delineation and rain rate assignment [3].

After training the models, the RF-based rainfall at a high spatiotemporal resolution (2 km^2, 15 min) was estimated. In this step, the models were applied to the GOES-16 scenes where MW-IMERG was available and the following scenes until the next model was present in Turini et al. [3]. The product is available from 19 April 2017 to 19 April 2018.

4.2.2 Methods

Three different validations were employed in this study to assess satellite-based rainfall product performance. Due to the different availabilities of the slots of the products, the period for this study ranged from 19 April 2017 to 1 February 2018 in the time slots where radar data are available.

- The performance of the satellite-based rainfall products are investigated against the X-band rain radar network at the time of MW overpass at a spatial resolution of 11 km^2.

- The performance of the satellite-based rainfall products is investigated against the ground based meteorological station network at the time of MW overpass at a spatial resolution of 11 km^2.

- The RF-based rainfall product is validated against the X-band rain radar network in the temporal resolution of 30 min and spatial resolution of 2 km^2.

4.2.2.1 Validation of Satellite-Based Rainfall Products at the Time of MW Overpass from IMERG

The first validation was performed to investigate satellite-based rainfall products' performance against X-band rain radar network when MW overpass sensors from IMERG are present. This is essential since the IMERG data set has been widely used to develop satellite-based rainfall products [8, 12, 13, 33].

We used different subdata sets in the IMERG product. We first considered the pixels from "precipitationCal" when the PMWs swat was available ("HQobservation"). Then, the pixels with the "PrecipitationQualityIndex" >0.6 (which indicates the current half-hour microwave swath data) [31] were picked out. "IRprecipitation" were also selected in the same pixels from IMERG. This data set (IR only) was retrieved from the PERSIANN-CCS in IMERG, which are calibrated regionally to the PMW-only measures [28]. Therefore, in this study, we named this product "IR-only IMERG".

To compile the most robust data set for the first validation of satellite-based rainfall products against the radars at the time of MW overpass in IMERG, we defined the following criteria: (i) For temporal matching, we used "HQobservationTime" for IMERG to determine the exact time of MW overpass in each pixel. Then, we rounded the MW overpass time to the closest 5 min to be compatible with the temporal resolution of the radar (every 5 min). In this step, we assumed that the RF-based rainfall and IR-only IMERG have the same timing as the time of MW overpass. (ii) To ensure the high-quality rainfall information from IMERG (merged MW-only precipitation estimates), we used the "PrecipitationQualityIndex". (iii) Sensitivity to light rain continuously degrades with increasing distance from the radar. To only assess the near range, we applied a circular mask with a radius of 50 km from the center of each radar. (iv) A mask for filtering the radar data for plausibility was also applied. A value of 1 indicates reliable data from radars. (v) There was some noise in the center of the radar due to the cross-talk from the antenna's side-lobes. Therefore, we omitted the inner pixels with a radius of 10 km from the center for the validation. (vi) Due to the different spatial resolutions of the RF-based rainfall (2 km^2), radar (0.5 km^2), radar quality index (0.5 km^2), DEM (1 km^2), and IMERG (11 km^2), the average resampling techniques in gdal [34] were used to guarantee

spatial matching between the different data sets. In our study, we used the WGS84 projection coordinate system and all dataset were resampled to the spatial resolution of IMERG (11 km^2). (vi) The 0.5 mm/h was used as a threshold between rainy and non-rainy pixels for validation. (vii) The pixels in the radar considered rainy (>0.5 mm/h) but red has a dBZ lower than −15 were considered false and filtered out from the validation data set.

By applying above criteria and withdraw the data pairs of the first validation against radar on a pixel basis, a total of 117,183 pixels of radar and MW-based IMERG, RF-based rainfall, and IR-only IMERG were made available at a half-hourly resolution for validation.

In the second validation, the overall performance of the rainfall area delineation and rainfall rate assignment was investigated for each product against data from ground based meteorological stations at the time of the MW overpass.

For comparison with the meteorological ground based station network, we only considered pixels with a minimum number of three gauges (see Figure 4.2). Tang et al. [35] underline that gauge networks with limited numbers of gauges in each pixel leads to underestimation of the performance of satellite-based rainfall products. This is because the point observations of gauges cannot represent pixel-based precipitation. Therefore, for this validation the stations from University of Cuenca with the temporal resolution of 5 min (Ana Davis, Zona Militar Davis and Balzay) and from UTPL (UTPL Militar, UTPL Tecnico and UTPL Villonaca) with the temporal resolution of 10 min are considered.

To generate the dataset for ground truth validation of the three satellite-based products against the gauge network, we proceeded as follows: (i) for temporal matching, we used "HQobservationTime" for IMERG to determine the exact time of MW overpass in each pixel. Then, we rounded the WM overpass time to the closest 5 min to be compatible with the temporal resolution of the radar (every 5 min). In this step, we assumed that the RF-based rainfall and IR-only IMERG have the same timing as the time of MW overpass. (ii) To ensure the high-quality rainfall information from IMERG (merged MW-only precipitation estimates), we used the "PrecipitationQualityIndex". In the next step (iii), the spatial matching were done using the average resampling techniques in gdal [34] to resample the products to the spatial resolution of IMERG (11 km^2). (iv) The threshold of 0.5 mm/h was used to distinguish between rainy and non-rainy events. (v) After selecting pixels, the arithmetic mean rainfall from station data was computed in these pixels, given that

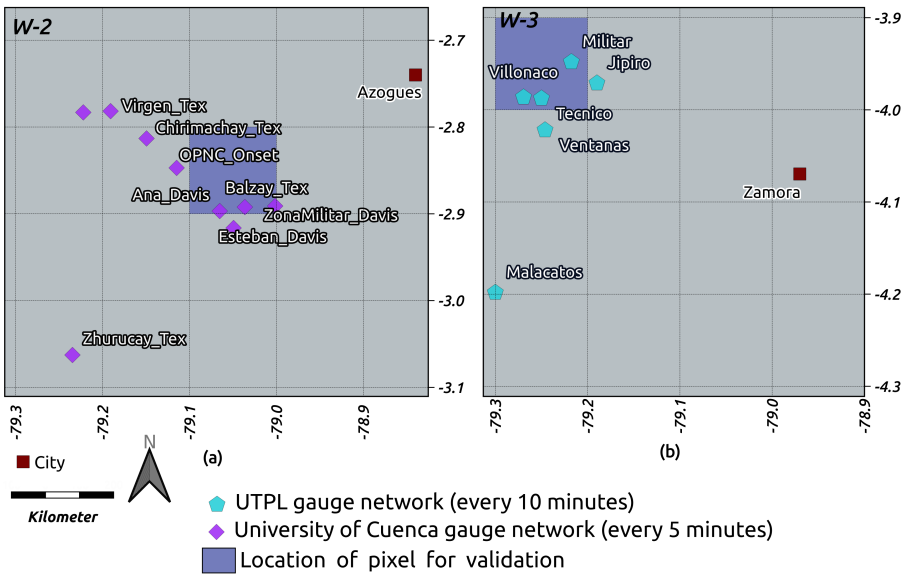

Figure 4.2: Location of pixels with a minimum number of three gauges for (**a**) the University of Cuenca gauge network and (**b**) the UTPL gauge network. In Figure 4.1a, W-2 and W-3 rectangles outline the extent of (a) and (b), respectively.

every pixel includes three stations at minimum.

4.2.2.2 Validation of RF-Based Rainfall Products in Native Resolution

In the third validation, we investigated the general behavior RF-based rainfall in rainfall area delineation and rainfall estimation in the native spatial resolution (2 km^2) and every 30 min in the entire study area for th study period. To prepare the data set for this validation strategy, we defined the following criteria: (i) In our study, area, subscale convective rainfall systems in the transition zones and valleys[36] are dominant. To understand satellite-based rainfall products' capability to capture these events, we kept the original spatial resolutions of the RF-based rainfall, 2 km^2; (ii) to minimize the uncertainties caused by the potential temporal offset between RF-based rainfall products, the radar and RF-based rainfall were aggregated in time to 30 min. For the temporal aggregation of the radar and the RF-based rainfall, we considered a unit conversion between mm/h and mm/30min. (iii) We used a threshold of 0.2 mm/30min to distinguish between rainy and non-rainy pixels for validation; (iv) equal t the first validation strategy, the pixels of the radar considered rainy (>0.2 mm/30

min) at a dBz lower than −15 dBz were considered false and were removed from the validation data set. (v) We omitted the inner pixels within a radius of 10 km^2 from the center; (vi) a mask for filtering the radar data for plausibility was also applied. (vii) In the next step, the RF-based rainfall was aggregated for the observation period in 1 h, 3 h, and daily for evaluation against the radar.

4.2.2.3 Validation Metrics for Rainfall Area Delineation and Rainfall Estimate

We considered all pixels from the validation data set in each validation strategy for the validation of rainfall area delineation. First, we calculated the cross-table's respective satellite-based rainfall products in comparison with the radar as a reference. Therefore we calculated the misses (M), hits (H), false alarms (F), and correct negatives (C). We define hit when the satellite-rainfall product and the radar are both raining in the same location; A miss occurs when the satellite-rainfall product is not raining but the radar shows rain, a false alarm holds when the satellite-rainfall product is raining but the radar is not and a correct negative is when both, the satellite-rainfall product and radar are showing cloudy but not rainy conditions (Figure 4.3).

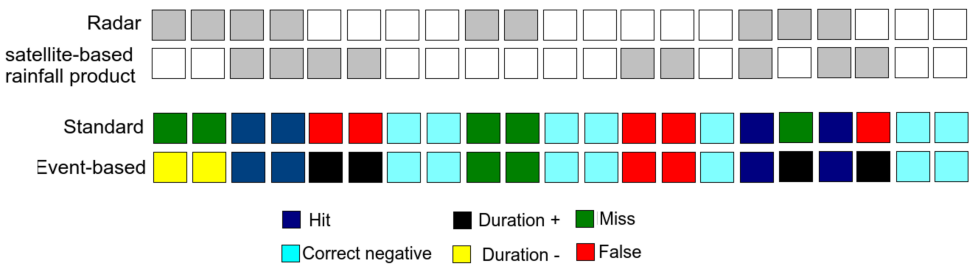

Figure 4.3: Schematic view of how H, M, and F were designated in the rain area validation. The dry pixels are shown in white, and the rainy pixels are shown in grey. The standard approach defines M (F) when a rainy pixel in the radar (satellite-based rainfall product) is related to a dry pixel in the satellite-based rainfall product (radar) at the same time. In the temporal event-based approach (fourth row), the M (F) in the vicinity time of hits are defined as a reduction (continuous) in the event duration. Thus, the terms Duration+ (Duration-) are described. True misses and true false alarms are the errors occurring simultaneously or in the same pixel, respectively [17].

We also defined temporal and spatial events. Schematic images of temporal and spatial events are illustrated in Figures 4.3 and 4.4, respectively.

Temporal events were defined to check the time lag effect of satellite scanning.

You et al. [37] stressed this aspect for PMW observation. Later, Maranan et al. [17] investigated the time lag effect in IMERG, where false alarms were reduced through the temporal shift in IMERG relative to surface observations.

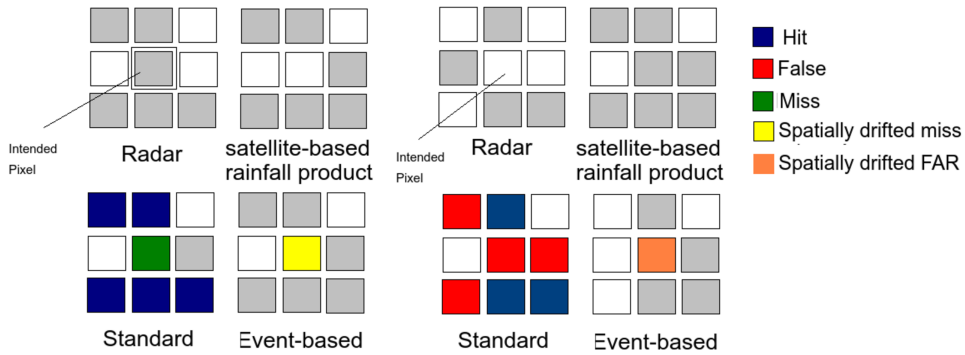

Figure 4.4: Schematic view of how hits, misses, and false alarms are designated in the rain area validation. The dry pixels are shown in white, and the rainy pixels are shown in grey. The standard approach defines M (F) when a rainy pixel in the radar (satellite-based rainfall product) is related to a dry pixel in the satellite-based rainfall product (radar) at the same time. In the spatial event-based approach (second row), the M (F) in the neighboring pixels are defined as a spatially drifted miss (false alarm) of the event. The errors simultaneously and in the same pixel are called true misses and false alarms, respectively.

We calculated the probability of detection (POD), false alarm ratio (FAR), and Heike skill score (HSS) as validation metrics from the H, M, F, and C.

To evaluate the accuracy of estimated rainfall from each satellite-based rainfall product, we used the mean absolute error (MAE), root mean square error (RMSE) and mean error (ME), and their normalized counterparts. These metrics were calculated when it was rainy for both radar and satellite-based rainfall products. Table 4.1 shows the detailed equations and the range of these metrics.

Table 4.1: List of validation metrics used in this study for rain area delineation and rain estimate.

Name	Metrics Equation	Range	Optimum
Probability of detection	POD=$\frac{H}{H-M}$	(0,1)	1
False alarm ratio	FAR=$\frac{F}{F-C}$	(0,1)	0
Heike skill score	HSS=$\frac{2(H\times C-F\times M)}{(H-M)(M+C)+(H+F)(F+C)}$	(0,1)	1
Mean absolute error	MAE=$\frac{1}{n}\sum_{i=1}^{n}\lvert P_i-O_i\rvert$	-	-
Normalized mean absolute error	NMAE=$\frac{\frac{1}{n}\sum_{i=1}^{n}\lvert P_i-O_i\rvert}{\frac{1}{n}\sum_{i=1}^{n}O_i}$	-	-
Root mean square error	RMSE=$\sqrt{\frac{\sum_{i=1}^{n}(P_i-O_i)^2}{n}}$	-	-
Normalized root mean square error	NRMSE=$\frac{\sqrt{\frac{\sum_{i=1}^{n}(P_i-O_i)^2}{n}}}{\frac{1}{n}\sum_{i=1}^{n}O_i}$	-	-
Mean error	ME=$\frac{1}{n}\sum_{i=1}^{n}(P_i-O_i)$	-	-
Normalized mean error	NME=$\frac{\frac{1}{n}\sum_{i=1}^{n}(P_i-O_i)}{\frac{1}{n}\sum_{i=1}^{n}O_i}$	-	-

4.3 Results

4.3.1 Validation Metrics for Satellite-Based Rainfall Products at the Time of MW Overpass against X-Band Rain Radar Network

4.3.1.1 Rain Area Delineation

The frequency of occurrence of the cross-table components formed on all available MW overpass timing (n = 51,384) is presented in Figure 4.5. Less than 5% of the MW overpass times in either radar or satellite-based rainfall products contain rainfall and a total of 0.73%, 0.58%, and 0.39% are hits for MW-based IMERG, RF-based rainfall, and IR-only IMERG, respectively. Successively, false alarms dominated the error with a fraction of 2.53% for MW-based IMERG, 2.08% for RF-based rainfall,

and 2.24% for IR-only IMERG. All three product show reasonable agreement with the radar at the time of MW overpass Table 4.2. All products have a high FAR (0.78 for MW-based IMERG and RF-based rainfall, and 0.85 for IR-only IMERG).

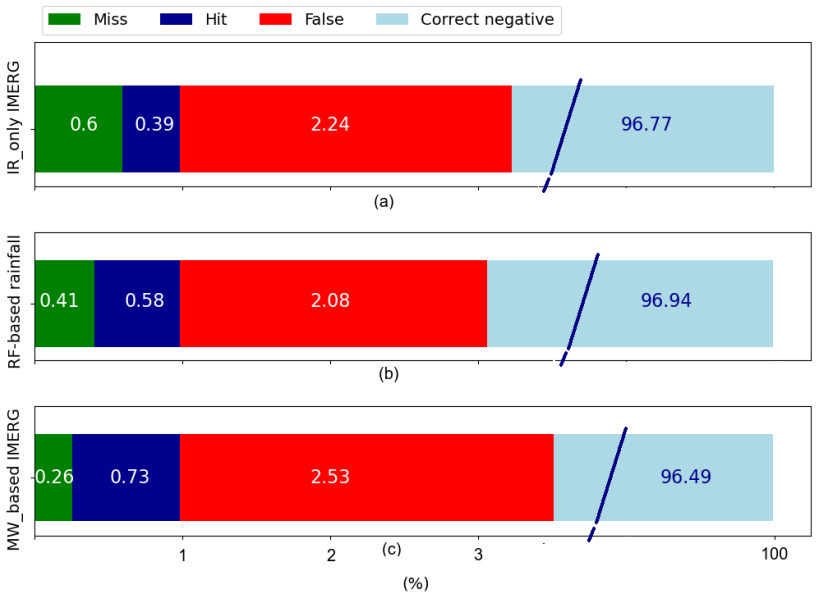

Figure 4.5: Standard cross-table approach for all available MW overpass times for the validation of rain area delineation for (**a**) IR-only IMERG, (**b**) RF-based rainfall, and (**c**) MW-based IMERG. Note that the correct negative fraction extends to 100%.

Table 4.2: The rain area delineation performance of satellite-based rainfall over the MW overpass time compared to ground radar network.

Satellite-Based Rainfall Products	**POD**	**FAR**	**HSS**
MW-based IMERG	0.74	0.78	0.33
RF-based rainfall	0.58	0.78	0.31
IR-only IMERG	0.39	0.85	0.2

Overall, MW-based IMERG exhibits relatively better performance (HSS = 0.33), RF-based rainfall performs somewhat the same as MW-based IMERG (HSS = 0.3), whereas IR-only IMERG performs the worst (HSS = 0.2). This shows the higher potential of using multispectral GEO data (RF-based rainfall) compared with only one IR channel rainfall retrieval, as is the case for IR-only IMERG [3, 8, 12, 13].

Figure 4.6 reveals the spatial performance of the satellite-based rainfall products at the time of MW overpass during the study period. Figure 4.6c,f,i shows the spatial distribution of HSS for MW-based IMERG, IR-only IMERG, and RF-based rainfall, respectively. The HSS share similarities in the spatial distribution for all products, with the maximum occurring at the north and northeast of the study region (0.4–0.7 for MW-based IMERG,and 0.4–0.8 for IR-only IMERG and RF-based rainfall). However, in the northwestern part of the region, the ability to capture precipitation is almost lost due to the lower POD and higher FAR (0.7–1 for MW-based IMERG, IR-only IMERG, and RF-based rainfall) in all the products. The GUAXX radar performs better in terms of POD in general but with a relatively higher FAR (0.6–1 for MW-based IMERG, and 0.7–1 for IR-only IMERG and RF-based rainfall), and this phenomenon illustrates that the products have difficulties in capturing the rainfall in these region (HSS of 0.1–0.6 for MW-based IMERG, 0.1–0.3 for IR-only IMERG, and 0.1–0.6 for RF-based rainfall). Please note that the time periods of available data for GUAXX and CAXX are different.

Figure 4.7 provides an overview of the validation metrics of the three satellite-based rainfall products for rain area delineation, along with the altitude. All products have a high FAR and a convincing POD. The performance at a terrain elevation of approximately 0–1500 m.a.s.l is relatively lower for all of the three products with HSS of 0.2–0.29 for MW-based IMERG, 0.1–0.22 for IR-only IMERG, and 0.2–0.25 for RF-based rainfall. The rain area delineation performance increased until 3000 m.a.s.l At 0–750 m.a.s.l, the RF-based rainfall (HSS = 0.25) performs the best of all products.

Figure 4.8 provides an overview of the rain area delineation performance, along with different rainfall rates. In all products, rainfall rates lower than 2 mm/h have the highest FAR. With increasing rainfall rate, the performance of all products increases until 6 mm/h. For a rain rate of more than 6 mm/h, the products perform steadily. Altogether, the graph confirms (i) the poor rain area delineation performance at lower rainfall rates in Ecuador, and (ii) the WM-based IMERG shows the best performance with different rain rates in Ecuador, followed by RF-based rainfall.

4.3.1.2 Rainfall Estimation

Table 4.3 exhibits the ability of satellite-based rainfall products to estimate rainfall at the time of MW overpass. RF-based rainfall shows the best performance compared with the two other products. All three products underestimate rainfall, indicated by

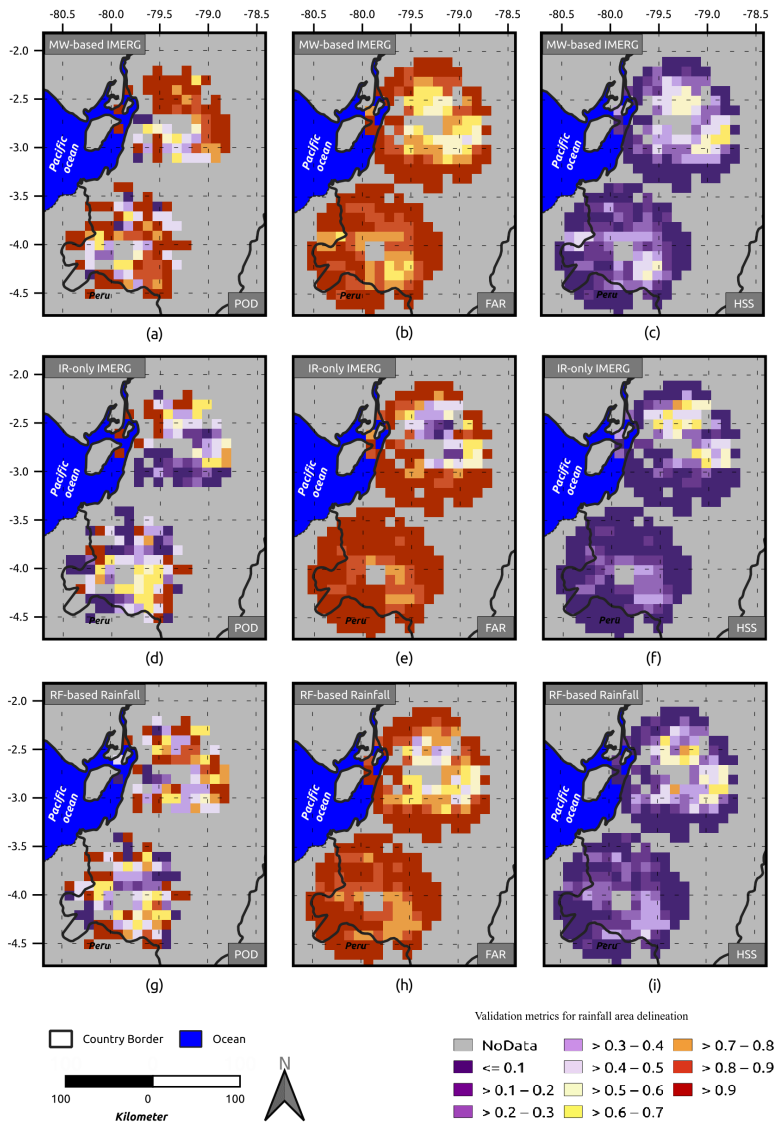

Figure 4.6: Spatial distribution of the validation metrics for rain area delineation at the time of MW overpass. (**a**) POD, (**b**) FAR, and (**c**) HSS showing the matrics for MW. The variables were calculated for MW-based IMERG. (**d**) POD, (**e**) FAR, and (**f**) HSS illustrating the performance of IR-only IMERG. (**g**) POD, (**h**) FAR, and (**i**) HSS showing the RF-based rainfall performance. The variables were calculated for each grid point of the validation data set over the stated period. For better illustration, we show the results up to 75 km distance from the center of each radar.

their negative ME and NME.

The scatter plots in Figure 4.9 illustrate how the rainfall rate at the time of MW overpass is distributed for each of the satellite-based rainfall products against the

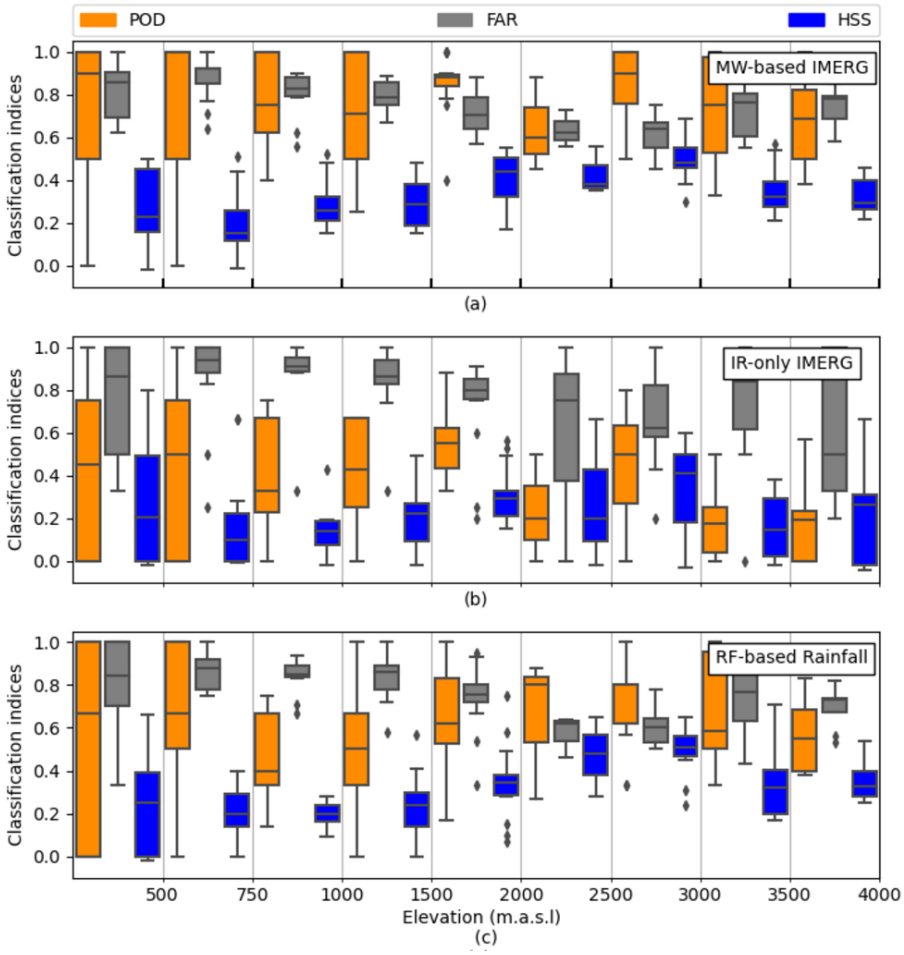

Figure 4.7: Boxplot of the validation metrics for rain area delineation over the MW overpass time. The performance of (**a**) MW-based IMERG, (**b**) IR-only IMERG, and (**c**) RF-based rainfall along elevation. Boxes show the 25th, 50th, and 75th percentiles. Whiskers extensions are to the maximum data value between the 75th and 25th percentiles. Diamonds indicate outliers.

radar. Only pixels with hits are considered, therefore the number of hits (n) differs for each product (Figure 4.9a,d,g). The overall variability in all the products is high, which might be due to issues in timing or/and rainfall estimation (Figure 4.9a,d,g) [17]. Overall, IR-only rainfall shows the best correlation line close to 1:1. The regression line also indicates the underestimation by RF-based rainfall. MW-based IMERG and IR-only rainfall overestimate the rainfall rate. Figure 4.9b,e,h shows the rainfall rate for each product against radar in quantile–quantile (Q–Q) plots.

The Q–Q plot ignores the corresponding time steps in order to underline the differences between the radar and each product in a more comprehensive manner

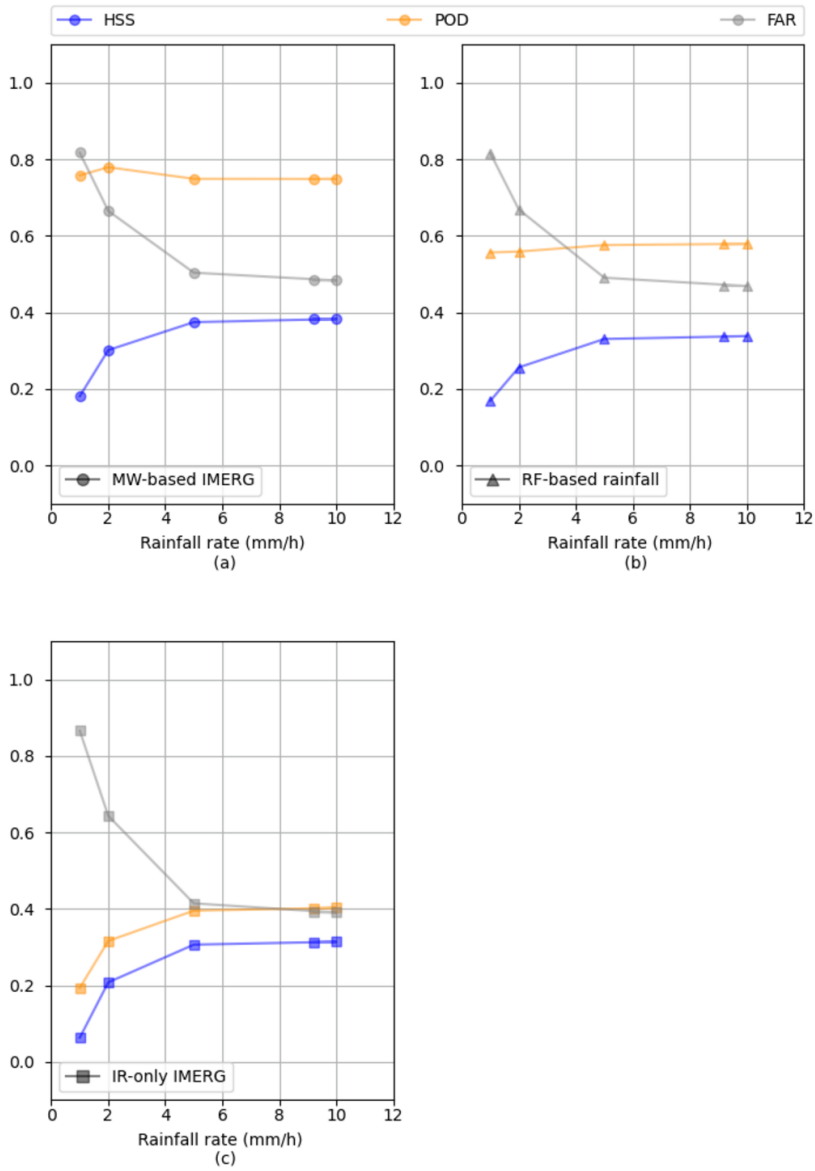

Figure 4.8: The rain area delineation performance over the MW overpass time and at 11 km^2 for different rainfall rates for (**a**) MW-based IMERG, (**b**) RF-based rainfall, and (**c**) IR-only IMERG.

[17]. In MW-based IMERG (Figure 4.9b) the rainfall rate is almost evenly distributed up to 5 mm/h, the positive values for MW-based IMERG at higher rainfall rates are more evident. The distribution of the rainfall rate between radar and IR-only IMERG shows more discrepancies (Figure 4.9e). IR-only IMERG shows negative biases until the 90th percentile and shows high positive bias for the higher rainfall rates. RF-based rainfall is distributed relatively even for all rainfall rates, with a slight negative bias

Table 4.3: The rainfall estimation performance of satellite-based rainfall over the MW overpass time compared to ground radar network.

Satellite-based rainfall products	**RMSE (mm/h)**	**NRMSE**	**MAE (mm/h)**	**NMAE**	**ME (mm/h)**	**NME**
MW-based IMERG	2.96	0.82	1.86	1.35	–1.48	–1.07
RF-based rainfall	2.47	0.8	1.66	1.16	–1.34	–0.93
IR-only IMERG	4.65	1.27	2.5	1.63	–2.13	–1.39

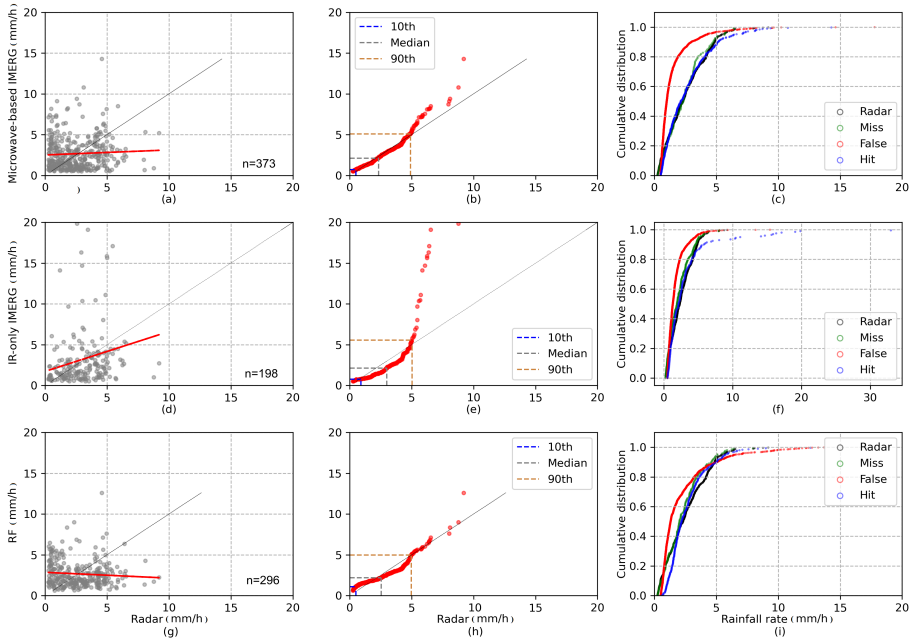

Figure 4.9: Comparison of rainfall rates estimated by the radar and satellite-based products. (a,d,g) Scatter plot with radar rainfall rates (x-axis) and microwave-based IMERG, IR-only IMERG, and RF-based rainfall rates (y-axis), respectively. Only pixels with hits are considered. The parameters n show the total number of hits. (b,g,h) Quantile–quantile (Q–Q) plot of the radar (x-axis) and microwave-based IMERG (y-axis), IR-only IMERG (y-axis), and RF-based (y-axis) rainfall rates. The 10th, 50th, and 90th percentiles are illustrated. (c,f,i) The distribution of cumulative rainfall rate for the contingency table of each satellite-based product. The radar rain rate is displayed in black as a reference.

between 3 and 5 mm/h. Overall, IR-only IMERG and MW-based IMERG are unable to model the most extreme rainfall rates. For extreme rainfall rates, RF-based rainfall shows better performance. The cumulative distribution of the rainfall rates for hits and the other contingency table elements is compared in Figure 4.9c,f, i, for MW-based IMERG, IR-only IMERG, and RF-based rainfall, respectively. In MW-based IMERG (Figure 4.9c) and RF-based rainfall (Figure 4.9i), around 60% of the FARs is equal to or less than 1 mm/h. This is also true for IR-only IMERG (Figure 4.9f). The FAR is also shown for higher rainfall rates in the RF-based rainfall product. This underlines that the algorithm is flawed for low-intensity rainfall in these products [17]. The misses show the same distribution as the radar's distribution for all three products.

Figure 4.10 provides an overview of the validation metrics of the three satellite-based rainfall products for rain estimation along with altitude. MW-based IMERG and IR-only IMERG have difficulty estimating rainfall at lower elevations (0–500 m.a.s.l), which is shown by the extension of the boxplot for NRMSE and NMAE in this elevation range. RF-based rainfall has relatively lower values of NRMSE, NMAE, and NME at an elevation of 0–500 m.a.s.l. With increasing elevation, the rain estimation performance is relatively moderate until 2500 m.a.s.l. For high terrain elevations of approximately 2500–4000 m.a.s.l, all products show a significant uncertainty, mainly in NME. All the products underestimate the rainfall rate at high elevation (2000–4000 m.a.s.l).

4.3.2 Validation Metrics for Satellite-Based Rainfall Products at the Time of MW Overpass from IMERG against Meteorological Stations

Table 4.4 summarizes the performance of satellite-based rainfall products for rain area delineation against meteorological stations at the time of MW overpasses for the pixel in W-2 (Figure 4.2a) and W-3 (Figure 4.2b).

The validation scores show the superior performance of the IMERG-MW-based and RF-based rainfall products in comparison to IMERG-IR-only in W3. W2 shows a slightly better performance for RF-based rainfall while IR-only IMERG and MW-based IMERG are more or less the same. Still, all of the products overestimate precipitation area. These behaviors are similar to the validation of the rainfall products at the MW overpass time against the X-band rain radar network (Table 4.2). However, the validation scores indicate a lower performance of the satellite-based

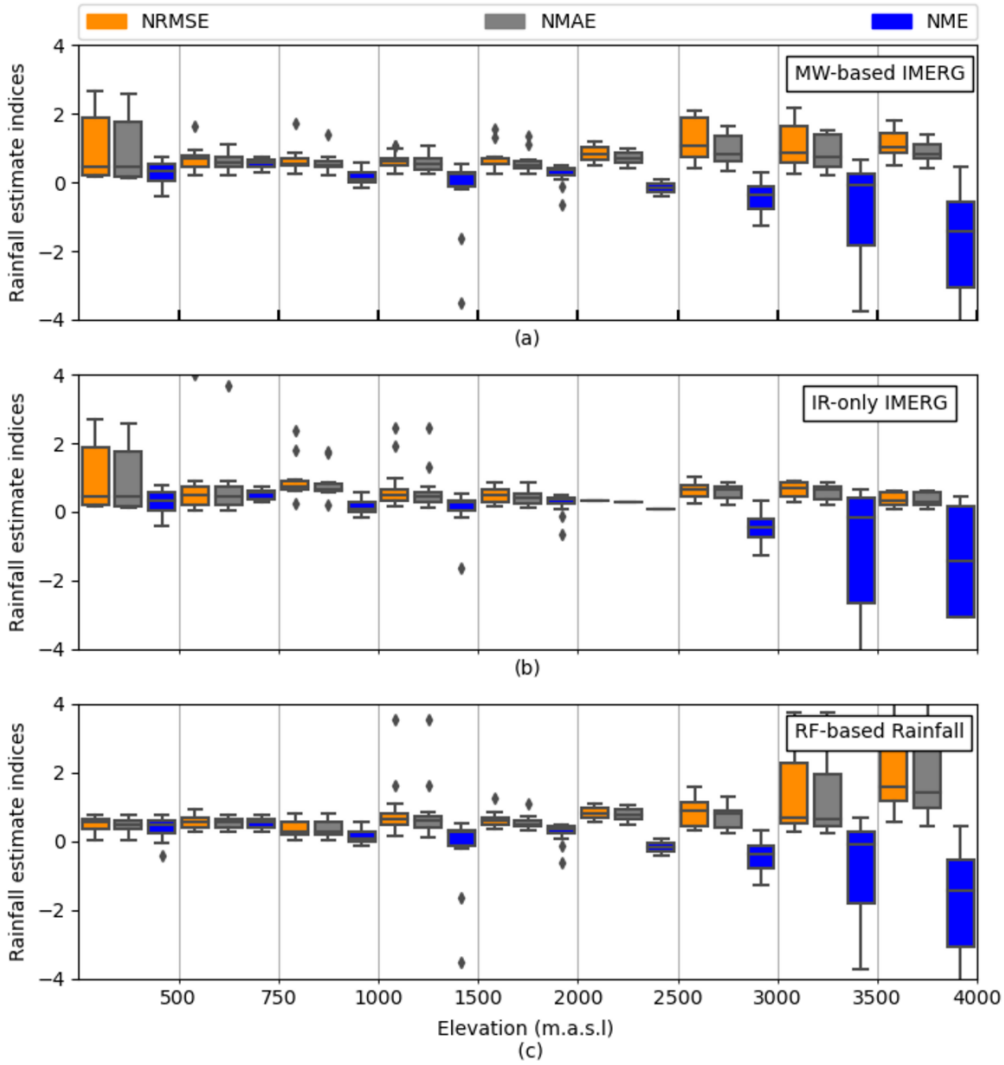

Figure 4.10: Boxplot of the validation metrics for rain estimation at the MW overpass time. The performance of (**a**) MW-based IMERG, (**b**) IR-only IMERG, and (**c**) RF-based rainfall are shown along with elevation. Boxes show the 25th, 50th, and 75th percentiles. Whiskers extensions are to the maximum data value between the 75th and 25th percentiles. Diamonds indicate outliers.

rainfall products by using the radar data compared to higher scores by using the station data. This is not surprising, since a low number of the gauges in a pixel (3 gauges in 11 km^2) is not representative for the spatial distribution of rain. Therefore, the assessment of satellite-based rainfall products against a low number of gauges in each pixel underestimates their performance [35].

Table 4.5 shows the satellite-based rainfall products' ability to estimate the rainfall

Table 4.4: Rain area delineation performance of satellite-based rainfall products at the time of MW overpass compared to the meteorological station network. Pixel W-2 and W-3 are shown in Figure 4.2a and Figure 4.2b, respectively.

Pixel Number	Satellite-Based Rainfall Products	POD	FAR	HSS
W-3	MW-based IMERG	0.33	0.83	0.21
W-3	RF-based rainfall	0.25	0.83	0.19
W-3	IR-only IMERG	0.17	0.89	0.12
W-2	MW-based IMERG	0.29	0.82	0.19
W-2	RF-based rainfall	0.35	0.78	0.24
W-2	IR-only IMERG	0.23	0.82	0.19

at the time of MW overpass against ground truth data. The behavior of satellites is different in two pixels. In W-2, IR-only IMERG shows the best performance compared to the other two products. Meanwhile, in W-3, the RF-based rainfall capture the rain estimate more accurately compared to other products. In general, all of the products overestimate rainfall slightly (positive ME).

Table 4.5: Rainfall estimation performance of satellite-based rainfall over the MW overpass time compared to ground radar network.

Pixel Number	Satellite-Based Rainfall Products	RMSE (mm/h)	NRMSE	MAE (mm/h)	NMAE	ME (mm/h)	NME
W-3	MW-based IMERG	1.10	1.03	0.96	0.91	0.83	0.78
W-3	RF-based rainfall	0.48	0.45	0.85	0.80	0.83	0.78
W-3	IR-only IMERG	3.32	3.11	3.27	3.07	0.83	0.80
W-2	MW-based IMERG	1.03	0.87	0.68	0.57	0.68	0.57
W-2	RF-based rainfall	1.11	0.94	1.05	0.89	0.60	0.71
W-2	IR-only IMERG	0.68	0.58	0.49	0.41	0.77	0.67

4.3.3 Validation Metrics for RF-Based Rainfall Products in Native Resolution

4.3.3.1 Rain Area Delineation

Using the analysis techniques described in Section 4.2.2.3, the ability of RF-based rainfall to estimate rainfall in comparison with the radar at 2 km^2 spatial resolution

and 30 minute temporal resolution is shown in Figure 4.11 (n= 1,048,575). Less than 3% of the time steps in either radar or RF-based rainfall contain rainfall including 0.31% of hits (Figure 4.11a). The errors are dominated by false alarms at 1.57%. The decomposition of misses using the temporal event-based approach shows that almost 12% of the misses occur in the coincidental timing from radar precipitation (Figure 4.11b, Duration −, yellow bar; Duration +, black bar), whereas the spatially drifted misses are not recognizable (Figure 4.11d). Almost 4% of the overestimation occurs by overestimating event duration (Figure 4.11c), and 8.5% by overestimating events in the neighboring pixel (Figure 4.11e).

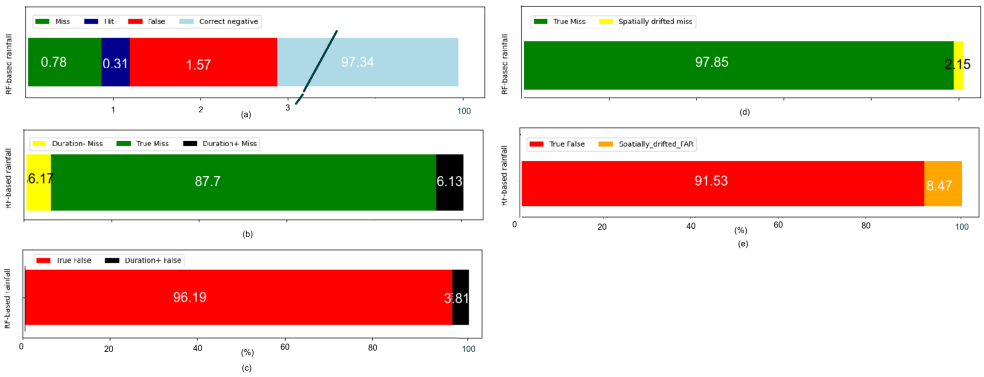

Figure 4.11: (**a**) Standard contingency table approach for all available RF-based rainfall products for both radars at 2 km^2 and 30 min. Note that the correct negative fraction extends to 100%. (**b**,**c**) The temporal event-based approach of the contingency table was evaluated in the M and F subsets, respectively. (**d**,**e**) The spatial event-based approach of the contingency table was evaluated in the M and F subsets, respectively. The numbers in the bars show the percentage.

The performance is summarized in Table 4.6. As expected, a noticeable result is the high FAR of 83%, showing that 83% of rainy events are false alarms. This is almost similar behaviour as for RF-based rainfall at the MW overpass in 11 km^2 temporal resolution (Table 4.2). By applying the algorithm in 2 km^2 spatial and 30 min temporal resolution, the ability of rain detection by RF-based rainfall has reduced compared to the RF-based rainfall in MW-overpasses and at 11 km^2 spatial resolution (HSS = 0.31).

4.3.3.2 Rain Estimation

Table 4.7 summarizes the performance of RF-based rainfall in estimating rain at 2 km^2 spatial and 30 min temporal resolution. The RF-based rainfall shows better

Table 4.6: Performance evaluation of RF-based rainfall at rainfall area delineation for 2 km^2 spatial and 30 min temporal resolution.

Satellite-Based Rainfall Products	**POD**	**FAR**	**HSS**
RF-based rainfall	0.28	0.83	0.20

performance in estimating rainfall at higher resolution compared with lower resolution (Table 4.3).

Table 4.7: Performance evaluation of RF-based rainfall for rainfall estimation 2 km^2 spatial and 30 min temporal resolution.

Satellite-Based Rainfall Products	**RMSE (mm/h)**	**NRMSE**	**MAE (mm/h)**	**NMAE**	**ME (mm/h)**	**NME**
RF-based rainfall	2.39	1.07	1.72	0.77	0.51	0.22

Focusing on hits, Figure 4.12 shows the rain estimation retrieval ability of RF-based rainfall in comparison with the radar. The scatter plot in Figure 4.12a shows the distribution of the half-hourly rain rates. The rain rates illustrates high variability, suggesting problems in rain estimation retrieval and/or timing. This is also shown in Figure 4.9g at the time of MW overpass. Figure 4.12b shows the Q–Q plot for RF-based rainfall. The overall estimation of the rainfall is placed along the 1:1 line to the 90th percentile. However, the curve deviates towards the left after the 90th percentile, showing an overestimation of rain intensities in the outliers. Figure 4.12c decomposes the results in more detail. Overall, RF-based rainfall is unable to detect the most extreme rainfall rates, as reported by Turini et al. [3]. The cumulative distribution of rainfall rates for hits, misses, radar, and false alarms are compared in Figure 4.12a. Around 60% of false alarms and misses are less than or equal to 1 mm/h. This is also true for 60% of event-based (temporally and spatially) false alarms Figure 4.12d. The event-based misses are evenly distributed over the different rainfall rates.

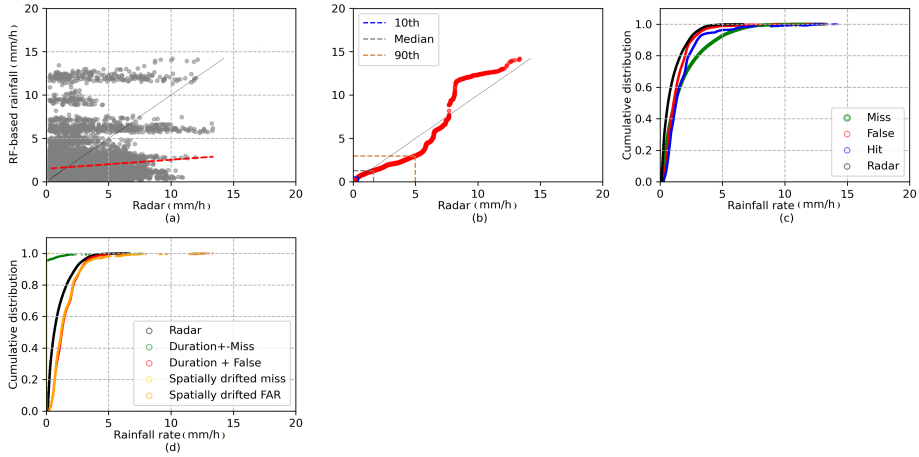

Figure 4.12: Comparison of rain rates estimated by the radar and RF-based rainfall at 2 km^2 and 30 min. (**a**) Scatter plot with radar rainfall (x-axis) and RF-based rainfall (y-axis). Only the pixels with hit are considered. (**b**) Q–Q plot of radar (x-axis) and RF-based rainfall rates (y-axis). The 10th, 50th, and 90th percentiles are illustrate. (**c**) The distribution of cumulative rainfall rate for the contingency table. (**d**) The distribution of cumulative rainfall rate based on the event-based (spatial and temporal) contingency table.

4.3.4 Validation Metrics for RF-Based Rainfall Products at Different Temporal Resolutions

To validate the results of rain area delineation and rain estimation in different temporal resolutions, Figure 4.13a,b presents the validation metrics with the radar for the whole study region and observation period. The results show the best agreements regarding rain area delineation in daily resolution (POD 0.68, HSS 0.4, and FAR 0.6).

The rain estimation indices for RF-based rainfall do not show a significant improvement for the different temporal resolutions. The NME suggests the overestimation of precipitation by RF-based rainfall at lower resolution (after 3 h) and an underestimation at higher temporal resolutions. Note that in this step, we considered rainfall at a rate of more than 0.5 mm/h as rainy.

4.4 Discussion

In Section 4.3.1, satellite-based rainfall products at the time of MW overpasses from IMERG were assessed using radar data. We evaluated the satellite-based products in grid cells at the time of MW overpasses and a spatial resolution of 11 km^2.

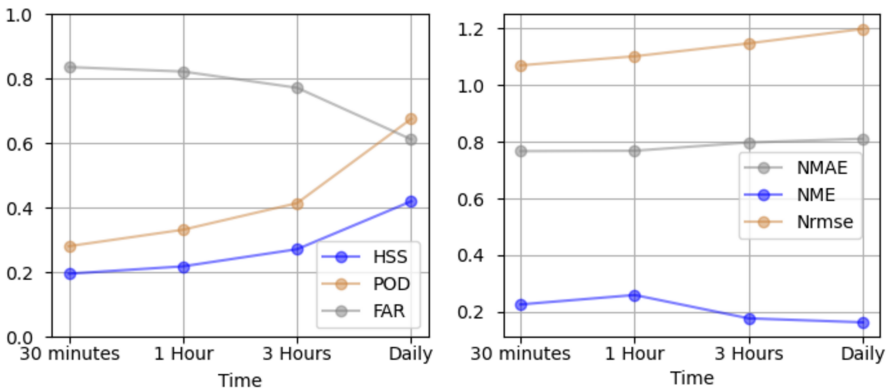

Figure 4.13: Comparison of the validation metrics between the radar and RF-based rainfall at 2 km^2 and 30 min, 1 h, 3 h, and daily. The performance of RF-based (**a**) rain area delineation and (**b**) rain estimation is shown for different temporal resolutions.

The verification scores for rain area delineation revealed that the MW-based IMERG has superior performance in estimating rain area (POD = 0.74, HSS = 0.33).

RF-based rainfall, which is trained based on MW-based IMERG, has slightly lower performance compared to MW-based IMERG data (HSS = 0.31). IR-only IMERG performed the worst in Ecuador. This is in line with the findings of Kolbe et al. [12], Kolbe et al. [13], Turini, Thies, and Bendix [8], and Turini et al. [3]. It shows that multispectral GEO data has more potential than using one IR channel only for rainfall retrieval.

The frequent false alarm is one of the most noticeable issues identified in the present study. This agrees well with the result of IMERG-V06 validation in the west African forest zone [17] and confirms the previous investigation of IMERG-v05 by Manz et al. [15] in the Andes region. In our study, around 60% of the false alarms were related to rain rates less than 1 mm/h for all products (Figure 4.9), which was found to be the dominant rainfall intensity in this region of the world [38]. We also note that the radar potentially underestimated rainfall [39, 40, 41, 42]. This was also reported elsewhere for the radars in Ecuador [23]. In MW-based IMERG and RF-based rainfall, with increasing the rainfall rate, the FAR decreases while POD does not change (Figure 4.8).

The results of the topography-based evaluation indicated the high detection accuracy of MW-based IMERG and RF-based rainfall in different topographical regions. Moreover, the highest errors occurred for coastal areas and foothills

(0–1500 m.a.s.l) and high mountains regions (>3000 m.a.s.l) compared to the other topographical regions. All the products experienced challenges in estimating rainfall at high elevation in the Andes (Figure 4.10). In Ecuador, high-elevation areas and volcanoes have two issues for rainfall retrieval algorithms: (i) They are regularly covered by ice, which generates errors in MW-based IMERG [28, 43]; (ii) the drizzle on the high elevation is hard to be captured by MW and IR channels. This conclusion is in agreement with the findings of study conducted by Prakash et al. [44], who assessed the performance of IMERG products in monsoon-dominated regions in India. Their results showed that IMERG was affected by the orographic process, which leads to higher errors in mountainous areas. Another study by Kim et al. [45] revealed the disadvantage of IMERG products over mountainous and coastal regions. Similar results were obtained by Turini et al. [3] in Ecuador for RF-based rainfall. They argued that because of local topography, the subscale convective rainfall systems probably could not be captured by GOES data and IMERG [3, 36]. Altogether, at the elevation of 0–750 m.a.s.l, RF-based rainfall showed the best performance of all products (Figures 4.7 and 4.10).

Concerning rainfall rate validation, the overall variability in all the products is high, suggesting rainfall rate estimation and/or timing issues. Different studies discuss a possible time lag between the satellite-based rainfall products and the ground-based rainfall measurements as a source of degrading validation results [17, 37, 46, 47, 48]. The time lag is defined as the time shift when satellite observation and surface precipitation rate from ground data obtain to their optimum correlation. This time lag might be due to the time it takes for the precipitation detected by the satellite to reach the ground [17, 46]. You et al. [37] related the precipitation time from GMI to the environmental temperature and storm top height. They found that when the storm is taller, the lag time increases to obtain the optimum correlation between the GMI and ground truth data. This is due to the long way of raindrops from the storm top to the gauge.

Ignoring the corresponding time steps in the Q–Q plots shows that the MW-based IMERG and RF-based (Figure 4.9b,h) rainfall rates are distributed up to 5 mm/h evenly. The positive values in MW-based IMERG at higher rainfall rates are more evident. Conversely, the rainfall rate distribution between the radar and IR-only IMERG shows more discrepancies (Figure 4.9e). The validation of satellite-based rainfall products against the gauges show lower consistency (Table 4.5). However, in the term of rain area delineation (Table 4.4), the RF-based rainfall product

shows better performance than IMERG-IR-only, which confirms the potential to use multispectral GEO data.

The validation of satellite-based rainfall show a slight overestimation of rainfall totals for all products (Table 4.5).

It should be noted that the evaluation of satellite-based products against only a few gauges has high uncertainties [8, 35], especially in areas with high small-scale precipitation variability in mainly convective environments, like the Ecuadorian Andes, where point based observations at weather stations cannot properly represent the spatial rainfall distribution.

The validation of RF-based rainfall retrieval at high spatiotemporal resolution for all the available rain events is shown in Table 4.6. The RF-based rainfall is calibrated locally for Ecuador. The importance of local calibration, which involves determining relevant climatic parameters, including the selection of appropriate temperature thresholds for clouds and a local correlation systematic biases that may not have been adjusted in global products, have been mentioned in different studies [49, 50, 51].

RF-based rainfall for 2 km^2 and 30 min shows a lower HSS compared to the RF-based rainfall for 11 km^2 at the time of MW overpass. This was expected because the errors at higher temporal resolutions may cancel each other out following the aggregation to a lower temporal resolution [49]. However, in terms of rainfall estimation, RF-based rainfall performs better at higher spatial resolution (Table 4.3). This result needs to be interpreted with caution, since the rainfall events at the time of MW overpasses differ from the validation of the RF-based rainfall at 2 km^2 and 30 min.

An event-based analysis was then used to investigate the source of error in the RF-based rainfall product. Shifting the RF-based rainfall backward by one to two time steps (i.e., 30 min) resulted in the more accurate detection of rainfall around 10% (Figure 4.11b) by lowering the misses. RF-based rainfall rates are lower than their counterparts in radar, as shown in Figure 4.12d. We speculate that this lag appears due to the lag time between the time of MW overpass and the GOES-16 scan time. The RF-based rainfall algorithm relies on the precipitation information from MW-based IMERG and IR data from GOES-16.

However, RF-based rainfall also has a high FAR. The event-based spatial analysis reduced the FAR by 8.5% (Figure 4.11e), but the challenge remains the same. High FAR values occur for all the different types of rain with different intensities

(Figure 4.12c,d). The reason for the high FAR in RF-based rainfall might be (i) the high amount of FAR from MW-based IMERG in Ecuador (Table 4.2), which is used as a reference for calibrating of RF-based rainfall; (ii) A bias in IR retrievals that classify cold cloud pixels as rainy. They experience difficulties in defining the correct rainfall cloud and profile, thus producing error in statistical-physical rainfall algorithms.

By increasing the temporal resolution of the RF-based rainfall product, the performance of the product increased. However, the FAR (60% in daily resolution) remains a main challenge.

4.5 Conclusions

In this study, we evaluated and compared the performance of different satellite-based rainfall products over the Pacific coast and Andes of Ecuador. A mesoscale quality-controlled rain radar network was used as the rainfall reference. Statistical comparison indices were used to analyze the performance and to describe different aspects of the satellite-based rainfall products. The first validation was performed at 11 km^2 spatial resolution and at the time of MW overpass for MW-based IMERG, RF-based rainfall, and IR-only IMERG products. Based on the validation, MW-based IMERG and RF-based rainfall provided better rainfall estimates in Ecuador than IR-only IMERG during MW overpasses. The distribution of the evaluation metrics spatially shows the impact of topography and the complex climate zonations in the study region. High precipitation values were better captured by the MW-based IMERG and the RF-based rainfall algorithms. The frequent false alarms are one of the most important issues in all products; FAR decreases with an increasing rainfall rate. Future studies on the lag time are therefore required in order to elucidate the high FAR in the satellite-based products. In the third validation, we investigated regionally calibrated RF-based rainfall products for Ecuador. RF-based rainfall is trained by MW-based IMERG. Although the product shows convincing results at a MW overpass of 11 km^2, the performance decreased by increasing the resolution to 2 km^2 spatial and 30 min temporal resolution. Furthermore, RF-based rainfall is trained to the available microwave-only data from IMERG. Consequently, due to the low temporal resolution of the data from MW satellites, some rainfall events might not have been considered [8].

References

[1] Jochen Seidel et al. "Precipitation Characteristics at Two Locations in the Tropical Andes by Means of Vertically Pointing Micro-Rain Radar Observations". In: *Remote Sensing* 11.24 (2019). ISSN: 2072-4292. DOI: 10.3390/rs11242985. URL: https://www.mdpi.com/2072-4292/11/24/2985.

[2] E Ward et al. "Evaluation of precipitation products over complex mountainous terrain: A water resources perspective". In: *Advances in Water Resources* 34.10 (2011), pp. 1222–1231.

[3] Nazli Turini et al. "Random forest-based rainfall retrieval for Ecuador using GOES-16 and IMERG-V06 data". In: *European Journal of Remote Sensing* 54.1 (2021), pp. 117–139. DOI: 10.1080/22797254.2021.1884002. eprint: https://doi.org/10.1080/22797254.2021.1884002. URL: https://doi.org/10.1080/22797254.2021.1884002.

[4] Jackson Tan, Walter A Petersen, and Ali Tokay. "A novel approach to identify sources of errors in IMERG for GPM ground validation". In: *Journal of Hydrometeorology* 17.9 (2016), pp. 2477–2491.

[5] George J Huffman et al. "NASA global precipitation measurement (GPM) integrated multi-satellite retrievals for GPM (IMERG)". In: *Algorithm theoretical basis document, version* 4 (2015), p. 30.

[6] George J Huffman et al. *The TRMM Multisatellite Precipitation Analysis (TMPA): Quasi-Global, Multiyear, Combined-Sensor Precipitation Estimates at Fine Scales*. 2007.

[7] Willam S Olson, Hirohiko Masunaga, and Combined Radar-Radiometer Algorithm Team Gpm. "GPM combined radar-radiometer precipitation algorithm theoretical basis document (Version 4)". In: *NASA: Washington, DC, USA* (2016).

[8] Nazli Turini, Boris Thies, and Joerg Bendix. "Estimating High Spatio-Temporal Resolution Rainfall from MSG1 and GPM IMERG Based on Machine Learning: Case Study of Iran". In: *Remote Sensing* 11.19 (2019). ISSN: 2072-4292. DOI: 10.3390/rs11192307. URL: https://www.mdpi.com/2072-4292/11/19/2307.

[9] Margaret Wambui Kimani, Joost C B Hoedjes, and Zhongbo Su. "An Assessment of Satellite-Derived Rainfall Products Relative to Ground Observations over East Africa". en. In: *Remote Sensing* 9.5 (May 2017), p. 430.

[10] Meike Kühnlein et al. "Precipitation Estimates from MSG SEVIRI Daytime, Nighttime, and Twilight Data with Random Forests". In: *J. Appl. Meteorol. Climatol.* 53.11 (Nov. 2014), pp. 2457–2480.

[11] Meike Kühnlein et al. "Improving the accuracy of rainfall rates from optical satellite sensors with machine learning—A random forests-based approach applied to MSG SEVIRI". In: *Remote Sens. Environ.* 141 (2014), pp. 129–143.

[12] Christine Kolbe et al. "Precipitation Retrieval over the Tibetan Plateau from the Geostationary Orbit—Part 1: Precipitation Area Delineation with Elektro-L2 and Insat-3D". In: *Remote Sensing* 11.19 (2019). ISSN: 2072-4292. DOI: 10.3390/rs11192302. URL: https://www.mdpi.com/2072-4292/11/19/2302.

[13] Christine Kolbe et al. "Correction: Kolbe, C., et al. Precipitation Retrieval over the Tibetan Plateau from the Geostationary Orbit—Part 2: Precipitation Rates with Elektro-L2 and Insat-3D. Remote Sensing 2020, 12, 2114". In: *Remote Sensing* 12.21 (2020). ISSN: 2072-4292. DOI: 10.3390/rs12213594. URL: https://www.mdpi.com/2072-4292/12/21/3594.

[14] Yang Hong et al. "Precipitation estimation from remotely sensed imagery using an artificial neural network cloud classification system". In: *Journal of Applied Meteorology* 43.12 (2004), pp. 1834–1853.

[15] Bastian Manz et al. "Comparative ground validation of IMERG and TMPA at variable spatiotemporal scales in the tropical Andes". In: *Journal of Hydrometeorology* 18.9 (2017), pp. 2469–2489.

[16] Bolívar Erazo et al. "Validation of Satellite Estimates (Tropical Rainfall Measuring Mission, TRMM) for Rainfall Variability over the Pacific Slope and Coast of Ecuador". In: *Water* 10.2 (2018). ISSN: 2073-4441. DOI: 10.3390/w10020213. URL: https://www.mdpi.com/2073-4441/10/2/213.

[17] Marlon Maranan et al. "A process-based validation of GPM IMERG and its sources using a mesoscale rain gauge network in the West African forest zone". In: *Journal of Hydrometeorology* 21.4 (2020), pp. 729–749.

[18] Nevenka Bulovic, Neil McIntyre, and Fiona Johnson. "Evaluation of IMERG V05B 30-Min Rainfall Estimates over the High-Elevation Tropical Andes Mountains". In: *Journal of Hydrometeorology* 21.12 (2020), pp. 2875–2892.

[19] T Dinku et al. "Validation of satellite rainfall products over East Africa's complex topography". In: *International Journal of Remote Sensing* 28.7 (2007), pp. 1503–1526.

[20] Ross I Maidment et al. "A new, long-term daily satellite-based rainfall dataset for operational monitoring in Africa". In: *Scientific data* 4 (2017), p. 170063.

[21] Jörg Bendix et al. "RadarNet-Sur first weather radar network in tropical high mountains". In: *Bulletin of the American Meteorological Society* 98.6 (2017), pp. 1235–1254.

[22] Rütger Rollenbeck and Jörg Bendix. "Experimental calibration of a cost-effective X-band weather radar for climate ecological studies in southern Ecuador". In: *Atmospheric Research* 79.3-4 (2006), pp. 296–316.

[23] Rütger Rollenbeck and Jörg Bendix. "Rainfall distribution in the Andes of southern Ecuador derived from blending weather radar data and meteorological field observations". In: *Atmospheric Research* 99.2 (2011), pp. 277–289.

[24] Niklas Boers et al. "Complex networks identify spatial patterns of extreme rainfall events of the South American Monsoon System". In: *Geophysical Research Letters* 40.16 (2013), pp. 4386–4392.

[25] Mathias Vuille, Raymond S Bradley, and Frank Keimig. "Climate variability in the Andes of Ecuador and its relation to tropical Pacific and Atlantic sea surface temperature anomalies". In: *Journal of climate* 13.14 (2000), pp. 2520–2535.

[26] Jhan Carlo Espinoza et al. "Rainfall hotspots over the southern tropical Andes: Spatial distribution, rainfall intensity, and relations with large-scale atmospheric circulation". In: *Water Resources Research* 51.5 (2015), pp. 3459–3475.

[27] Bodo Bookhagen and Manfred R Strecker. "Orographic barriers, high-resolution TRMM rainfall, and relief variations along the eastern Andes". In: *Geophysical Research Letters* 35.6 (2008).

[28] George J Huffman et al. "NASA Global Precipitation Measurement (GPM) Integrated Multi-satellitE Retrievals for GPM (IMERG). Algorithm Theoretical Basis Document, Version 06". In: *Algorithm Theoretical Basis Document (ATBD) Version* 4 (2019), p. 26.

[29] Robert J Joyce et al. *CMORPH: A Method that Produces Global Precipitation Estimates from Passive Microwave and Infrared Data at High Spatial and Temporal Resolution*. 2004.

[30] Jackson Tan et al. "Diurnal cycle of IMERG V06 precipitation". In: *Geophysical Research Letters* 46.22 (2019), pp. 13584–13592.

[31] George Huffman. *IMERG V06 quality index*. 2019.

[32] Hans Martin Schulz et al. "Mapping the montane cloud forest of Taiwan using 12 year MODIS-derived ground fog frequency data". en. In: *PLoS One* 12.2 (Feb. 2017), e0172663.

[33] M Min et al. "Estimating Summertime Precipitation from Himawari-8 and Global Forecast System Based on Machine Learning". In: *IEEE Trans. Geosci. Remote Sens.* 57.5 (May 2019), pp. 2557–2570.

[34] GDAL/OGR contributors. *GDAL/OGR Geospatial Data Abstraction software Library*. Open Source Geospatial Foundation. 2020. URL: https://gdal.org.

[35] Guoqiang Tang et al. "Accounting for spatiotemporal errors of gauges: A critical step to evaluate gridded precipitation products". In: *Journal of hydrology* 559 (2018), pp. 294–306.

[36] Jörg Bendix et al. "Formation of convective clouds at the foothills of the tropical eastern Andes (South Ecuador)". In: *Journal of Applied Meteorology and Climatology* 48.8 (2009), pp. 1682–1695.

[37] Yalei You et al. "Time-Lag Correlation Between Passive Microwave Measurements and Surface Precipitation and Its Impact on Precipitation Retrieval Evaluation". In: *Geophysical Research Letters* 46.14 (2019), pp. 8415–8423. DOI: https://doi.org/10.1029/2019GL083426. URL: https://agupubs.onlinelibrary.wiley.com/doi/abs/10.1029/2019GL083426.

[38] Johanna Orellana-Alvear et al. "Analysis of rain types and their Z–R relationships at different locations in the high Andes of southern Ecuador". In: *Journal of Applied Meteorology and Climatology* 56.11 (2017), pp. 3065–3080.

[39] P Hazenberg, H Leijnse, and R Uijlenhoet. "Radar rainfall estimation of stratiform winter precipitation in the Belgian Ardennes". In: *Water Resources Research* 47.2 (2011).

[40] Edouard Goudenhoofdt and Laurent Delobbe. "Generation and verification of rainfall estimates from 10-yr volumetric weather radar measurements". In: *Journal of Hydrometeorology* 17.4 (2016), pp. 1223–1242.

[41] Jonathan G Fairman Jr et al. "A radar-based rainfall climatology of Great Britain and Ireland". In: *Weather* 70.5 (2015), pp. 153–158.

[42] James A Smith et al. "Analyses of a long-term, high-resolution radar rainfall data set for the Baltimore metropolitan region". In: *Water Resources Research* 48.4 (2012).

[43] Veljko Petković and Christian D. Kummerow. "Understanding the Sources of Satellite Passive Microwave Rainfall Retrieval Systematic Errors Over Land". In: *Journal of Applied Meteorology and Climatology* 56.3 (2017), pp. 597–614. DOI: 10.1175/JAMC-D-16-0174.1. URL: https://journals.ametsoc.org/view/journals/apme/56/3/jamc-d-16-0174.1.xml.

[44] Satya Prakash et al. "A preliminary assessment of GPM-based multi-satellite precipitation estimates over a monsoon dominated region". In: *Journal of Hydrology* 556 (2018), pp. 865–876.

[45] Kiyoung Kim et al. "Evaluation of topographical and seasonal feature using GPM IMERG and TRMM 3B42 over Far-East Asia". In: *Atmospheric Research* 187 (2017), pp. 95–105. ISSN: 0169-8095. DOI: https://doi.org/10.1016/j.atmosres.2016.12.007. URL: https://www.sciencedirect.com/science/article/pii/S0169809516306901.

[46] Jackson Tan et al. "Evaluation of Global Precipitation Measurement Rainfall Estimates against Three Dense Gauge Networks". In: *Journal of Hydrometeorology* 19.3 (2018), pp. 517–532. DOI: 10.1175/JHM-D-17-0174.1. URL: https://journals.ametsoc.org/view/journals/hydr/19/3/jhm-d-17-0174_1.xml.

[47] Ulrich Foelsche et al. "Evaluation of GPM IMERG Early, Late, and Final rainfall estimates using WegenerNet gauge data in southeastern Austria". In: *Hydrology and Earth System Sciences* 21.12 (2017), pp. 6559–6572.

[48] Gabriele Villarini and Witold F Krajewski. "Evaluation of the research version TMPA three-hourly 0.25× 0.25 rainfall estimates over Oklahoma". In: *Geophysical Research Letters* 34.5 (2007).

[49] G. T. Ayehu et al. "Validation of new satellite rainfall products over the Upper Blue Nile Basin, Ethiopia". In: *Atmospheric Measurement Techniques* 11.4 (2018), pp. 1921–1936. DOI: 10.5194/amt-11-1921-2018. URL: https://amt.copernicus.org/articles/11/1921/2018/.

[50] N Ghajarnia, A Liaghat, and P Daneshkar Arasteh. "Comparison and evaluation of high resolution precipitation estimation products in Urmia Basin-Iran". In: *Atmospheric Research* 158 (2015), pp. 50–65.

[51] Pari-Sima Katiraie-Boroujerdy et al. "Evaluation of satellite-based precipitation estimation over Iran". In: *Journal of arid environments* 97 (2013), pp. 205–219.

Chapter 5

Conclusions and Outlook

5.1 Conclusions

The research developed a new rainfall retrieval technique using LEO microwave and GEO multispectral satellite data. This project supports water management in areas with sparse ground truth rainfall data. Ground-based rainfall information is hardly accessible in most world regions due to remoteness and complex topography. These challenges impose difficulty on planners and decision-makers in the water management field. For this reason, in many regions, satellite rainfall products are available to receive information on precipitation in space and time [1].

Thus, the main aim of this thesis was to combine the advantages of second-generation GEO systems and the new IMERG product to develop a regionally adapted rainfall retrieval scheme with a high temporal and spatial resolution based on a machine learning algorithm in ungauged areas. This aim was based on four different hypotheses.

Hypothesis 1 states that multispectral GEO IR data and machine learning can improve the newest generation of rainfall products' rainfall retrieval for ungauged regions. Therefore, in the chapter 2 (WP1), a new rainfall retrieval technique was developed for Iran using microwave satellite and MSG1 data. The MW rainfall data from IMERG-V05 was used as a training references in RF models. In this algorithm two models for the rainfall area delineation and rainfall rate assignment were developed using RF. The method was validated against independent microwave-only GPM IMERG rainfall data. The validation results verified Hypothesis 1 with high accuracy. Combining second-generation precipitation radar information with multispectral IR from modern GEO satellites using the machine learning algorithm RF provides a high spatio-temporal resolution of rainfall in Iran. The new

rainfall retrieval performed well in the validation against independent MW-IMERG, particularly compared with the GPM IMERG IR-only rainfall product (Section 2.3.2.3). Also, further validation was performed against daily gauge data. The results showed improvement of rainfall retrieval with the developed rainfall product in high spatio-temporal resolution in comparison with other global products which were evaluated in Iran. This confirmation allowed us to test the second hypothesis.

Hypothesis 2 reads: "The developed algorithm in Hypothesis 1 is transferable with equal accuracy to areas with complex topography and rainfall regimes". Therefore, in chapter 3 (WP2), I investigated the applicability of the developed algorithm in Ecuador to another rainfall regime and geostationary satellite (GOES-16) compared with Iran. So, in this chapter, I developed the rainfall retrieval product for Ecuador using multispectral IR information from GOES-16 and microwave-only data from IMERG-V06 using RF. The MW overpass from IMERG-V06 was used as a reference to train the RF models for rain area delieation and rainfall rate assignment separately. Considering the regional specifications of Ecuador, the feature selection and tuning of the RF models were conducted again. I applied two different validation strategies to estimate the model accuracy: i) The RF-based rainfall product (11 km^2 and 30 minutes) was validated against independent microwave-only IMERG-V06 information; ii) the RF-based rainfall product (2 km^2 and daily) was validated against daily gauge stations. The validation demonstrated that the developed algorithm could retrieve reliable rainfall information in Ecuador more accurately than the IR-only IMERG product (Section 3.3.2 and 3.3.4), confirming the approach's viability and Hypothesis 2. The developed algorithm could be applied in another region with complex topography with equal accuracy. Meanwhile, the spatial variability of the evaluation displays the influence of the topography in Ecuador, where inaccuracy appears in the higher elevations of the Andes (Section 3.3.3). These results might be due to the small-scale regional convective rainfall in more complex regions of Ecuador [2], which are difficult to be capture using GOES data. On the other hand, the detailed analysis of validation results showed that the developed RF models could not capture extreme events (Section 3.3.2). Therefore, Hypotheses 3 and 4 are designed to identify and understand the error source in the developed algorithm.

Hypothesis 3 evaluates whether the accuracy assessment of satellite-based rainfall products is highly dependent on the spatial coverage and resolution of the products. Hypothesis 4 reads: "The main uncertainties in the satellite-based rainfall retrievals are drizzle and extreme rainfall rates, which are difficult to capture." In Chapter

4 (WP3) I validated different satellite-based rainfall products to test Hypotheses 3 and 4. The accuracy of MW-based IMERG compared to RF-based rainfall and IR-only IMERG data was evaluated against high spatio-temporal resolution data from ground-based radar networks and high temporal resolution data from meteorological stations to assess satellite-based rainfall products under climatic and topographic conditions at the time of MW overpass in 11 km^2 (Section 4.2.2.1). Furthermore, I also validated the performance of regionally trained RF-based rainfall models for Ecuador at 30 min and 2 km^2 to evaluate the spatial resolution's impact on the accuracy of satellite-based rainfall products. The validation resulted in different aspects: (i) The spatial resolution significantly impacted the performance of RF-based rainfall even with a regionally trained product. The product performed better at a higher resolution. In order to develop high spatio-temporal resolution rainfall information based on MW data, more frequent temporal MW data must be available; (ii) the RF-based rainfall products in high spatio-temporal resolution (2 km^2) performed better in a lower temporal resolution (Section 4.3.4) (iii) the validation metrics spatial distribution demonstrated the influence of topography and complex climate zonation on the rainfall retrieval accuracy of the study region; (iv) the validation of satellite-based rainfall products against the gauges (Section 4.3.2) showed lower consistency than radar (Section 4.3.1), which might be because convective rainfall in complex terrains could not be captured with the spatial resolution of GOES-16 data accurately. (v) The discrepancy between the RF-based rainfall products and radar data is more evident in higher rainfall rates (Section 4.7 and 4.3.1.2); (vi) the validation showed that around 60% of false alarms and misses are ≤1 mm/h (Section 4.7 and 4.3.1.2).

Evidence from this chapter suggests that the spatial and temporal resolution of the satellite-based rainfall product influences rainfall estimate accuracy. Furthermore, plotting the evaluation metrics spatially made it evident that the same satellite-based product has different accuracy for different topographical and climatic zones (i–iv). Therefore, Hypothesis 3 was confirmed. The aforementioned points (v) and (vi) confirm that the RF-based rainfall product has difficulty detecting extreme rainfall rates and drizzle. Therefore, Hypothesis 4 is acceptable.

In summary, the following contributions and novelties of this thesis are:

(1) The new regionally adapted MW-IR rainfall retrieval algorithm in a high spatio-temporal resolution was developed based on modern GEO multispectral IR data and random forest algorithm for ungauged regions, which overcame

the limitations of previously existing rainfall retrievals relying on ground-based rainfall. Therefore, the developed algorithm is transferable with equal accuracy to areas with different topography and rainfall regimes;

(2) The developed algorithm overcomes limitations in IMERG concerning the application of geostationary IR data;

(3) The source of differences between the developed satellite-based rainfall product and ground measurements was investigated. This validation was performed in a high spatio-temporal resolution (2 km^2 and 30 minutes) against high temporal resolution ground-based radar data and meteorological stations. This method was a novel approach to finding the source of possible errors for further development considering the time of MW overpass. The results confirmed the importance of the availability of high spatio-temporal ground-based rainfall resolutions in validation strategies and showed that the developed algorithms need improvement to cope with very low/high rainfall rates over complex terrains.

5.2 Outlook

The main conclusions of this thesis are summarized in Section 5.1.

After developing this algorithm, potential improvements, including atmospheric parameters as a predictor, should be investigated. This improvement allows us to incorporate regional and seasonal specifications of the area directly into the algorithm. In addition, the impact of climatic zones, climatic dynamics, and topographic situations should be considered in the performance of the new rainfall retrieval technique. The results suggest that the developed algorithms need improvement, particularly to cope with very low/high intensities. Therefore, additional work must be conducted to establish whether another machine learning algorithm, training approach, or data set could be applied to capture drizzle and extreme events over complex regions. We are currently in the process of investigating these aspects with the DFG research project “Dynamics of precipitation in transition: The water source for the Galápagos Archipelago under climate change”.

References

[1] Margaret Wambui Kimani, Joost C. B. Hoedjes, and Zhongbo Su. "An Assessment of Satellite-Derived Rainfall Products Relative to Ground Observations over East Africa". In: *Remote Sensing* 9.5 (2017). ISSN: 2072-4292. DOI: 10.3390/rs9050430. URL: https://www.mdpi.com/2072-4292/9/5/430.

[2] Jörg Bendix et al. "Formation of convective clouds at the foothills of the tropical eastern Andes (South Ecuador)". In: *Journal of Applied Meteorology and Climatology* 48.8 (2009), pp. 1682–1695.

[3] Bateman. *2020 was Earth's 2nd-hottest year, just behind 2016*. https://www.noaa.gov/news/2020-was-earth-s-2nd-hottest-year-just-behind-2016. Accessed 03/06/2021. 2021.

[4] *WORLD DISASTERS REPORT 2020 COME HEAT OR HIGH WATER*. https://media.ifrc.org/ifrc/wp-content/uploads/2020/11/IFRC_wdr2020/20201113_WorldDisasters_1.pdf. 2020.

[5] *Australian wildfires declared among the 'worst wildlife disasters in modern history'*. https://www.nbcnews.com/news/world/australian-wildfires-declared-among-worst-wildlife-disasters-modern-history-n1235071. 2020.

[6] World Health Organization et al. *Water, sanitation, hygiene, and waste management for the COVID-19 virus: interim guidance, 23 April 2020*. Tech. rep. World Health Organization, 2020.

[7] Xuan Phuong Nguyen et al. "Record decline in global CO2 emissions prompted by COVID-19 pandemic and its implications on future climate change policies". In: *Energy Sources, Part A: Recovery, Utilization, and Environmental Effects* (2021), pp. 1–4.

[8] Prajal Pradhan et al. "A Systematic Study of Sustainable Development Goal (SDG) Interactions". In: *Earth's Future* 5.11 (2017), pp. 1169–1179. DOI: https://doi.org/10.1002/2017EF000632. eprint: https://agupubs.onlinelibrary.wiley.com/doi/pdf/10.1002/2017EF000632. URL: https://agupubs.onlinelibrary.wiley.com/doi/abs/10.1002/2017EF000632.

[9] UNESCO. "The United Nations World Water Development Report 2015: Water for a Sustainable World". In: *WWAP (United Nations World Water Assessment Programme)* (2015). eprint: https://www.unwater.org/publications/world-water-development-report-2015/.

[10] Anik Bhaduri et al. "Achieving Sustainable Development Goals from a Water Perspective". In: *Frontiers in Environmental Science* 4 (2016), p. 64. ISSN: 2296-665X. DOI: 10.3389/fenvs.2016.00064. URL: https://www.frontiersin.org/article/10.3389/fenvs.2016.00064.

[11] Wouter Buytaert et al. "Assessment and management of water resources in developing, semi-arid and arid regions". In: *Water Resources Management* 26.4 (2012), pp. 841–844.

[12] Siamak Farrokhzadeh et al. "Sustainable water resources management in an arid area using a coupled optimization-simulation modeling". In: *Water* 12.3 (2020), p. 885.

[13] Wendy Barnaby. "Do nations go to war over water?" In: *Nature* 458.7236 (2009), pp. 282–283.

[14] Waseem Ahmad Qureshi. "International Law and the Threat of Water Wars". In: *Geo. Wash. J. Energy & Envtl. L.* 12 (2021), p. 18.

[15] Mohammed HI Dore. "Climate change and changes in global precipitation patterns: what do we know?" In: *Environment international* 31.8 (2005), pp. 1167–1181.

[16] Christof Lorenz and Harald Kunstmann. "The hydrological cycle in three state-of-the-art reanalyses: Intercomparison and performance analysis". In: *Journal of Hydrometeorology* 13.5 (2012), pp. 1397–1420.

[17] Ali Behrangi et al. "REFAME: Rain Estimation Using Forward-Adjusted Advection of Microwave Estimates". In: *Journal of Hydrometeorology* 11.6 (2010), pp. 1305–1321. DOI: 10.1175/2010JHM1248.1. URL: https://journals.ametsoc.org/view/journals/hydr/11/6/2010jhm1248_1.xml.

[18] U.S. Geological Survey. *Global 30 Arc-Second Elevation (GTOPO30)*. 30.

[19] Boris Thies, Thomas Nauß, and Jörg Bendix. "Precipitation process and rainfall intensity differentiation using Meteosat Second Generation Spinning Enhanced Visible and Infrared Imager data". In: *J. Geophys. Res.* 113.D23 (Dec. 2008), p. 1121.

[20] Sebastian Egli, Boris Thies, and Jörg Bendix. “A Hybrid Approach for Fog Retrieval Based on a Combination of Satellite and Ground Truth Data”. en. In: *Remote Sensing* 10.4 (Apr. 2018), p. 628.

[21] Guoqiang Tang et al. “Accounting for spatiotemporal errors of gauges: A critical step to evaluate gridded precipitation products”. In: *Journal of hydrology* 559 (2018), pp. 294–306.

[22] Pari-Sima Katiraie-Boroujerdy et al. “Trends of precipitation extreme indices over a subtropical semi-arid area using PERSIANN-CDR”. en. In: *Theor. Appl. Climatol.* 130.1-2 (Oct. 2017), pp. 249–260.

[23] Apostolos Giannakos and Haralambos Feidas. “Classification of convective and stratiform rain based on the spectral and textural features of Meteosat Second Generation infrared data”. In: *Theoretical and applied climatology* 113.3-4 (2013), pp. 495–510.

[24] Yang Hong et al. “Precipitation estimation from remotely sensed imagery using an artificial neural network cloud classification system”. In: *Journal of Applied Meteorology* 43.12 (2004), pp. 1834–1853.

[25] Vladimir Svetnik et al. “Random forest: a classification and regression tool for compound classification and QSAR modeling”. In: *Journal of chemical information and computer sciences* 43.6 (2003), pp. 1947–1958.

[26] Tanvir Islam et al. “Non-parametric rain/no rain screening method for satellite-borne passive microwave radiometers at 19–85 GHz channels with the Random Forests algorithm”. In: *International journal of remote sensing* 35.9 (2014), pp. 3254–3267.

[27] G Rivolta et al. “Artificial neural-network technique for precipitation nowcasting from satellite imagery”. In: *Advances in Geosciences* 7 (2006), pp. 97–103.

[28] Kou-lin Hsu et al. “Precipitation estimation from remotely sensed information using artificial neural networks”. In: *Journal of Applied Meteorology* 36.9 (1997), pp. 1176–1190.

[29] FJ Tapiador et al. “Neural networks in satellite rainfall estimation”. In: *Meteorological Applications* 11.1 (2004), pp. 83–91.

[30] DIF Grimes et al. "A neural network approach to real-time rainfall estimation for Africa using satellite data". In: *Journal of Hydrometeorology* 4.6 (2003), pp. 1119–1133.

[31] J Lelieveld et al. "Climate change and impacts in the Eastern Mediterranean and the Middle East". en. In: *Clim. Change* 114.3-4 (Mar. 2012), pp. 667–687.

[32] Jan Cermak and Jörg Bendix. "A novel approach to fog/low stratus detection using Meteosat 8 data". In: *Atmos. Res.* 87.3 (Mar. 2008), pp. 279–292.

[33] Toshiyuki Kurino. *A satellite infrared technique for estimating "deep/shallow" precipitation.* 1997.

[34] R J Hijmans, S E Cameron, J L Parra, et al. "Very high resolution interpolated climate surfaces for global land areas". In: *J. Appl. Meteorol. Climatol.* (2005).

[35] Margaret Wambui Kimani, Joost C B Hoedjes, and Zhongbo Su. "An Assessment of Satellite-Derived Rainfall Products Relative to Ground Observations over East Africa". en. In: *Remote Sensing* 9.5 (May 2017), p. 430.

[36] Meike Kühnlein et al. "Improving the accuracy of rainfall rates from optical satellite sensors with machine learning—A random forests-based approach applied to MSG SEVIRI". In: *Remote Sens. Environ.* 141 (2014), pp. 129–143.

[37] Bruno Collischonn, Walter Collischonn, and Carlos Eduardo Morelli Tucci. "Daily hydrological modeling in the Amazon basin using TRMM rainfall estimates". In: *Journal of Hydrology* 360.1-4 (2008), pp. 207–216.

[38] Zengxin Zhang et al. "Hydrologic Evaluation of TRMM and GPM IMERG Satellite-Based Precipitation in a Humid Basin of China". In: *Remote Sensing* 11.4 (2019), p. 431.

[39] Xian Luo et al. "Hydrological Simulation Using TRMM and CHIRPS Precipitation Estimates in the Lower Lancang-Mekong River Basin". In: *Chinese geographical science* 29.1 (2019), pp. 13–25.

[40] George J Huffman et al. "NASA global precipitation measurement (GPM) integrated multi-satellite retrievals for GPM (IMERG)". In: *Algorithm theoretical basis document, version* 4 (2015), p. 30.

[41] Ornl Daac. "Spatial Data Access Tool (SDAT)". In: *ORNL DAAC* (May 2017).

[42] Viviana Maggioni and Christian Massari. "On the performance of satellite precipitation products in riverine flood modeling: A review". In: *Journal of hydrology* 558 (2018), pp. 214–224.

[43] Ali Behrangi et al. *PERSIANN-MSA: A Precipitation Estimation Method from Satellite-Based Multispectral Analysis*. 2009.

[44] Tayeb Raziei et al. *Spatial Patterns and Temporal Variability of Drought in Western Iran*. 2009.

[45] Trevor Hastie, Robert Tibshirani, and Jerome Friedman. *The elements of statistical learning: data mining, inference, and prediction, Springer Series in Statistics*. 2009.

[46] *Website*. (https://webmap.ornl.gov/ogc/dataset.jsp?dg_id=10003_1). Accessed: 2019-7-9.

[47] Soroosh Sorooshian et al. *Evaluation of PERSIANN System Satellite–Based Estimates of Tropical Rainfall*. 2000.

[48] Mohammed H I Dore. "Climate change and changes in global precipitation patterns: what do we know?" en. In: *Environ. Int.* 31.8 (Oct. 2005), pp. 1167–1181.

[49] Leo Breiman. "Random Forests". In: *Mach. Learn.* 45.1 (Oct. 2001), pp. 5–32.

[50] Michael R Chernick. *Bootstrap Methods: A Guide for Practitioners and Researchers*. en. John Wiley & Sons, Sept. 2011.

[51] Johannes Schmetz et al. "AN INTRODUCTION TO METEOSAT SECOND GENERATION (MSG)". In: *Bull. Am. Meteorol. Soc.* 83.7 (July 2002), pp. 977–992.

[52] ORNL DAAC. *Spatial Data Access Tool (SDAT)*. 2017.

[53] S Finkensieper et al. *CLAAS-2: CM SAF CLoud property dAtAset using SEVIRI–Edition 2, Satellite Application Facility on Climate Monitoring*. 2016.

[54] Ehsan Sharifi, Reinhold Steinacker, and Bahram Saghafian. *Assessment of GPM-IMERG and Other Precipitation Products against Gauge Data under Different Topographic and Climatic Conditions in Iran: Preliminary Results*. 2016.

[55] B Thies, T Nauss, and J Bendix. *First results on a process-oriented rain area classification technique using Meteosat Second Generation SEVIRI nighttime data*. 2008.

[56] Willam S Olson, Hirohiko Masunaga, and Combined Radar-Radiometer Algorithm Team Gpm. "GPM combined radar-radiometer precipitation algorithm theoretical basis document (Version 4)". In: *NASA: Washington, DC, USA* (2016).

[57] Haralambos Feidas and Apostolos Giannakos. "Classifying convective and stratiform rain using multispectral infrared Meteosat Second Generation satellite data". en. In: *Theor. Appl. Climatol.* 108.3-4 (May 2012), pp. 613–630.

[58] M J Amiri and S S Eslamian. *Investigation of Climate Change in Iran*. 2010.

[59] Mohammadali Alijanian et al. "Evaluation of satellite rainfall climatology using CMORPH, PERSIANN-CDR, PERSIANN, TRMM, MSWEP over Iran". In: *Int. J. Climatol.* 37.14 (2017), pp. 4896–4914.

[60] Hanna Meyer, Johannes Drönner, and Thomas Nauss. *Satellite based high resolution mapping of rainfall over Southern Africa*. 2017.

[61] M R P Sapiano and P A Arkin. *An Intercomparison and Validation of High-Resolution Satellite Precipitation Estimates with 3-Hourly Gauge Data*. 2009.

[62] Robert J Joyce et al. *CMORPH: A Method that Produces Global Precipitation Estimates from Passive Microwave and Infrared Data at High Spatial and Temporal Resolution*. 2004.

[63] Apostolos Giannakos and Haralambos Feidas. "Classification of convective and stratiform rain based on the spectral and textural features of Meteosat Second Generation infrared data". en. In: *Theor. Appl. Climatol.* 113.3-4 (Aug. 2013), pp. 495–510.

[64] M Min et al. "Estimating Summertime Precipitation from Himawari-8 and Global Forecast System Based on Machine Learning". In: *IEEE Trans. Geosci. Remote Sens.* 57.5 (May 2019), pp. 2557–2570.

[65] V Levizzani, P Bauer, and F Joseph Turk. *Measuring Precipitation from Space: EURAINSAT and the Future*. en. Springer Science & Business Media, May 2007.

[66] George J Huffman et al. *The TRMM Multisatellite Precipitation Analysis (TMPA): Quasi-Global, Multiyear, Combined-Sensor Precipitation Estimates at Fine Scales*. 2007.

[67] *Bootstrap Methods: A Guide for Practitioners and Researchers by CHERNICK, M. R.* 2008.

[68] G Heinemann et al. *Investigation of summertime convective rainfall in Western Europe based on a synergy of remote sensing data and numerical models*. 2001.

[69] Pari-Sima Katiraie-Boroujerdy et al. *Intercomparison of PERSIANN-CDR and TRMM-3B42V7 precipitation estimates at monthly and daily time scales*. 2017.

[70] S Javanmard et al. *Comparing high-resolution gridded precipitation data with satellite rainfall estimates of TRMM_3B42 over Iran*. 2010.

[71] Pari-Sima Katiraie-Boroujerdy et al. "Evaluation of satellite-based precipitation estimation over Iran". In: *J. Arid Environ.* 97 (Oct. 2013), pp. 205–219.

[72] D Capacci and BJ Conway. "Delineation of precipitation areas from MODIS visible and infrared imagery with artificial neural networks". In: *Meteorological Applications* 12.4 (2005), pp. 291–305.

[73] Hanna Meyer et al. "Comparison of four machine learning algorithms for their applicability in satellite-based optical rainfall retrievals". In: *Atmospheric research* 169 (2016), pp. 424–433.

[74] Saber Moazami et al. "Comparison of PERSIANN and V7 TRMM Multi-satellite Precipitation Analysis (TMPA) products with rain gauge data over Iran". In: *Int. J. Remote Sens.* 34.22 (Nov. 2013), pp. 8156–8171.

[75] Arthur Y Hou et al. "The Global Precipitation Measurement Mission". In: *Bull. Am. Meteorol. Soc.* 95.5 (May 2014), pp. 701–722.

[76] Markus Kottek et al. "World Map of the Köppen-Geiger climate classification updated". In: *Meteorol. Z.* 15.3 (2006), pp. 259–263.

[77] Hans Martin Schulz et al. "Mapping the montane cloud forest of Taiwan using 12 year MODIS-derived ground fog frequency data". en. In: *PLoS One* 12.2 (Feb. 2017), e0172663.

[78] C Kidd and V Levizzani. *Status of satellite precipitation retrievals*. 2011.

[79] Abolghasem Akbari et al. "Validation of TRMM 3B42 V6 for estimation of mean annual rainfall over ungauged area in semiarid climate". en. In: *Environ. Earth Sci.* 76.15 (Aug. 2017), p. 537.

[80] Meike Kühnlein et al. "Precipitation Estimates from MSG SEVIRI Daytime, Nighttime, and Twilight Data with Random Forests". In: *J. Appl. Meteorol. Climatol.* 53.11 (Nov. 2014), pp. 2457–2480.

[81] Johannes Drönner et al. "FFLSD - Fast Fog and Low Stratus Detection tool for large satellite time-series". In: *Comput. Geosci.* 128 (July 2019), pp. 51–59.

[82] Reza Modarres and Ali Sarhadi. *Rainfall trends analysis of Iran in the last half of the twentieth century.* 2009.

[83] Gareth James et al. *An Introduction to Statistical Learning: with Applications in R.* en. Springer Science & Business Media, June 2013.

[84] Hanqing Chen et al. *Impact of the crucial geographic and climatic factors on the input source errors of GPM-based global satellite precipitation estimates.* 2019.

[85] S Egli et al. "A 10 year fog and low stratus climatology for Europe based on Meteosat Second Generation data". In: *Q.J.R. Meteorol. Soc.* 143.702 (Jan. 2017), pp. 530–541.

[86] Reza Modarres and Vicente de Paulo Rodrigues da Silva. *Rainfall trends in arid and semi-arid regions of Iran.* 2007.

[87] F Pedregosa et al. "Scikit-learn: Machine Learning in Python". In: *J. Mach. Learn. Res.* 12 (2011), pp. 2825–2830.

[88] N Ghajarnia, A Liaghat, and P Daneshkar Arasteh. *Comparison and evaluation of high resolution precipitation estimation products in Urmia Basin-Iran.* 2015.

[89] GJ Huffman et al. *NASA Global Precipitation Measurement (GPM) Integrated Multi-satellitE Retrievals for GPM (IMERG) Algorithm Theoretical Basis Document (ATBD) Version 5.2. 2018.* 2011.

[90] GJ Huffman. *IMERG Quality Index.* 2018.

[91] GROWnet. en. Dec. 2017. URL: https://bmbf-grow.de/en/grow-projects/sawam (visited on 09/26/2021).

[92] Jochen Seidel et al. "Precipitation Characteristics at Two Locations in the Tropical Andes by Means of Vertically Pointing Micro-Rain Radar Observations". In: *Remote Sensing* 11.24 (2019). ISSN: 2072-4292. DOI: 10.3390/rs11242985. URL: https://www.mdpi.com/2072-4292/11/24/2985.

[93] Wouter Buytaert et al. "Spatial and temporal rainfall variability in mountainous areas: A case study from the south Ecuadorian Andes". In: *Journal of hydrology* 329.3-4 (2006), pp. 413–421.

[94] Boris F Ochoa-Tocachi et al. "Impacts of land use on the hydrological response of tropical Andean catchments". In: *Hydrological Processes* 30.22 (2016), pp. 4074–4089.

[95] Rütger Rollenbeck and Jörg Bendix. "Rainfall distribution in the Andes of southern Ecuador derived from blending weather radar data and meteorological field observations". In: *Atmospheric Research* 99.2 (2011), pp. 277–289. ISSN: 0169-8095. DOI: https://doi.org/10.1016/j.atmosres.2010.10.018. URL: https://www.sciencedirect.com/science/article/pii/S0169809510002826.

[96] Robert F. Adler et al. "Estimation of Monthly Rainfall over Japan and Surrounding Waters from a Combination of Low-Orbit Microwave and Geosynchronous IR Data". In: *Journal of Applied Meteorology and Climatology* 32.2 (1993), pp. 335–356. DOI: 10.1175/1520-0450(1993)032<0335:EOMROJ>2.0.CO;2. URL: https://journals.ametsoc.org/view/journals/apme/32/2/1520-0450_1993_032_0335_eomroj_2_0_co_2.xml.

[97] Christian Kummerow and Louis Giglio. "A method for combining passive microwave and infrared rainfall observations". In: *Journal of Atmospheric and Oceanic Technology* 12.1 (1995), pp. 33–45.

[98] Liming Xu et al. "A Microwave Infrared Threshold Technique to Improve the GOES Precipitation Index". In: *Journal of Applied Meteorology* 38.5 (1999), pp. 569–579. DOI: 10.1175/1520-0450(1999)038<0569:AMITTT>2.0.CO;2. URL: https://journals.ametsoc.org/view/journals/apme/38/5/1520-0450_1999_038_0569_amittt_2.0.co_2.xml.

[99] Chris Kidd et al. "Satellite rainfall estimation using combined passive microwave and infrared algorithms". In: *Journal of Hydrometeorology* 4.6 (2003), pp. 1088–1104.

[100] Robert J. Kuligowski. "A Self-Calibrating Real-Time GOES Rainfall Algorithm for Short-Term Rainfall Estimates". In: *Journal of Hydrometeorology* 3.2 (2002), pp. 112–130. DOI: 10.1175/1525-7541(2002)003<0112:ASCRTG>2.0.CO;2. URL: https://journals.ametsoc.org/view/journals/hydr/3/2/1525-7541_2002_003_0112_ascrtg_2_0_co_2.xml.

[101] S. W. Miller, P. A. Arkin, and R. Joyce. "A combined microwave/infrared rain rate algorithm". In: *International Journal of Remote Sensing* 22.17 (2001), pp. 3285–3307. DOI: 10.1080/01431160152609155. eprint: https://doi.org/10.1080/01431160152609155. URL: https://doi.org/10.1080/01431160152609155.

[102] Gilberto A Vicente, Roderick A Scofield, and W Paul Menzel. "The operational GOES infrared rainfall estimation technique". In: *Bulletin of the American Meteorological Society* 79.9 (1998), pp. 1883–1898.

[103] Fengrui Chen and Xi Li. "Evaluation of IMERG and TRMM 3B43 monthly precipitation products over mainland China". In: *Remote Sensing* 8.6 (2016), p. 472.

[104] Hao Guo et al. "Early assessment of integrated multi-satellite retrievals for global precipitation measurement over China". In: *Atmospheric Research* 176 (2016), pp. 121–133.

[105] Na Li et al. "Statistical assessment and hydrological utility of the latest multi-satellite precipitation analysis IMERG in Ganjiang River basin". In: *Atmospheric research* 183 (2017), pp. 212–223.

[106] Bastian Manz et al. "Comparative ground validation of IMERG and TMPA at variable spatiotemporal scales in the tropical Andes". In: *Journal of Hydrometeorology* 18.9 (2017), pp. 2469–2489.

[107] Satya Prakash et al. "From TRMM to GPM: How well can heavy rainfall be detected from space?" In: *Advances in Water Resources* 88 (2016), pp. 1–7. ISSN: 0309-1708. DOI: https://doi.org/10.1016/j.advwatres.2015.11.008. URL: https://www.sciencedirect.com/science/article/pii/S0309170815002675.

[108] E Ward et al. "Evaluation of precipitation products over complex mountainous terrain: A water resources perspective". In: *Advances in Water Resources* 34.10 (2011), pp. 1222–1231.

[109] Bolívar Erazo et al. "Validation of Satellite Estimates (Tropical Rainfall Measuring Mission, TRMM) for Rainfall Variability over the Pacific Slope and Coast of Ecuador". In: *Water* 10.2 (2018). ISSN: 2073-4441. DOI: 10.3390/w10020213. URL: https://www.mdpi.com/2073-4441/10/2/213.

[110] John T. Abatzoglou, Kelly T. Redmond, and Laura M. Edwards. "Classification of Regional Climate Variability in the State of California". In: *Journal of Applied Meteorology and Climatology* 48.8 (2009), pp. 1527–1541. DOI: 10.1175/2009JAMC2062.1. URL: https://journals.ametsoc.org/view/journals/apme/48/8/2009jamc2062.1.xml.

[111] Yagmur Derin et al. "Multiregional satellite precipitation products evaluation over complex terrain". In: *Journal of Hydrometeorology* 17.6 (2016), pp. 1817–1836.

[112] Frédéric Satgé et al. "Assessment of satellite rainfall products over the Andean plateau". In: *Atmospheric Research* 167 (2016), pp. 1–14.

[113] C Kidd et al. "Intercomparison of high-resolution precipitation products over northwest Europe". In: *Journal of Hydrometeorology* 13.1 (2012), pp. 67–83.

[114] Eni G Njoku. *Encyclopedia of Remote Sensing*. 2014.

[115] Veljko Petković and Christian D. Kummerow. "Understanding the Sources of Satellite Passive Microwave Rainfall Retrieval Systematic Errors Over Land". In: *Journal of Applied Meteorology and Climatology* 56.3 (2017), pp. 597–614. DOI: 10.1175/JAMC-D-16-0174.1. URL: https://journals.ametsoc.org/view/journals/apme/56/3/jamc-d-16-0174.1.xml.

[116] C. Kidd. *Satellite rainfall climatology: a review*. 2001. DOI: https://doi.org/10.1002/joc.635. eprint: https://rmets.onlinelibrary.wiley.com/doi/pdf/10.1002/joc.635. URL: https://rmets.onlinelibrary.wiley.com/doi/abs/10.1002/joc.635.

[117] H. Meyer, J. Drönner, and T. Nauss. "Satellite-based high-resolution mapping of rainfall over southern Africa". In: *Atmospheric Measurement Techniques* 10.6 (2017), pp. 2009–2019. DOI: 10.5194/amt-10-2009-2017. URL: https://amt.copernicus.org/articles/10/2009/2017/.

[118] Andrew Heidinger. *Algorithm theoretical basis document: ABI cloud mask*. University of Wisconsin–Madison, 2011.

[119] George Huffman. *IMERG V06 quality index*. 2019.

[120] Arthur Y Hou et al. "The global precipitation measurement mission". In: *Bulletin of the American Meteorological Society* 95.5 (2014), pp. 701–722.

[121] Steven J Goodman. "GOES-R series introduction". In: *The GOES-R Series*. Elsevier, 2020, pp. 1–3.

[122] Timothy J Schmit et al. "A closer look at the ABI on the GOES-R series". In: *Bulletin of the American Meteorological Society* 98.4 (2017), pp. 681–698.

[123] T Inoue. "On the temperature measurements and effective cirrus emissivity clouds by window determination region of semi-transparent in the". In: *J. Meteorol. Soc. Jpn* 63 (1985), pp. 88–99.

[124] Itamar M Lensky and Daniel Rosenfeld. "A night-rain delineation algorithm for infrared satellite data based on microphysical considerations". In: *Journal of Applied Meteorology* 42.9 (2003), pp. 1218–1226.

[125] SC Ou et al. "Remote sensing of cirrus cloud parameters using advanced very-high-resolution radiometer 3.7-and 10.9-μm channels". In: *Applied Optics* 32.12 (1993), pp. 2171–2180.

[126] Robert S Stone et al. "The remote sensing of thin cirrus cloud using satellites, lidar and radiative transfer theory". In: *Journal of Applied Meteorology and Climatology* 29.5 (1990), pp. 353–366.

[127] Kathleen I Strabala, Steven A Ackerman, and W Paul Menzel. "Cloud Properties inferred from 8 12-μm Data". In: *Journal of Applied Meteorology and Climatology* 33.2 (1994), pp. 212–229.

[128] Christine Kolbe et al. "Precipitation Retrieval over the Tibetan Plateau from the Geostationary Orbit—Part 1: Precipitation Area Delineation with Elektro-L2 and Insat-3D". In: *Remote Sensing* 11.19 (2019). ISSN: 2072-4292. DOI: 10.3390/rs11192302. URL: https://www.mdpi.com/2072-4292/11/19/2302.

[129] Christine Kolbe et al. "Correction: Kolbe, C., et al. Precipitation Retrieval over the Tibetan Plateau from the Geostationary Orbit—Part 2: Precipitation Rates with Elektro-L2 and Insat-3D. Remote Sensing 2020, 12, 2114". In: *Remote Sensing* 12.21 (2020). ISSN: 2072-4292. DOI: 10.3390/rs12213594. URL: https://www.mdpi.com/2072-4292/12/21/3594.

[130] Nazli Turini, Boris Thies, and Joerg Bendix. "Estimating High Spatio-Temporal Resolution Rainfall from MSG1 and GPM IMERG Based on Machine Learning: Case Study of Iran". In: *Remote Sensing* 11.19 (2019). ISSN: 2072-4292. DOI: 10.3390/rs11192307. URL: https://www.mdpi.com/2072-4292/11/19/2307.

[131] Martin G. Schultz et al. "Tropospheric Ozone Assessment Report: Database and metrics data of global surface ozone observations". In: *Elementa* 5 (2017). ISSN: 23251026. DOI: 10.1525/elementa.244.

[132] T Dinku et al. "Validation of satellite rainfall products over East Africa's complex topography". In: *International Journal of Remote Sensing* 28.7 (2007), pp. 1503–1526.

[133] M Neteler et al. *GRASS GIS: A multi-purpose Open Source GIS. Environmental Modeling and Software (31): 124–130*. 2012.

[134] Olaf Conrad et al. "System for automated geoscientific analyses (SAGA) v. 2.1. 4". In: *Geoscientific Model Development* 8.7 (2015), pp. 1991–2007.

[135] T Dinku et al. "Validation of high-resolution satellite rainfall products over complex terrain". In: *International Journal of Remote Sensing* 29.14 (2008), pp. 4097–4110.

[136] Jackson Tan et al. "Diurnal cycle of IMERG V06 precipitation". In: *Geophysical Research Letters* 46.22 (2019), pp. 13584–13592.

[137] George J Huffman et al. "NASA Global Precipitation Measurement (GPM) Integrated Multi-satellitE Retrievals for GPM (IMERG). Algorithm Theoretical Basis Document, Version 06". In: *Algorithm Theoretical Basis Document (ATBD) Version* 4 (2019), p. 26.

[138] John D Hunter. "Matplotlib: A 2D graphics environment". In: *Computing in science & engineering* 9.03 (2007), pp. 90–95.

[139] Marlon Maranan et al. "A process-based validation of GPM IMERG and its sources using a mesoscale rain gauge network in the West African forest zone". In: *Journal of Hydrometeorology* 21.4 (2020), pp. 729–749.

[140] Jörg Bendix et al. "RadarNet-Sur first weather radar network in tropical high mountains". In: *Bulletin of the American Meteorological Society* 98.6 (2017), pp. 1235–1254.

[141] Ricardo Zubieta et al. "Hydrological modeling of the Peruvian–Ecuadorian Amazon Basin using GPM-IMERG satellite-based precipitation dataset". In: *Hydrology and Earth System Sciences* 21.7 (2017), pp. 3543–3555.

[142] Ravinesh C Deo and Mehmet Şahin. "Application of the extreme learning machine algorithm for the prediction of monthly Effective Drought Index in eastern Australia". In: *Atmospheric Research* 153 (2015), pp. 512–525.

[143] Nazli Turini et al. "Random forest-based rainfall retrieval for Ecuador using GOES-16 and IMERG-V06 data". In: *European Journal of Remote Sensing* 54.1 (2021), pp. 117–139. DOI: 10.1080/22797254.2021.1884002. eprint: https://doi.org/10.1080/22797254.2021.1884002. URL: https://doi.org/10.1080/22797254.2021.1884002.

[144] Jackson Tan, Walter A Petersen, and Ali Tokay. "A novel approach to identify sources of errors in IMERG for GPM ground validation". In: *Journal of Hydrometeorology* 17.9 (2016), pp. 2477–2491.

[145] Nevenka Bulovic, Neil McIntyre, and Fiona Johnson. "Evaluation of IMERG V05B 30-Min Rainfall Estimates over the High-Elevation Tropical Andes Mountains". In: *Journal of Hydrometeorology* 21.12 (2020), pp. 2875–2892.

[146] Ross I Maidment et al. "A new, long-term daily satellite-based rainfall dataset for operational monitoring in Africa". In: *Scientific data* 4 (2017), p. 170063.

[147] Rütger Rollenbeck and Jörg Bendix. "Experimental calibration of a cost-effective X-band weather radar for climate ecological studies in southern Ecuador". In: *Atmospheric Research* 79.3-4 (2006), pp. 296–316.

[148] Rütger Rollenbeck and Jörg Bendix. "Rainfall distribution in the Andes of southern Ecuador derived from blending weather radar data and meteorological field observations". In: *Atmospheric Research* 99.2 (2011), pp. 277–289.

[149] Mathias Vuille, Raymond S Bradley, and Frank Keimig. "Climate variability in the Andes of Ecuador and its relation to tropical Pacific and Atlantic sea surface temperature anomalies". In: *Journal of climate* 13.14 (2000), pp. 2520–2535.

[150] Niklas Boers et al. "Complex networks identify spatial patterns of extreme rainfall events of the South American Monsoon System". In: *Geophysical Research Letters* 40.16 (2013), pp. 4386–4392.

[151] Jhan Carlo Espinoza et al. "Rainfall hotspots over the southern tropical Andes: Spatial distribution, rainfall intensity, and relations with large-scale atmospheric circulation". In: *Water Resources Research* 51.5 (2015), pp. 3459–3475.

[152] Bodo Bookhagen and Manfred R Strecker. "Orographic barriers, high-resolution TRMM rainfall, and relief variations along the eastern Andes". In: *Geophysical Research Letters* 35.6 (2008).

[153] Ulrike Romatschke and Robert A Houze Jr. "Extreme summer convection in South America". In: *Journal of Climate* 23.14 (2010), pp. 3761–3791.

[154] GDAL/OGR contributors. *GDAL/OGR Geospatial Data Abstraction software Library*. Open Source Geospatial Foundation. 2020. URL: https://gdal.org.

[155] Johanna Orellana-Alvear et al. "Analysis of rain types and their Z–R relationships at different locations in the high Andes of southern Ecuador". In: *Journal of Applied Meteorology and Climatology* 56.11 (2017), pp. 3065–3080.

[156] P Hazenberg, H Leijnse, and R Uijlenhoet. "Radar rainfall estimation of stratiform winter precipitation in the Belgian Ardennes". In: *Water Resources Research* 47.2 (2011).

[157] Edouard Goudenhoofdt and Laurent Delobbe. "Generation and verification of rainfall estimates from 10-yr volumetric weather radar measurements". In: *Journal of Hydrometeorology* 17.4 (2016), pp. 1223–1242.

[158] Jonathan G Fairman Jr et al. "A radar-based rainfall climatology of Great Britain and Ireland". In: *Weather* 70.5 (2015), pp. 153–158.

[159] James A Smith et al. "Analyses of a long-term, high-resolution radar rainfall data set for the Baltimore metropolitan region". In: *Water Resources Research* 48.4 (2012).

[160] Kiyoung Kim et al. "Evaluation of topographical and seasonal feature using GPM IMERG and TRMM 3B42 over Far-East Asia". In: *Atmospheric Research* 187 (2017), pp. 95–105. ISSN: 0169-8095. DOI: https://doi.org/10.1016/j.atmosres.2016.12.007. URL: https://www.sciencedirect.com/science/article/pii/S0169809516306901.

[161] Satya Prakash et al. "A preliminary assessment of GPM-based multi-satellite precipitation estimates over a monsoon dominated region". In: *Journal of Hydrology* 556 (2018), pp. 865–876.

[162] Jackson Tan et al. "Evaluation of Global Precipitation Measurement Rainfall Estimates against Three Dense Gauge Networks". In: *Journal of Hydrometeorology* 19.3 (2018), pp. 517–532. DOI: 10.1175/JHM-D-17-0174.1. URL: https://journals.ametsoc.org/view/journals/hydr/19/3/jhm-d-17-0174_1.xml.

[163] Ulrich Foelsche et al. "Evaluation of GPM IMERG Early, Late, and Final rainfall estimates using WegenerNet gauge data in southeastern Austria". In: *Hydrology and Earth System Sciences* 21.12 (2017), pp. 6559–6572.

[164] Gabriele Villarini and Witold F Krajewski. "Evaluation of the research version TMPA three-hourly 0.25× 0.25 rainfall estimates over Oklahoma". In: *Geophysical Research Letters* 34.5 (2007).

[165] Yalei You et al. "Time-Lag Correlation Between Passive Microwave Measurements and Surface Precipitation and Its Impact on Precipitation Retrieval Evaluation". In: *Geophysical Research Letters* 46.14 (2019), pp. 8415–8423. DOI: https://doi.org/10.1029/2019GL083426. URL: https://agupubs.onlinelibrary.wiley.com/doi/abs/10.1029/2019GL083426.

[166] G. T. Ayehu et al. "Validation of new satellite rainfall products over the Upper Blue Nile Basin, Ethiopia". In: *Atmospheric Measurement Techniques* 11.4 (2018), pp. 1921–1936. DOI: 10.5194/amt-11-1921-2018. URL: https://amt.copernicus.org/articles/11/1921/2018/.

[167] Pari-Sima Katiraie-Boroujerdy et al. "Evaluation of satellite-based precipitation estimation over Iran". In: *Journal of arid environments* 97 (2013), pp. 205–219.

[168] N Ghajarnia, A Liaghat, and P Daneshkar Arasteh. "Comparison and evaluation of high resolution precipitation estimation products in Urmia Basin-Iran". In: *Atmospheric Research* 158 (2015), pp. 50–65.

[169] C. Kummerow. "The evolution of the Goddard profiling algorithm (GPROF) for rainfall estimation from passive microwave sensors". In: *J. Appl. Meteor.* 40 (2001), pp. 1801–1820.

[170] C. Kummerow et al. "An observationally generated a priori database for microwave rainfall retrievals". In: *J. Atmos. Oceanic Technol.* 28 (2011), pp. 113–130.

[171] C. Kummerow et al. "The evolution of the Goddard Profiling algorithm to a fully parametric scheme". In: *J. Atmos. Oceanic Technol.* 32 (2015), pp. 2265–2280.

[172] R. F. Adler. "The version-2 Global Precipitation Climatology Project (GPCP) monthly precipitation analysis (1979–present)". In: *J. Hydrometeor.* 4 (2003), pp. 1147–1167.

[173] Robert J Joyce and Pingping Xie. "Kalman filter–based CMORPH". In: *Journal of Hydrometeorology* 12.6 (2011), pp. 1547–1563.

[174] Phu Nguyen et al. "The PERSIANN family of global satellite precipitation data: A review and evaluation of products". In: *Hydrology and Earth System Sciences* 22.11 (2018), pp. 5801–5816.

[175] James P Hollinger, James L Peirce, and Gene A Poe. "SSM/I instrument evaluation". In: *IEEE Transactions on Geoscience and Remote Sensing* 28.5 (1990), pp. 781–790.

[176] Toneo Kawanishi et al. "The Advanced Microwave Scanning Radiometer for the Earth Observing System (AMSR-E), NASDA's contribution to the EOS for global energy and water cycle studies". In: *IEEE Transactions on Geoscience and Remote Sensing* 41.2 (2003), pp. 184–194.

[177] Martin C Todd et al. "A combined satellite infrared and passive microwave technique for estimation of small-scale rainfall". In: *Journal of Atmospheric and Oceanic Technology* 18.5 (2001), pp. 742–755.

[178] David W. Martin et al. "Estimates of daily rainfall over the Amazon Basin". In: 95.D10 (Sept. 1990), pp. 17, 043–17, 050. DOI: 10.1029/JD095iD10p17043.

[179] Joseph L Awange et al. "Uncertainties in remotely sensed precipitation data over Africa". In: *International Journal of Climatology* 36.1 (2016), pp. 303–323.

[180] Christopher Daly et al. "High-resolution precipitation mapping in a mountainous watershed: ground truth for evaluating uncertainty in a national precipitation dataset". In: *International Journal of Climatology* 37 (2017), pp. 124–137.

[181] J. Marshall Shepherd. "A Review of Current Investigations of Urban-Induced Rainfall and Recommendations for the Future". In: *Earth Interactions* 9.12 (2005), pp. 1–27. DOI: 10.1175/EI156.1. URL: https://journals.ametsoc.org/view/journals/eint/9/12/ei156.1.xml.

[182] Xiaoying Yang et al. "Nine-year systematic evaluation of the GPM and TRMM precipitation products in the shuaishui river basin in east-central china". In: *Remote Sensing* 12.6 (2020), p. 1042.

[183] Miguel Laverde-Barajas et al. "St-corabico: A spatiotemporal object-based bias correction method for storm prediction detected by satellite". In: *Remote Sensing* 12.21 (2020), p. 3538.

[184] Elham Ghasemifar et al. "Precipitation rate climatology related to different cloud types using satellite imagery over Iran". In: *Arabian Journal of Geosciences* 11.4 (2018), pp. 1–15.

List of Figures

List of Tables

Cover page: Landscape of the Kafar Meydan mountain, Qazvin, Iran.

Photo by Arash Ghariblou